NOVEL METHODS FOR THE PREVENTION OF NEURODEGENERATION AROUND NEURAL IMPLANTS

by

Noah Robert Snyder

B.S., Allegheny College, 2010

Submitted to the Graduate Faculty of

Swanson School of Engineering in partial fulfillment

of the requirements for the degree of

PhD in Bioengineering

University of Pittsburgh

2015

UNIVERSITY OF PITTSBURGH

SWANSON SCHOOL OF ENGINEERING

This dissertation was presented

by

Noah Snyder

It was defended on

November 16, 2015

and approved by

Carl Lagenaur, Ph.D., Associate Professor, Department of Neurobiology

Alberto Vazquez, Ph.D., Research Assistant Professor, Department of Radiology

Adrian Michael, Ph.D., Professor, Department of Chemistry

Andrew Schwartz, Ph.D., Professor, Department of Neurobiology

Dissertation Director: Xinyan Tracy Cui, Ph.D., Professor, Department of Bioengineering

NOVEL METHODS FOR THE PREVENTION OF NEURODEGENERATION AROUND NEURAL IMPLANTS

Noah Robert Snyder, PhD

University of Pittsburgh, 2015

The recent development of neural prosthetic technology has demonstrated a therapeutic potential for restoring lost sensory or motor functions via a brain-machine interface. Often the devices require direct contact between neural tissue and implanted electrodes to function properly by electrically stimulating or recording neurons on the scale of micro-volts. It is thus critical that the interface between the tissue and the electrode is seamless as well as stable for durations relevant to clinical applications. Unfortunately, the formation of an abiotic/biotic interface is often riddled with host tissue responses that interfere with device function. Neuronal loss due to insertion injury and chronic inflammation and exclusion of recordable cells by an encapsulated glial sheath have all been implicated as potential sources for chronic neural recording failure. Failure to establish a stable interface severely limits the function of implanted neural devices.

In this work we rely upon interdisciplinary techniques in chemistry, biology, and physics to develop methods for the formation of a healthy brain-machine interface as well as new tools for the diagnostics of the tissue response. Through the creation of new biomaterials we have improved the neural interface, reduced local neurodegeneration around chronic implants, and demonstrated *in vivo* improvement of neural recording. In addition, novel conductive and

magnetic nanomaterials have been developed for electrochemically detecting reactive oxygen species associated with implant induced tissue damage as well as treatment strategies using on demand drug release.

By establishing a method for the formation of healthy and stable interfaces between neural tissue and electrode recording devices, the development of neural prosthetic devices can continue to progress towards clinical acceptance.

TABLE OF CONTENTS

LIST OF FIGURES

1.0 INTRODUCTION

Interfacing with neural tissue is an incredibly complicated endeavor that holds the reward of restoring both lost motor and sensory function through neural prosthetic devices.[1, 2] Given the unique electrical and chemical properties of the tissue, it is inherently an interdisciplinary field, interesting researchers in a wide array of backgrounds from electrical engineering and biomaterials, to computer science and mathematics. As scientists develop new technologies with neural interfacing applications, it is vital for a general understanding of a combination of both physical and natural sciences. Often this results in new materials being developed from a large team of researchers unconfined by a single discipline. In that spirit, the scope of this thesis is to outline the design of new technologies for the improvement of the tissue-electrode interface using a combination of molecular biology, synthetic chemistry, and physics. In large part, this work was of engineering motivation. While much of the described work will be valuable for our understanding of the mechanisms and underlying science of the tissue response to implanted devices, the true aim was to generate new technologies with translatable applications. For that reason, clinical relevance and potential acceptance is a focus of each chapter. The following chapters describe the design, preparation, and testing of new materials created with the goal of improving the lives of those impacted by the devastating effects of damage to one of the most important and delicate of tissues, the brain.

1.1 TISSUE-ELECTRODE INTERFACE

In the U.S. alone there are approximately 50 million people affected by one of the nearly 600 neurological disorders. Neurodegenerative diseases, which are classified by the progressive neuronal death within the nervous system, are not only emotionally exhausting to those affected and their families, but it is estimated that in the U.S. $100 billion are spent on health care costs for Alzheimer's disease (AD) alone. Given that the risk for being diagnosed with AD doubles every 5 years after age 65, the economic burden this disease and others like it including Parkinson's disease (PD), Huntington's disease (HD), Amyotrophic Lateral Sclerosis (ALS), etc. continues to weigh heavily on the nation's aging populations.[3, 4]

In recent decades a rapid increase in neurotechnology has enabled researchers across the globe to interact with the nervous system like never before. By implanting electrode probes into neural tissue, extracellular potential changes on the order of micro-volts can be recorded from individual neurons. Conversely, via the application of current into the system, neurons can be stimulated or inhibited resulting in network changes and even influencing behavior. This technology has been the foundation for the emergence of neural prosthetic devices which may someday restore lost motor or sensory function to the millions affected by spinal cord injuries, brain injuries, or neurodegenerative diseases.[1, 2, 5, 6] Of course, the formation of an abiotic/biotic interface is often riddled with interfering biological responses and this technological problem is intensified when interfacing with neural tissue. Failure to establish a stable interface severely limits the function of implanted devices, especially those intended for clinical applications which in most cases would require proper function for the duration of the patient's lifetime. Furthermore, the ability to record from individual neurons continues to increase our knowledge regarding the function of the brain.[7] By establishing a method for the formation of stable

interfaces between neural tissue and electrode recording devices, the development of neural prosthetic devices can continue to progress in addition to the advancement of our ability to study the nervous system.

1.1.1 Neurodegeneration

Current attempts to record the chronic activity of individual neurons from implanted neural electrodes is variable between experiments and often limited in terms of consistently recording from the same neuron over time.[8-10] Cell death resulting from implant insertion as well as chronic inflammation, and exclusion of recordable cells by an encapsulated glial sheath have all been implicated as potential sources for device failure. Given the limited range in which cells must be within to provide isolatable recording data, reversing the reduction of neuron numbers near the implant remains one of the key focuses of improving the interface.[2, 11] Beyond the lack of recordable units, the degradation of the interface mediated by the glial response further hinders the possibility of recording from individual cells resulting in a significant increase of the electrical impedance of the recording sites.[12] Improving the interface by preserving neurons near the implant and controlling the glial reaction will be critical in yielding functional chronic recording implants.

Understanding the direct mechanism behind neuronal loss near chronically implanted electrodes is essential for the development of treatment paradigms that can improve the abiotic/biotic interface. Recent research has demonstrated that degenerating neuronal processes are observed near implant locations, a pathology similar to the neurodegeneration seen in hallmark neurodegenerative disorders such as Alzheimer's disease.[13]

1.2 REACTIVE OXYGEN SPECIES

The biochemical origin of the aforementioned neurological disorders is greatly varied. However, many of these diseases are unified by the progressive excitotoxicity and apoptosis of neurons that ensues. Given the role oxidative species play in these processes it stands that while the presence of reactive oxygen species (ROS) may not be the initiator of each of these diseases, ROS certainly mediate the pathology.[4] In Alzheimer's disease oxidative stress is elevated by the radical generation from an increase in trace metals such as Fe as well as free radicals produced directly from β-amyloid peptide (βAP) aggregated in the senile plaques.[4, 14-16] Likewise, for several decades it has been well established that oxidative stress mediated lipid peroxidation plays a major role in nigral cell death associated with Parkinson's disease.[17, 18] Whether it is the ROS produced by macrophages which results in the demyelination observed in multiple sclerosis (MS), or the increased generation of free radicals from mitochondria following ischemia, it is clear oxidative species play a clear role in the mediation of numerous neurological disorders.[19-21] With recent demonstration of neurodegeneration near neural implants, it appears ROS may also influence the failure of chronically implanted neural electrodes.[13]

1.2.1 Chemistry

Oxidative stress is well known to be at the center of many diseases and disorders. In most references, oxidative stress is defined loosely as the outcome of high levels of reactive oxygen species that results in cellular damage. ROS are highly reactive oxygen containing chemical species that often contain an additional un-paired electron.[22] While many ROS are in fact free radical species, this is not always so, as is the case with highly reactive single oxygen.[23]

Furthermore, a second related family of reactive species, reactive nitrogen species (RNS) are formed as a product of ROS *in vivo*.[24, 25] The combination of ROS/RNS play a dynamic and intertwined role in cellular damage, cell signaling, and the inflammatory response. Collectively we will define reactions, whether chemical or biological, relating to these two families of species as reactive oxygen and nitrogen species (RONS). While RONS are often generalized as a single chemical output, an understanding of the individual biologically relevant species is vital to comprehension of the nuanced impact of oxidative stress. The entire list of RONS is lengthy; however, we place our focus on the most biologically relevant RONS produced in response to cellular damage. Superoxide ($O_2^{\cdot-}$), nitric oxide (NO), peroxynitrite (ONOO-), hydrogen peroxide (H_2O_2), and the hydroxyl radical ($OH\cdot$) are well understood to play pivotal roles in a variety of diseases including neurological disorders.[26-28]

Understanding the relationship between ROS and RNS is an important step in designing new technologies targeting oxidative stress. Superoxide and nitric oxide are produced as both byproducts of reactions within a cell, for the purpose of cell signaling, and as inflammatory agents.[29] Superoxide is produced as a byproduct of cellular respiration in the mitochondria; and typical levels are quenched by a class of proteins known as superoxide dismutase (SOD).[30-33] However, when cell damage occurs, the balance of superoxide production and elimination is tipped. What results is direct cellular damage by superoxide, but of more consequence is the diffusion-limited reaction with nitric oxide to produces the highly reactive nitrogen species, peroxynitrite (Figure 1-1). Within a cell the consequences of high levels of peoxynitrite are extremely toxic, resulting in the oxidation of protein and DNA as well as the peroxidation of the cell membrane.[25, 34]

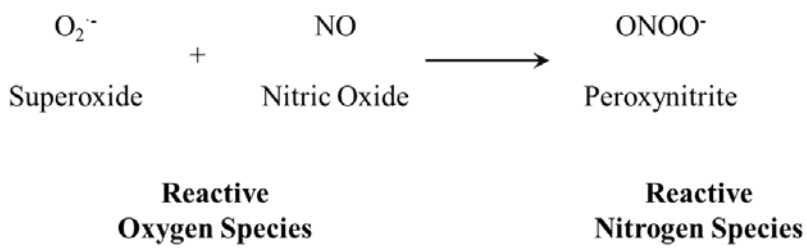

Figure 1-1 Reactive Oxygen and Nitrogen Species Reaction

1.2.2 Biological Sources

Within the CNS, microglia act as the resident macrophage and upon activation transition from a ramified state to an amoeboid-like state. Once activated, microglia secrete pro-inflammatory cytokines, initiate the recruitment of additional macrophages/microglia, and produce various cytotoxic factors such as excitatory amino acids and reactive oxygen species (ROS).[4] Given the proximity of microglia to implanted electrodes, nearby produced reactive oxygen species may directly result in an environment promoting neurodegeneration, especially considering that microglia up-regulate ROS when presented with insoluble promoters of activation.[31, 32] Through the enzymatic production of superoxide and nitric oxide by NADPH oxidase and NO synthase, respectively, the oxidative stress produced by activated microglia results in neuron death. Furthermore, nearby dying cells effectively activate and recruit more microglia producing a positive feedback loop of neuronal death.[33, 35, 36] Employing methods that would reduce reactive oxygen species may not only preserve the number of neurons nearby the electrode, but may also act to decrease the overall microglia response to the implant.

The blood-brain barrier (BBB) is necessary to maintain homeostasis within the CNS and vital for neuronal health. Many diseases are implicated in blood-brain barrier dysfunction and it

is clear that disruption of the BBB has a negative effect on the function of chronic neural implants through recruitment of pro-inflammatory myeloid cells, increased presence of neurotoxic factors, as well as the activation of pathways that increase the levels of ROS.[37, 38] To complicate matters further, reactive oxygen species have been shown to compromise endothelial tight junction proteins and subsequently increase the permeability of the BBB.[39] It is not surprising then that activated microglia alone are sufficient to induce dysfunction of the BBB.[40] In a similar manner to microglial activation, disruption of BBB integrity by chronically implanted electrodes appears to form a positive feedback loop, corroborated by research showing long-term increased BBB permeability[41, 42]. While the circumstances regarding BBB dysfunction are certainly complex, the fact that the process is at least mediated by ROS provides the potential for treating oxidative stress that would improve both BBB integrity and further ameliorate the effects of activated microglia.

Current analysis of oxidative stress and subsequent neurodegeneration around chronic neural electrodes is limited to histological end-point experiments.[30-32] The short half-life and diffusion-limited reactions of reactive oxygen species make immunohistochemistry qualitative at best.[43] The advancement of two-photon microscopy (TPM) allows researchers to now view individual cells within the brain in real-time providing information regarding neuronal activity as well as response to stimuli such as stroke.[38, 44] With the use of dihydrorhodamine 123 (DHR 123), an indicator of the ROS peroxynitrite, the extent of oxidative stress in ex vivo human skin after exposure to UV light shows promise for directly visualizing ROS in tissue.[45] By combining two-photon microscopy with the unique specificity of DHR 123 for peroxynitrite, it may be possible to visualize oxidative stress near a neural electrode in vivo and in real-time.

1.2.3 Antioxidants.

Given the widespread role ROS play in a variety of neurodegenerative diseases and disorders it makes oxidative stress a single therapeutic target for the treatment of a large variety of conditions. Typically, the level of oxidative stress is held in balance by the enzyme family superoxide dismutase (SOD), which can remove the superoxide through dismutation, a process that converts superoxide to molecular oxygen and hydrogen peroxide. However, using SOD to treat diseases that are influenced by oxidative stress, such as neurodegenerative diseases, has been for the most part unsuccessful due to low stability, poor bioavailability, and other negative factors including immunogenicity.[31, 32] In recent years, the development of low molecular weight synthetic molecules that mimic the function of SOD has provided potential pharmaceutical agents for treating oxidative stress.[30-33] One SOD mimic (SODm) in particular, manganese(III) meso-tetrakis-(N-ethylpyridinium-2-yl) porphyrin (Mn^{III}TE-2-Pyp5+), has proven to be neuroprotective in in vitro models of Alzheimer's disease as well as in in vivo models of stroke. Furthermore, Mn^{III}TE-2-Pyp5+ is an equally capable peroxynitrite scavenger, a byproduct of the superoxide and nitric oxide released by microglia making it an ideal compound for reducing a variety of ROS produced in the context of neurological disorders.[30-32]

1.3 L1 NEURAL ADHESION MOLECULE

The development of biomimetic strategies has resulted in new technologies designed to improve the interface between neural tissue and implanted devices.[46, 47] In efforts to reduce the host tissue response as well as promote neuron survival, coatings have been developed using components of

the extracellular matrix. The hope of technologies such as these, is to 'mask' inorganic devices like neural electrodes for the formation of a tight abiotoic/biotic interface. One such technology that has demonstrated great promise both *in vitro* and *in vivo* is the use of the neural cell adhesion molecule, L1CAM.

1.3.1 Biological Origin

Since its discovery in the mid-1980s, the L1 cell adhesion molecule has interested researchers in both the fields of neurodevelopment as well as biomaterials.[48, 49] L1CAM is a transmembrane glycoprotein found along the axons of developing neurons and is responsible for interaction between cells. The protein structure is composed of a larger extracellular region and a highly conserved cytoplasmic domain.[48-52] The extracellular domain contains immunoglobulin and fibronectin-like regions that are responsible for the cell-cell interactions associated with L1CAM. The selective binding of L1CAM to integrins, extracellular matrix proteins, and homophilic interactions are critical for developing cells and important for neuron migration, axon growth, fasciculation, and even synaptic plasticity.

1.3.2 Use for Neural Prosthetic Devices

Given L1CAM's unique ability to promote neuron attachment and cell survival, the protein was an ideal choice for the development of a biomimetic coating. Both recombinant forms of L1 and isolated protein from fresh brain tissue have been studied as a potential route for improving chronic neural electrode technologies.[46, 47, 53] In addition to the improvement of neuron survivability, an additional benefit of L1 coatings is the reduction of inflammation around the

device. In previous work where the coating was applied to silicon-based neural electrodes, the tissue response to L1 coated arrays was mitigated.[46, 47] Both an increase in relative neuron and neurites were observed in L1CAM coated arrays, as well as s reduction in inflammatory cells such as astrocytes and microglia.

1.4 CONDUCTIVE AND MAGNETIC NANOCOMPOSITES

The advancement of nanomaterials is essential for not only industrial coatings and applications but also the development of new highly functional medical devices. The concept of biocompatible films has transitioned from static coatings and materials into advanced materials that can be externally controlled and manipulated. For that reason an emphasis has been placed on materials containing conductive and magnetic properties.[54, 55] These new controllable materials are redefining the manner in which we design new diagnostic and treatment technologies for biological tissue.

1.4.1 Silica and Magnetic Nanoparticles

Silica nanoparticles are widespread through the field of materials science. Given their ease of preparation and unique biocompatible properties, design and optimization of new silica nanoparticles is of great interest to biomaterials researchers.[56-58] Furthermore, these materials can be effectively coupled with magnetic nanoparticle technology to result in a controllable and biocompatible nanocomposite with great potential. One of the key methods for preparing uniform silica nanoparticles is through the sol-gel process. The benefits of the sol-gel process is

that pure silica nanoparticles can be readily prepared and adjusted on the basis of size, distribution, and morphology by altering of reaction parameters and conditions. The general scheme is the preparation of a metal alkoxide solution which reacts to form a silicon polymer network through hydrolysis and condensation. This reaction can be catalyzed under either basic or acidic conditions.

Incorporation of magnetic nanoparticles into silica nanocomposites allows for increased applications for these materials. Magnetic properties allows for improvements in magnetic imaging; however, magnetic separation and drivable hyperthermia properties are of increasing interest to researchers.[19, 38, 43] Applications of static magnetic fields to magnetic nanoaprticles have been effective method for driving nanoparticle localization in tissue, as well as mass transport of nanoparitlce-bound cells. Both of which have great potential for drug delivery and regeneration applictions.[38] In addition, the ability to cause local changes to the tissue through 'excitation' of nanoparticles is increasing in interest. By applying high-frequency magnetic fields, micro-motion of nanoparticles can effectively increase the temperature of nearby tissue.[43, 59] This response has already provided researchers with a new tool to kill cancerous tissue. Furthermore, when tuned, this response can be contained within the nanoparticle, resulting in swelling of the nanomaterial. When combined with drug loaded nanoparticles, this has enabled researchers a new method for controlled drug release.

1.4.2 Conductive Nanomaterials

One of the benefits of conducting polymers in the field of bioelectronics is their use in the preparation of electrode films.[60-63] The conductive nature of these materials is a result of the conjugated backbone that allows for electron transport through the delocalized π-bonds. In

addition oxidation of monomers in solution is easily performed that allows for polymerization at the surface of the electrode. Depending upon the monomer of choice, the resulting insoluble polymer contains either positive or negative charges. When electrodeposition is achieved in the presence of molecules or drugs of the opposite charge, these molecules can be effectively doped within the film. Furthermore, once on the surface of an electrode, these materials retain their conductivity and redox properties. Via the application of a reducing voltage potential, the reduction of the polymer backbone can be driven, releasing the doped drugs in the process. This property has resulted in the development of new controllable drug-release platforms.[61]

1.5 DISSERTATION ORGANIZATION

The work described within this dissertation is focused on the use of synthetic chemistry and materials science to create new coatings and materials for the improvement of the tissue-electrode interface. In general the prepared materials are either directly targeting the mitigation of reactive oxygen species caused by the foreign body response, or are designed for the potential therapeutic delivery for antioxidant compounds. While the tissue response to inorganic implanted devices is certainly complex and composed of an incalculable number of biological signaling pathways, and inevitable consequence is the production of reactive oxygen and nitrogen species. Therefore, the goal of this dissertation is for the development of new techniques to reduce oxidative damage and thereby improve the tissue-electrode interface.

In *Chapter 2*, the preparation of an antioxidant coating for neural probes is described. Using synthetic chemistry a novel superoxide dismutase mimic (SODm) is created and incorporated into a self-assembled monolayer (SAM) coating on neural electrodes. The material

demonstrated effective elimination of the superoxide, one of the main oxidative species produced by inflammatory glial cells. In addition to *in vitro* performance, the coating effectively improved the neuron density near implanted neural electrodes. The applications of this technology are far-reaching and not limited to the improvement of neural technologies. The work described in *Chapter 2* resulted in the development of patent pending technology. This technology is currently being licensed and commercialized by a material science company spun out of the University of Pittsburgh.

Chapter 3 described the creation of a nanocomposite film designed for the purpose of improving electrochemical detection of superoxide. Through direct adsorption of the metallorporphyin complex, hemin, onto a conducting polymer nanocomposite comprised of poly(3,4-ethylenedioxythiophene) (PEDOT) and graphene oxide (GO), we have prepared a sensor capable of reliably detecting superoxide. Using the prepared hemin-PEDOT/GO sensor, we conducted a mechanistic study of the generation of superoxide by the enzyme complex, xanthine oxidase. In addition to providing a platform for our understanding of the mechanism behind the foreign body response, this sensor technology could be used to provide real-time assessment of neural implant health enabling clinicians to implement the appropriate treatment.

Described in *Chapter 4* is the efforts made towards dissemination and translation of a protein based biomimetic coating for neural implants. Built upon our laboratories L1CAM protein coating for neural implants, we have prepared a new methodology for coating FDA-approved neural electrode arrays. In addition, described is the first isolation of the non-human primate L1CAM homologue. As a step towards pre-clinical development, the coating is applied to electronically functional arrays for non-human primate studies, where a general improvement

in neural recording quality is observed. The L1CAM coating optimized in this chapter has resulted in patent pending technology.

The development of novel drug delivery systems using silica magnetic nanoparticles is described in *Chapter 5*. By combining the properties of silica nanomaterials and magnetic nanoparticles, a controlled-release system has been developed. Due to the magnetic nature of the created nanocarriers, controlled drug release can be stimulated using noninvasive application of high-frequency magnetic field. This technology is further developed to provide 'proof-of-concept' evidence for drug delivery using clinical-grade MRI scanner equipment. Furthermore, for the precise application of incorporating a new drug-delivery system directly onto neural electrodes, a self-assembled monolayer magnetic nanoparticle coating is prepared. The nanoparticle coating improves neuron attachment and growth due to the magnetic nanoparticles of the coating and enables future development of magnetically controlled drug-release strategies for neural electrodes.

Finally, *Chapter 6* details the development of a conductive-magnetic nanocomposite designed for electrochemical drug release. We successfully prepared nanoparticles by encapsulating magnetic nanoparticles in a conductive polymer 'shell'. Using this technique we incorporated the model drug, fluorescein and relying upon the magnetic separation of the prepared nanoparticles, electrodeposited the conductive-magnetic nanocomposite onto electrodes. These films were characterized by a rough, fibrous network, and greatly increased the drug release performance when compared to traditional doped polymer coatings. This technology could be used to improve neural electrodes by providing an effective drug-release platform for implanted devices.

In summary, the work described here represents a variety of techniques and methods for the improvement of the neural tissue-electrode interface. The reduction of oxidative species represents a promising strategy for increasing neuron survivability near implants. Using both chemical and biological derived coatings has resulted in promising results that could translate to clinical applications. Finally with the preparation of nanomaterial based films and coatings, we have continued to improve the fields of both bioelectronics and drug-delivery. Each of these technologies could be impactful in the diagnostics and treatment of the inflammatory response around chronically implanted neural devices.

2.0 A SUPEROXIDE-SCAVENGING COATING FOR IMPROVING NEURAL IMPLANTS

2.1 INTRODUCTION

In recent decades neurotechnology has offered researchers new ways to interface with the nervous system. By implanting electrode probes into neural tissue, extracellular potential changes on the order of micro-volts can be recorded from individual neurons. Conversely, via the application of current into the system, neurons can be stimulated or inhibited resulting in network changes and even influencing behavior. This technology has been the foundation for the emergence of neural prosthetic devices which may someday restore lost motor or sensory function to the millions affected by spinal cord injuries, brain injuries, or neurodegenerative diseases.[1, 2, 5, 6] However, implant performance is often riddled with interfering host tissue responses and this technological problem is intensified when interfacing with neural tissue. Failure to establish a stable interface severely limits the function of implanted devices, especially those intended for clinical applications which in most cases would require proper function for the duration of the patient's lifetime. Furthermore, the ability to record from individual neurons continues to increase our knowledge regarding the function of the brain.[7] By establishing a method for the formation of stable and seamless interfaces between neural tissue and electrode devices, the development of neural prosthetic devices can continue to progress in addition to the advancement of our ability to study the nervous system.

Current attempts to record the chronic activity of individual neurons from implanted neural electrodes is variable between experiments and often limited in terms of consistently recording from the same neuron over time.[8-10] Cell death resulting from implant insertion as well as chronic inflammation, and exclusion of recordable cells by an encapsulated glial sheath have all been implicated as potential sources for device failure. Given the limited range in which cells must be within to provide isolatable recording data, reversing the reduction of neuron numbers near the implant remains one of the key focuses of improving the interface.[2, 11] Beyond the lack of recordable units, the degradation of the interface mediated by the inflammatory glial response further hinders the possibility of recording by isolating the electrodes with a scar.[12] Inhibiting neuronal dealth near the implant and controlling the inflammatory reaction will be critical in yielding long term high quality neural recording or stimulation[cite the caspase-1 paper].

Recent research has demonstrated that degenerating neuronal processes are observed near implant locations, a pathology similar to the neurodegeneration seen in hallmark neurodegenerative disorders such as Alzheimer's disease.[13] The biochemical origin of the aforementioned neurological disorders is greatly varied. However, many of these diseases are unified by the progressive excitotoxicity and apoptosis of neurons that ensues. Given the role oxidative species play in these processes it stands that while the presence of reactive oxygen species (ROS) may not be the initiator of each of these diseases, ROS certainly mediate the pathology.[4] For several decades it has been well established that oxidative stress mediated lipid peroxidation plays a major role in nigral cell death associated with Parkinson's disease.[17, 18] Whether it is the ROS produced by macrophages which results in the demyelination observed in multiple sclerosis (MS), or the increased generation of free radicals from mitochondria following

ischemia, it is clear oxidative species play a clear role in the mediation of numerous neurological disorders.[19-21]

ROS are highly reactive oxygen containing chemical species that often present an additional un-paired electron.[22] While many ROS are in fact free radical species, this is not always so, as is the case with highly reactive single oxygen.[23] Furthermore, a second related family of reactive species, reactive nitrogen species (RNS) are formed as a product of ROS *in vivo*.[24, 25] The combination of ROS/RNS play a dynamic and intertwined role in cellular damage, cell signaling, and the inflammatory response. Collectively we will define substances, whether chemical or biological, relating to these two families of species as reactive oxygen and nitrogen species (RONS). While RONS are often generalized as a single chemical output, an understanding of the individual biologically relevant species is vital to comprehension of the nuanced impact of oxidative stress. The entire list of RONS is lengthy; however, superoxide ($O_2^{\cdot -}$), nitric oxide (NO), peroxynitrite (ONOO-), hydrogen peroxide (H_2O_2), and the hydroxyl radical ($OH\cdot$) are well understood to play pivotal roles in a variety of diseases including neurological disorders.[26-28]

Understanding the relationship between ROS and RNS is an important step in designing new technologies targeting oxidative stress. Superoxide and nitric oxide are produced as both byproducts of reactions within a cell, for the purpose of cell signaling, and as inflammatory agents.[29] Superoxide is produced as a byproduct of cellular respiration in the mitochondria; and typical levels are quenched by a class of proteins known as superoxide dismutase (SOD).[30-33] However, when cell damage occurs, the balance of superoxide production and elimination is tipped. What results is direct cellular damage by superoxide, but of more consequence is the diffusion-limited reaction with nitric oxide to produces the highly reactive RNS, peroxynitrite.

Within a cell the consequences of high levels of peoxynitrite are extremely toxic, resulting in the oxidation of protein and DNA as well as the peroxidation of the cell membrane.[25, 34]

Within the CNS, microglia act as the resident macrophage and upon activation transition from a ramified state to an amoeboid-like state. Once activated, microglia secrete pro-inflammatory cytokines, initiate the recruitment of additional macrophages/microglia, and produce various cytotoxic factors such as excitatory amino acids and reactive oxygen species (ROS).[64, 65] Activated microglia/macrophages have been identified to be the primary cell type immediately contacting implanted electrodes.[11] Given the proximity of these cells to the neural implants and their activation state, nearby produced reactive oxygen species may directly result in an environment promoting neurodegeneration, especially considering that microglia up-regulate ROS production when presented with insoluble promoters of activation.[66] Through the enzymatic production of superoxide and nitric oxide by NADPH oxidase and inducible NO synthase (iNOS), respectively, the oxidative stress produced by activated microglia results in neuron death. Furthermore, nearby dying cells effectively activate and recruit more microglia producing a positive feedback loop of neuronal death.[64, 67, 68] Employing methods that would reduce reactive oxygen species may not only preserve the number of neurons nearby the electrode, but may also act to decrease the overall microglia pro-inflammatory response to the implant.

The blood-brain barrier (BBB) is necessary to maintain homeostasis within the CNS and vital for neuronal health. Many diseases are implicated in blood-brain barrier dysfunction and it is clear that disruption of the BBB has a negative effect on the function of chronic neural implants through recruitment of pro-inflammatory myeloid cells, increased presence of neurotoxic factors, as well as the activation of pathways that increase the levels of ROS.[37, 38] To

complicate matters further, reactive oxygen species have been shown to compromise endothelial tight junction proteins and subsequently increase the permeability of the BBB.[39] It is not surprising then that activated microglia alone are sufficient to induce dysfunction of the BBB.[40] In a similar manner to microglial activation, disruption of BBB integrity by chronically implanted electrodes appears to form a positive feedback loop, corroborated by research showing long-term increased BBB permeability[41, 42]. While the circumstances regarding BBB dysfunction are certainly complex, the fact that the process is at least mediated by ROS provides the potential for treating oxidative stress that would improve both BBB integrity and further ameliorate the effects of activated microglia.

Typically, the level of oxidative stress is held in balance by the enzyme family SOD, which can remove the superoxide through dismutation, a process that converts superoxide to molecular oxygen and hydrogen peroxide. However, using SOD directly to treat diseases that are influenced by oxidative stress, such as neurodegenerative diseases, has been for the most part unsuccessful due to low stability, poor bioavailability, and other negative factors including immunogenicity.[31, 32] In recent years, the development of low molecular weight synthetic molecules that mimic the function of SOD has provided potential pharmaceutical agents for treating oxidative stress.[30-33] One of the earliest superoxide dismutase mimic (SODm) complexes that has been tested in disorders relevant to oxidative stress and been incorporated into coatings for neural implants is manganese (III) tetrakis (4-benzoic acid) porphyrin chloride (MnTBAP).[69] However, the negative charge of the complex combined with the fact that the redox potential was outside the window for catalytic dismutation of superoxide, resulted in the development of new complexes.[70]

One SOD mimic (SODm) in particular, manganese(III) meso-tetrakis-(N-ethylpyridinium-2-yl) porphyrin (Mn^{III}TE-2-Pyp5+), has proven to be neuroprotective in *in vitro* models of Alzheimer's disease as well as in *in vivo* models of stroke. Furthermore, Mn^{III}TE-2-Pyp5+ is an equally capable peroxynitrite scavenger, a byproduct of the superoxide and nitric oxide released by microglia making it an ideal compound for reducing a variety of ROS produced in the context of neurological disorders.[30-32]

Previous work to functionalize silicon-based neural electrodes by covalent attachment of biomolecules has shown great promise at improving the tissue-electrode interface.[46, 47, 71] To reduce the oxidative stress and improve the neuronal survival near chronically implanted neural electrodes, we have designed a new coating based upon a synthetic derivative of Mn^{III}TE-2-$Pyp5^{+}$. Described here are the synthesis and coating strategy, *in vitro* performance of coated substrates, and *in vivo* histological evidence demonstrating an increase in neuron survivability nearby SODm coated neural electrodes.

2.2 MATERIALS AND METHODS

2.2.1 Chemicals and Reagents

The unsubstituted porphyrin, H_2T-2-Pyp, as well as the metalloporphyrin, Mn^{III}TE-2-Pyp5+ (manganese(III)-5,10,15,20-tetrakis(N-ethylpyridinium-2-yl)porphyrin)), can be purchased from Frontier Scientific, Inc. (Logan, UT). Resveratrol as well as manganese (III) tetrakis (4-benzoic acid) porphyrin chloride (MnTBAP) were purchased from EMD Millipore Corp. The remaining chemical reagents, biological reagents, and solvents were purchased from Sigma Aldrich.

2.2.2 Synthesis of the *Immobilizable Superoxide Dismutase Mimic* (iSODm)

The preparation of the alkylamine functionalized metalloporphyrin, MnIIITEA-2-Pyp5+ (manganese(III)-5,10,15,20-tetrakis(N-(2-aminoethyl)pyridinium-2-yl)porphyrin)) herein referred to as iSODm, occurs via a one-pot synthesis and direct metalation of the unsubstituted porphyrin H_2T-2-Pyp (meso-Tetra (2-pyridyl) porphine). The unsubstituted porphyrin, H_2T-2-Pyp, was dissolved in DMF with excess 2-bromethylamine in a round bottom flask equipped with a refluxing condenser. The temperature was raised to 100 ºC and the reaction was kept under reflux for 24 – 48 hr. The extent of the reaction was measured via the progressive appearance of mono-, di- , tri-, and tetra- substituted porphyrin species monitored via thin-layer chromatography (TLC) using KNO_3-saturated H_2O-H_2O-acetonitrile (1:1:8, v/v/v/) and the characteristic UV-Vis absorption peak at 414 nm. Following completion of the reaction to the tetra- substituted porphyrin, excess $MnCl_2$ was added directly to the flask and the reaction was kept under reflux for an additional 24 – 48 hr. The progression of the reaction was monitored by observation of the Soret band after metallation shift to 450 nm. After the completion of the reaction, the solution was cooled to room temperature and the final metalloporphyrin product was precipitated by the addition of tetrahydrofuran (THF). The complex was filtered and washed with THF and diethylether. Purification was achieved via ion exchange and crystallization. The water-soluble product was dissolved in water and crystallized using a saturated ammonium hexafluorophosphate solution. The final water soluble product was prepared by dissolving the hexafluorophosphate salt complex in acetone and precipitation with tetrabutylammonium chloride.

2.2.3 Electrochemical Characterization of the iSODm Complex

Electrochemical measurements were performed in a glass cell containing a glassy carbon working electrode (3 mm in diameter), a Pt foil counter electrode, and an Ag/AgCl electrode (in 1 M KCl solution) as a reference electrode using the Autolab Potentiostat/Galvanostat (Metrohm). Measurements were taken of 10 mM iSODm in 0.2 mM PBS, pH = 7.5 at a scan rate of 100 mV/s between -0.1 V to 0.5 V NHE.

2.2.4 Immobilization of iSODm

2.2.4.1 Cleaning and Pre-Treatment of Samples

Glass coverslips or dummy A-style silicon based neural probes (NeuroNexus, Ann Arbor MI) were submerged in a 1:1 MeOH:HCl solution for 30 min. in a large crystallization dish with gentle agitation to remove organic residue. After rinsing with deionized water, concentrated H_2SO4 was pipetted directly onto the samples. Following 30 min. of acid surface activation, the samples were rinsed with deionized water and dried under N_2 flow overnight.

2.2.4.2 Silanization

Pre-treated glass samples or silicon probes were submerged in a 2.5% solution of the organosilane, (3-Mercaptopropyl) trimethoxysilane (in toluene) and shaken for 2 hr. inside a glove bag under N_2. Afterwards, the samples were rinsed with copious amounts of toluene and sonicated in a water bath to remove excess unreacted silane. Sonicated samples were rinsed

again with toluene and allowed to dry under N_2 flow. The heterobifunctional crosslinker sulfo-gmbs (N-ɣ-maleimidobutyryl-oxysulfosuccinimide ester) was dissolved in minimal amounts of DMF and diluted to 0.5 mg/mL in absolute ethanol. The silanized surfaces were submerged in the sulfo-gmbs solution for 1 hr, then rinsed with absolute ethanol and dried. Finally, the functionalized iSODm complex was covalently attached to the activated surface by submerging the substrates in 1 mg/mL iSODm solution (PBS) for 1 hr. Successful coating was verified by confirmation of sulfur (silane) and manganese (iSODm) using X-ray photoelectron spectroscopy (XPS) for elemental composition with a MCL – ESCALAB 250 XI Thermo Scientific XPS.

2.2.5 Superoxide Scavenging Activity of iSODm

To determine the catalytic superoxide scavenging nature of the synthesized iSODm complex in comparison to other antioxidants, the cytochrome C assay is used to monitor superoxide produced via the xanthine oxidase enzyme system. Superoxide ($O_2^{\cdot -}$) was generated with xanthine oxidase (10 nM) and pterine (100 µM) in the presence of cytochrome c (50 µM) in PBS. To prevent interference from H_2O_2, 15 µg/mL catalase was added to the reaction. The reduction of cytochrome C by superoxide was monitored at 550 nm in the presence of different antioxidants to determine individual antioxidant activity. Besides iSODm, the antioxidants tested are:

2.2.6 *In vitro* bioactivity testing of iSODm immobilized surfaces

2.2.6.1 HAPI Cell Line

Frozen Highly Aggressive Proliferating Immortalized (HAPI) microglia cells (provided by Dr. Xiaoming Hu, Department of Neurology, University of Pittsburgh) were thawed and passaged once before being plated at a density of 1 x 10^5 cells/cm^2 in 24-well plates. Cells were plated directly onto glass coverslips. Cells to test the iSODm coating were plated directly onto glass coverslips that were coated with iSODm as described above. Cells to test the soluble antioxidants were plated directly onto glass coverslips in media containing either 10 µM Mn^{III}TE-2-Pyp5+(SODm), MnTBAP, resveratrol, or diphenyleneiodonium (DPI). Before activation, cells were grown until ~ 80% confluence (24 hr) in serum containing media (10% fetal bovine serum, DMEM (Gibco 21041 DMEM/F12 +L-glutamine – HEPES – Phenol Red, Invitrogen, Carlsbad CA)). Cells were plated in triplicate per group and incubated at 37 ºC.

2.2.6.2 Inflammatory Activation of HAPI Cells

HAPI cells were incubated with stimulating agents to activate the immune response via either the Damage-Associated Molecular Pattern (DAMP) pathway or the Pathogen-Associated Molecular Pattern (PAMP) pathway. Following initial proliferation of cells, all cells were maintained in serum-free DMEM media and treatment conditions were replenished when changing media.

For the PAMP pathway response, cells were stimulated with gram-negative bacteria-derived lipopolysaccharide (LPS, from Escherichia coli) at a concentration of 10 ng/mL in the

presence of 2 ng/mL interfeuron gamma (IFNɣ). Cells were stimulated for 24 with LPS/IFNɣ stimulation prior to measurement of oxidative species or fixation.

DAMP pathway activation was triggered with incubation in serum-free media containing 5 µg/mL phobol 12-myristate 13-acetate (PMA). Cells were stimulated with PMA for 3 hr. prior to the measurement of oxidative species or fixation.

2.2.6.3 Measurement of NO Output of Activated HAPI Cells

Nitric oxide production of stimulated cells was measured using the commercially available Griess Reagent Kit (Invitrogen, Carlsbad CA). Samples of the cellular supernatant are taken and mixed with the Griess reagent. Following 30 min. incubation at room temperature, NO levels were measured by measuring the absorbance at 540 nm. For each group, NO levels were normalized by cell count and a percent change from unstimulated cells was compared using two-way ANOVA, followed by Tukey's post hoc analysis. A p-value of < 0.05 is considered significant.

2.2.6.4 Measurement of $O_2^{\cdot -}$ Output of Activated HAPI Cells

Superoxide production by cells was monitored using the cytochrome C assay. In brief, 3 hr. prior to the PMA stimulation endpoint, media containing 10 μM cytochrome C was added to each well. For antioxidant groups and inflammatory response treatments, the appropriate concentrations of the antioxidants/stimulating agents were included with the cytochrome C. Following 3 hr., the reduction of cytochrome C is measured at 550 nm. For each group, O2·- levels are normalized by cell count and a percent change from unstimulated cells was compared using two-way ANOVA, followed by Tukey's post hoc analysis. A *p*-value of < 0.05 is considered significant.

2.2.6.5 Intracellular Staining of Reactive Oxygen Species

Intracellular staining of ROS was completed using the probe dihydrorhodamine (DHR) dye. Prior to the endpoint for all conditions, media containing 10 μM DHR was added to each well. For antioxidant groups and inflammatory response treatments, the appropriate concentrations of the antioxidants/stimulating agents were included with the cytochrome C. After 3 hr., cells were fixed with 4% paraformaldehyde and used for subsequent staining described below.

2.2.6.6 In vitro Cell Staining, imaging and quantification

Immunofluorescence was performed on HAPI cells fixed with 4% paraformaldehyde (PFA) for 10 minutes and blocked with 10% goat serum for 45 min. The following monoclonal primary antibodies were incubated at room temperature together at a dilution of 1:500 for 1.5 hr in 2.5% goat serum in PBS: mouse anti-ED1 (AdD Serotec, Raleight NC), rabbit anti-iNOS (inducible nitric oxide synthase, Millipore), and chicken anti-ARG-1 (arginase; Millipore). Cells previously stained with DHR (above) were incubated with rabbit anti-p47-phox (Millipore) for 1.5 hr. After washing, the appropriate fluorescence-conjugated secondary antibodies were added in 2.5% goat serum for 1.5 hours. Cell nuclei were counterstained with Hoechst 33258 (2µg/mL; Sigma-Aldrich) at a dilution of 1:1000 in PBS. For a comparison of *in vitro* cell staining and DHR quantification, corrected total cell fluorescence (CTCF) was calculated. The integrated density of cell bodies was measured using ImageJ and substracted from the average normalized background (area of cell x mean fluorescence of background reading). The CTCF was compared using two-way ANOVA, followed by Tukey's post hoc analysis. A p-value of < 0.05 is considered significant.

2.2.7 Primary Neuron Cultures

The ability of the iSODm coated samples to promote cell growth was examined by primary rat neuronal cell cultures. E18 Sprague-Dawley rat cortices were purchased from BrainBits, LLC. The rat cortices were triturated with a 1 mL pipette and removed from the Hibernate MediaTM via centrifugation at 800g for 1 minute. Cells were re-suspended in Neurobasal (Fisher)/B27

(Gibco)/0.5 mM glutamine/25 µM glutamate (Sigma-Aldrich) culture medium and plated directly onto either glass or iSODm coated glass coverslips in 24-well cell culture plates (Corning Costar) at a density of 2.5 x 105 cells/cm2. Cells were grown in culture for 5 days at 37 °C in 5% CO2 and media was refreshed after day 3. Cells were fixed with 4% paraformaldehyde for 10 min. and stained with the monoclonal antibodies against neuronal class III β-tubulin (Covance) and the astrocyte-specific marker glial fibrillary acidic protein (GFAP) (Dako). Fluorescence images were taken using a fluorescence microscope and samples were evaluated for neuron attachment and neurite extension.

2.2.8 1 Week Implantation of iSODm Coated Neural Probes

2.2.8.1 Surgical Procedures

Six adult male Sprague-Dawley rats (~ 350 g) were used throughout this study. Raw A-style probes were implanted bilaterally with a total of 15 control (uncoated) and 15 iSODm coated arrays (N = 15). A 1 week endpoint was investigated to determine the acute effect of the iSODm coating on neuron survivability. The animals were housed in University of Pittsburgh Department of Laboratory Animal Resources and given free access to food and water. All experiments and housing complied with the United States Department of Agriculture guidelines and were approved by the University of Pittsburgh's Institutional Animal Care and Use Committee. Probes (Control or iSODm coated) were implanted bilaterally into the motor area (1 mm anterior to Bregma, 2.5 mm Lateral), the somatosensory (2 mm posterior to Bregma, 2.5 mm lateral), and the visual area (4.5 mm posterior to Bregma, 2.5 mm lateral) in the cerebral cortex of the animal. General anesthesia was achieved with a mixture of 3% isoflurane in 1 L/min. O2

prior to implantation and was maintained at 1-2% isoflurane for the extent of the surgery. The state of anesthesia was closely monitored by observing the respiratory rate, heart rate, and absence of the pedal reflex. The animals were placed in a stereotaxic frame and their head was shaved, disinfected with isopropyl alcohol/betadine, and a sterile drape was placed over the surgical area. Ophthalmic ointment was applied to the animal, and the surface of the skull was exposed with a single incision along the midline. Three screw holes were drilled using a manual drill at each of the target areas (motor, somatosensory, visual) on both hemispheres. Two iSODm coated probes were implanted on the left hemisphere as well as one control probe (vice-versa for the opposite hemisphere). In total each group had electrodes implanted into each area of the cortex. Prior to insertion of the probes, the dura layer was removed using a 30 gauge needle bent at 90°. The probes were inserted manually using a vacuum inserter device that held the delicate Raw probes. Following implantation, the craniotomies were filled with Kwik-Sil (World Precision Instruments, Sarasota FL) followed by FUSIO liquid dental cement. The skin was sutured around the dental cement head-cap and the animal was allowed to recover.

2.2.8.2 Immunohistochemistry of brain tissue

After the 1 week time point, animals were anesthetized with 50 mg/mL ketamine and 5 mg/mL xylazine administered via the intraperitoneal (IP) cavity with a dosage of 0.1 mL/100 g body weight. The animals were transcardially perfused with 4% (w/v) paraformaldehyde in PBS. The brain was removed, taking care not to damage the implant site when removing the head-cap and post-fixed for 6 hr. The post-fixed brains were then equilibrated in 15% sucrose solution (4°C) overnight, followed by 30% for an additional 24 hr until the tissue sunk to the bottom of

the sucrose vial. The tissue was cut at 25 µm thick sections after cryoprotecting using optimal cutting temperature compound (OCT, Tissue-Tek, Torrance CA).

Tissue sections at ~ 1000 µm deep were hydrated in PBS and blocked with 10% normal goat serum. Following 45 min in 0.5% Triton X-100 in PBS, the sections were incubated with the primary mouse monoclonal NeuN (1:500, Neuronal Nuclei, Millipore). The sections were rinsed and incubated for 1 hr in goat anti-mouse IGG Alexa 594 (Invitrogen, USA). All sections were counterstained using Hoechst nuclear die, cover-slipped and preserved with fluoromount-G.

2.2.8.3 Fluorescent Imaging and Quantitative Brain Tissue Analysis

Confocal fluorescent images were acquired using a FluoView 1000 (Olympus, Inc., Tokyo, Japan) at the Center for Biological Imaging. Images for each antibody were taken in a single session to reduce differences in microscope sessions during data analysis. For in vivo images, all sections were near 1000 µm depth to reduce variability in tissue.

Neuron density was determined by counting neuron cell bodies stained with NeuN in concentric rings every 25 µm around the implant to 250 µm radially outwards. Total number of cells in each bin were counted using ImageJ. Neuron density per area was averaged for each implant group (Control vs. iSODm) and compared using two-way ANOVA, followed by Tukey's post hoc analysis. A p-value of < 0.05 is considered significant.

To compare the inflammatory response cellular markers for astrocytes (GFAP), microglia (OX42), and vascular leaking (IgG) were visualized. Average pixel intensity was calculated at a function of the distance from the probe, normalized to background tissue, and compared using two-way ANOVA, followed by Tukey's post hoc analysis. A p-value of < 0.05 is considered significant.

2.3 RESULTS AND DISCUSSION

2.3.1 Design and Characterization of iSODm

The design of highly potent antioxidants is of great interest due to the role of oxidative species in cancer, neurologic disorders, traumatic brain injury, etc. In the realm of synthetic antioxidants, cationic metalloporphyrins such as $Mn^{III}TE\text{-}2\text{-}Pyp^{5+}$ have demonstrated some of the highest activity for superoxide scavenging.[30] The key characteristic of $Mn^{III}TE\text{-}2\text{-}Pyp^{5+}$ that makes it such an effective antioxidant is that the complex's redox potential ($E_{1/2}$ = 230 mV vs NHE) lies roughly half-way between the oxidation (-160 mV) an reduction (890 mV) potentials of superoxide. To be an effective superoxide dismutase mimic (SODm) and to catalytically dismute superoxide, a metal complex must have a redox potential ~ 200 - 350 mV. The anionic metalloporphyrin MnTBAP was initially believed to be an effective SODm. However, combined with the complex's low $E_{1/2}$ which is nearly – 200 mV vs NHE, and the demonstration that impurities had bestowed earlier studies with SODm activity, research has determined MnTBAP to be an ineffective SODm.[70] On the other hand $Mn^{III}TE\text{-}2\text{-}Pyp^{5+}$ has demonstrated extraordinarily high SODm activity as well as it's antioxidant efficacy in several models of oxidative stress including *in vivo* models of stroke, diabetes, and cancer.

Therefore $Mn^{III}TE\text{-}2\text{-}Pyp^{5+}$ is considered an excellent candidate for incorporation into an antioxidant coating.[31],[32] To that end, we designed a metalloporphyrin that would retain the properties of $Mn^{III}TE\text{-}2\text{-}Pyp^{5+}$ which makes it an efficient SODm while adding amine functional groups that would provide coupling points for surface immobilization on to neural probe surfaces (Figure 2-1).[47], [46]

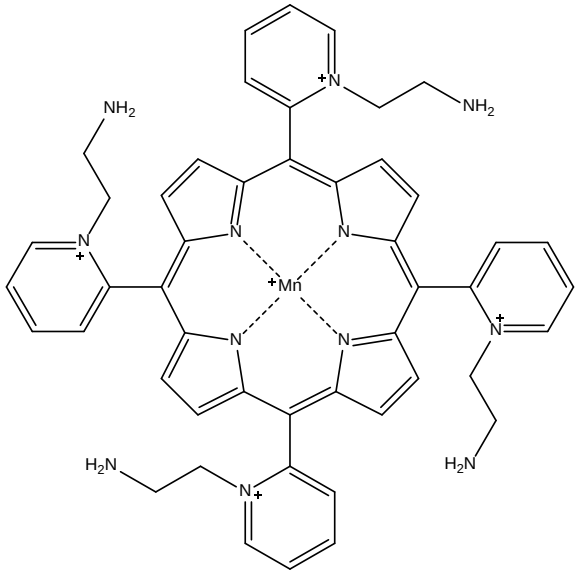

Figure 2-1 Chemical Structure for Novel Immobilizable SODm (iSODm).

First, it was necessary to demonstrate the newly synthesized immobilizable SODm (iSODm) maintains the properties that would make it an effective SODm. To test this, cyclic voltammetry (CV) was used to determine the redox potential of iSODm (Figure 2-2).

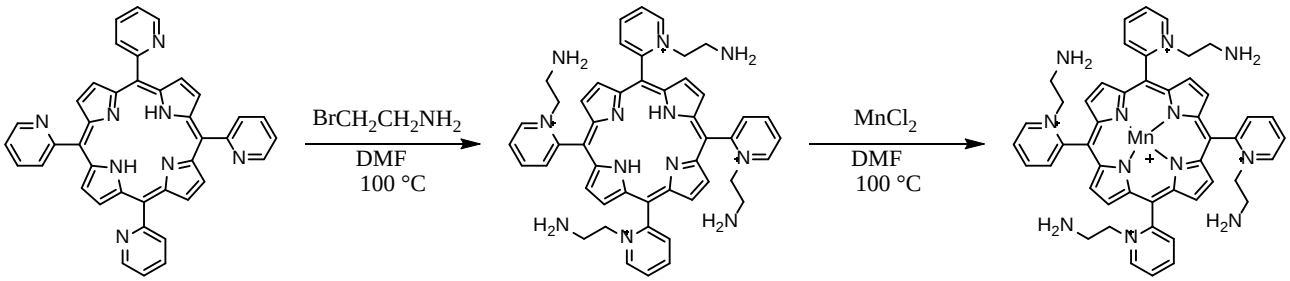

Figure 2-2 Synthesis Scheme for iSODm

First, it was necessary to demonstrate the newly synthesized immobilizable SODm (iSODm) maintains the properties that would make it an effective SODm. To test this, cyclic voltammetry (CV) was used to determine the redox potential of iSODm (Figure 2-3). The redox potential for iSODm was shown to be relatively unchanged from SODm at ~ 240 mV vs NHE, well within the catalytic window for superoxide dismutation.

Then, to test whether the iSODm also demonstrated superoxide scavenger activity as SODm, the capacity of the complex to remove superoxide in the xanthine oxidase system was evaluated. Traditionally the xanthine-xanthine oxidase system has been the most widely used source of superoxide produced as a bi-product during the oxidation of xanthine to uric acid. However, uric acid in itself has radical scavenging capabilities and therefore we used the more effective pterine-xanthine oxidase system.[25]

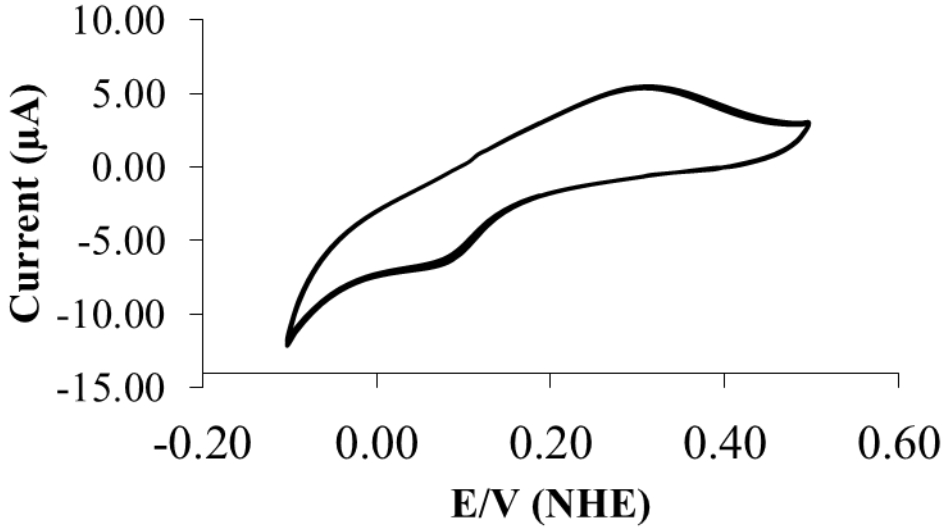

Figure 2-3 CV Curve of iSODm at 100 mV/s in 1X PBS vs. NHE.

The CV curve obtained of iSODm at 100 mV/s in 1X PBS vs. NHE. The $E_{1/2}$ of the synthesized iSODm is 220 mV vs. NHE, within the window necessary for catalytic dismutation of superoxide.

The superoxide-mediated reduction of cytochrome C in the presence of several antioxidants including iSODm, $Mn^{III}TE\text{-}2\text{-}Pyp^{5+}$, MnTBAP, and resveratrol was measured (Figure 2-4). Without any antioxidant treatment, cytochrome C reduction occurs at a constant rate indefinitely (PBS control), suggesting a constant supply of superoxide from the pterine-xanthine oxidase system. Likewise, the addition of resveratrol does not decrease the rate of cytochrome C production.

The antioxidant properties of resveratrol have been widely studied for many years. However, unlike catalytic SODm complexes, the antioxidant properties of resveratrol are believed to occur via suppression of NF-κB pathway following oxidative insult.[72] Therefore its negative impact on superoxide production in this non biological assay is expected. Also as expected by MnTBAP's low $E_{1/2}$, the anionic porphyrin is ineffective at preventing superoxide-

mediated reduction of cytochrome C. Conversely, both $Mn^{III}TE\text{-}2\text{-}Pyp^{5+}$ and iSODm completely prevented cytochrome C reduction for the duration of the experiment, further verifying that iSODm remains a potent superoxide scavenger.

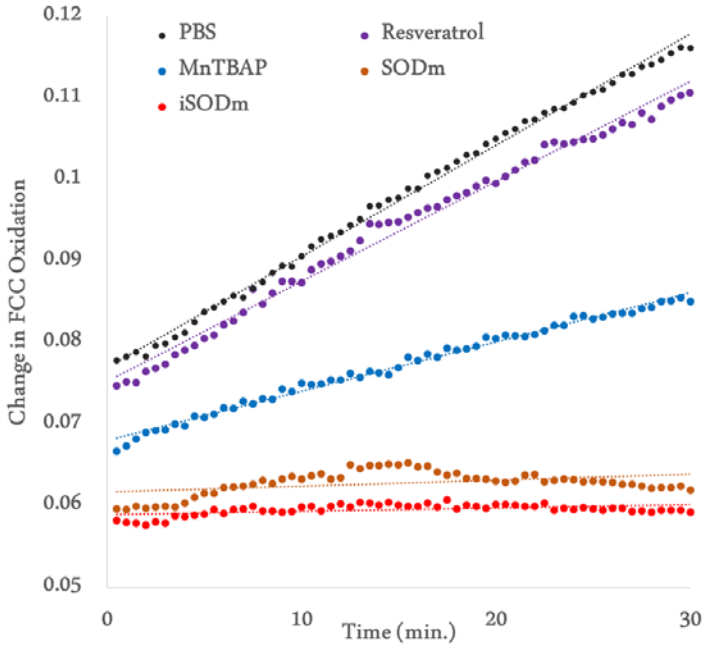

Figure 2-4 Antioxidant Activity of iSODm Compared to Other Known Antioxidants.

Antioxidant activity of iSODm compared to other known antioxidants. A constant supply of superoxide was generated using a Xanthine Oxidase/Pterine enzymatic system. Superoxide concentration was measured via the stoichiometric reduction of ferricytochrome C (FCC) by superoxide. Only the cationic antioxidant, SODm and the iSODm coating completely abolished FCC oxidation indefinitely.

2.3.2 *In Vitro* Antioxidant Effects of iSODm

To evaluate the antioxidant performance of the iSODm coating, an *in vitro* model was used based upon an immortalized microglia cell line. Highly Aggressively Proliferating Immortalized cell line, or HAPI cells, are an immortal cell line of macrophage/microglia lineage that demonstrate an inflammatory response when stimulated with cytokines, lipopolysaccharide (LPS), etc.[73] Given the nature of these cells, they are ideal for testing antioxidant performance under biologically relevant conditions of oxidative stress. Cells were either plated on glass (with or without antioxidant treatment in media) or glass coverslips coated with the iSODm. Following stimulation of the cells to activate the inflammatory response the oxidative output of the cells was evaluated in all conditions as well as the levels of several proteins important in oxidative species production.

One of the key mechanisms of the DAMP pathway is the activation of protein kinase C and subsequent phosphorylation/activation of the NADPH oxidase. The enzyme complex NADPH Oxidase functions to produce superoxide in monocyte derived cells including brain microglia as part of the inflammatory response. Phorbol myristate acetate (PMA) has been shown to activate protein kinase C and result in superoxide production of microglia cells via NADPH oxidase.[42], [53] PMA stimulation was used as a model for superoxide production and the inflammatory response of microglia cells according to the DAMP pathway. In addition to the iSODm coating and the other antioxidants, Diphenyleneiodonium was included as a control. Diphenyleneiodonium (DPI) has been shown to decrease superoxide-mediated cytochrome c reduction following NADPH oxidase activation of primary mouse monocytes/macrophages upon activation by 12-*O*-Tetradecanoyl-13-acetate (TPA).[74] DPI functions by inhibiting the NADPH oxidase enzyme complex. Following stimulation of HAPI cells with PMA, we observed over a

350% increase in cytochrome C reduction in control cells (Figure 2-5). Only cells plated on the iSODm coating or with $Mn^{III}TE\text{-}2\text{-}Pyp^{5+}$ in solution were at or below pre-stimulation levels. In fact, both treatments were significantly lower than DPI, the inhibitor of NADPH oxidase. As expected by the negligible antioxidant performance with the pterine-xanthine oxidase system, MnTBAP did not prevent superoxide-mediated cytochrome C reduction, nor did resveratrol.

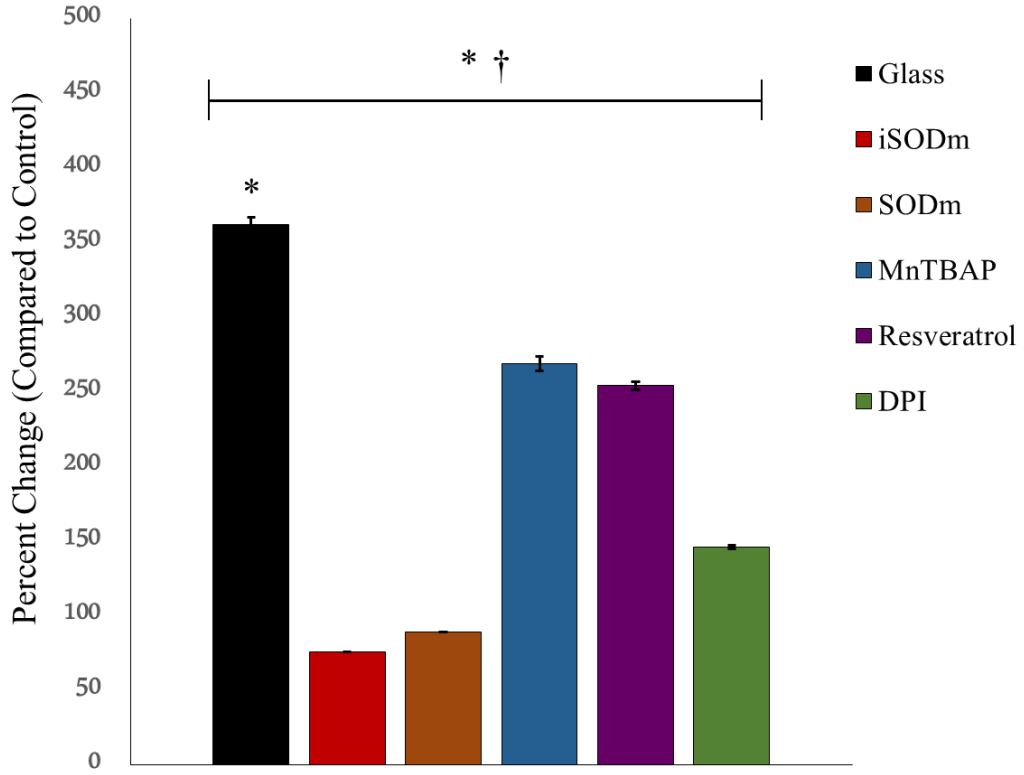

Figure 2-5 FCC Assay of PMA Stimulated HAPI Cells.

FCC Oxidation is Prevented by iSODm coating following stimulation of PMA. FCC oxidation following PMA stimulation is completely abolished by both the iSODm coating and the SODm in solution (± SEM; n = 3; * $p < 0.05$ compared to glass control; † $p < 0.05$ compared to group control).

Upon activation of protein kinase C, phosphorylation of the subunit p47 is translocated from the cytosol of the cell to the plasma membrane where it joins the other subunits of the NADPH oxidase complex.[53] Following stimulation of HAPI cells with PMA, a significant increase in p47 staining is observed (Figure 2-6). This increase is significantly decreased when cells are plated onto the iSODm coating. Superoxide is known to increase protein kinase C activity and thus form a positive feedback loop for activity. Therefore, by decreasing superoxide levels, the overall inflammatory response of the cells can be lowered.

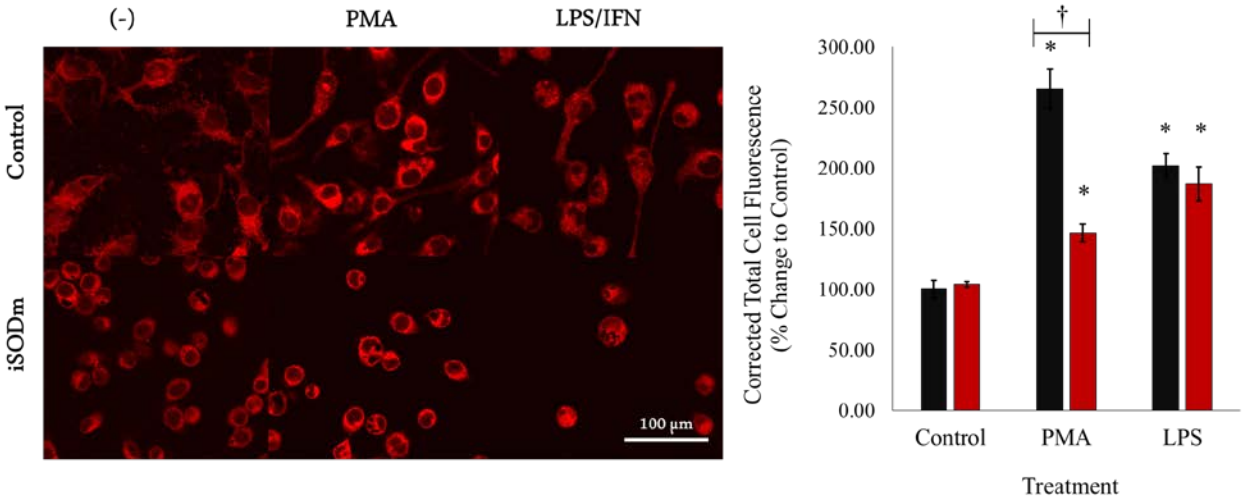

Figure 2-6 Cellular levels of the NADPH Oxidase protein, p47phox in stimulated microglia cells.

By using the corrected total cell fluorescence, a significant increase in p47 staining is observed in control microglia cells following treatment with either PMA or LPS. The CTCF from p47 staining is significantly lower in cells plated on the iSODm coating following PMA stimulation (± SEM; n = 20; * $p < 0.05$ compared to glass control; † $p < 0.05$ compared to glass treatment).

Lipopolysaccharide (LPS) is well established as an effective stimulating agent to induce the inflammatory response of microglia via the Pathogen-Associated Molecular Pattern (PAMP) pathway. Following activation by LPS/IFNγ, the activity of inducible nitric oxide synthase is

increased resulting in production of nitric oxide. To measure NO production in cells stimulated with LPS/ IFNγ, the commercially available Griess Reagent Assay was used. Interestingly, both the cationic porphyrin (iSODm) treatments and the anionic porphyrin ($Mn^{III}TE\text{-}2\text{-}Pyp^{5+}$) resulted in significantly increased NO output as measured by the Griess Assay (Figure 2-7).

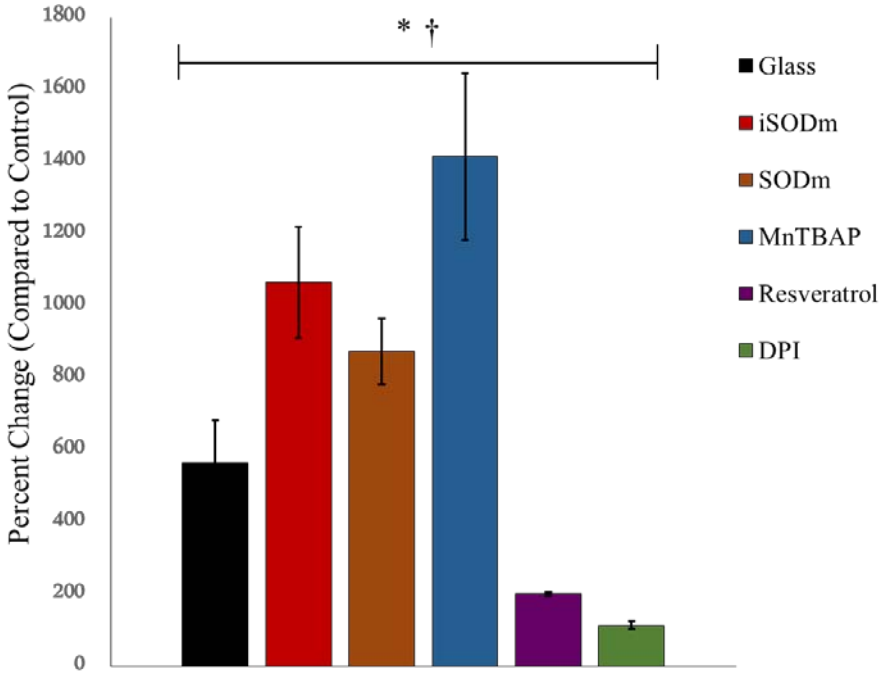

Figure 2-7 Griess Assay of LPS/IFN Stimulated HAPI Cells.

Production of NO is only reduced with pre-treatment of the antioxidant resveratrol. Both cationic and anionic catalytic antioxidants result in a dramatic increase in measured NO (± SEM; n = 3; * $p < 0.05$ compared to glass control; † $p < 0.05$ compared to group control).

Conversely resveratrol decreased NO output by more than 400% when compared to control. NO output altogether was nearly abolished with the NADPH oxidase inhibitor DPI. Although DPI has been shown to inhibit NADPH, it has been demonstrated in the literature that iNOS activity requires at least a threshold level of NADPH oxidase activity.[29] In addition when

looking at immunostaining for iNOS, a significant increase in iNOS signal in LPS/IFNγ cells plated on iSODm coated samples is observed (Figure 2-8). The relative increase in NO output as measured by the Griess Assay as well as an increase in iNOS staining may be a result of the decrease of NO breakdown (as opposed to increase in production), which is dependent upon superoxide concentration (and subsequent formation of peroxynitrite)[25].

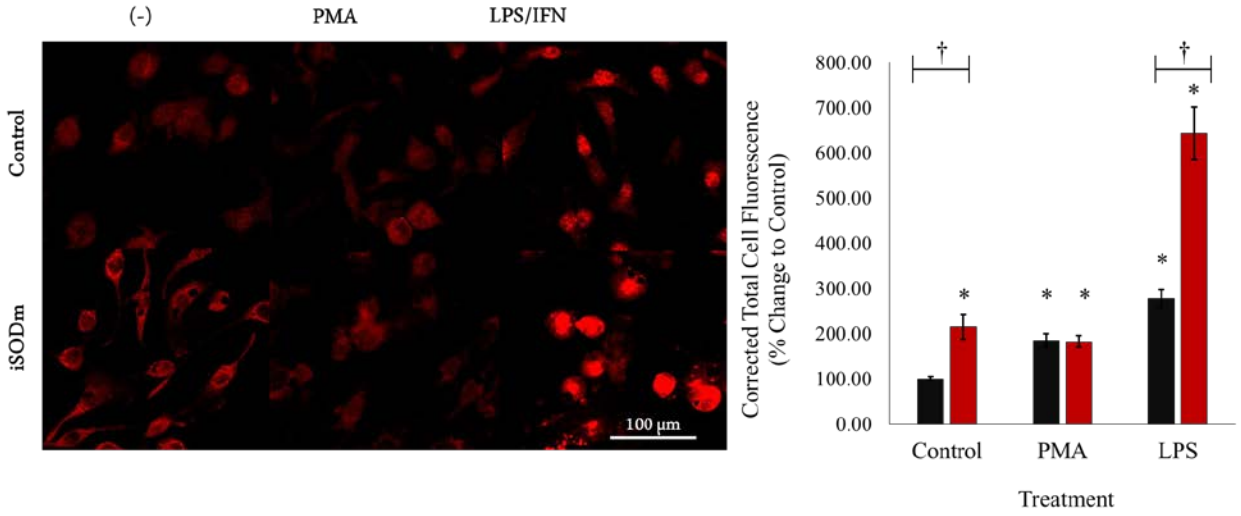

Figure 2-8 Up-Regulation of iNOS Following LPS/IFN Stimulation.

Staining of iNOS is pronounced following LPS stimulation of microglia cells. The corrected total cell fluorescence is significantly higher in microglia following LPS stimulation, and significantly increased further in cells plated on the iSODm coating (± SEM; n = 20; * $p < 0.05$ compared to glass control; † $p < 0.05$ compared to glass treatment).

As shown in previous literature, the presence of superoxide scavenger such as SOD, NO breakdown is drastically decreased resulting in overall higher levels.[42] In addition, NO, like superoxide, operates in a positive feedback method resulting in an increase in iNOS activity. These findings are consistent with what has been found on iSODm confirming the expected efficacy of the SODm. In addition, higher levels of arginase is observed in cells plated onto the iSODm coating (Figure 2-9). Arginase activity is typically related to the 'wound-healing'

response of macrophage type cells and mostly inversely proportional to iNOS activity. However, in this case high levels of both proteins for cells plated on the iSODm coating is observed. While iNOS is traditionally viewed as part of the inflammatory response, it has been shown that without superoxide production (and subsequent peroxynitrite production) NO levels can be cytoprotective and important for angiogenesis.[64]

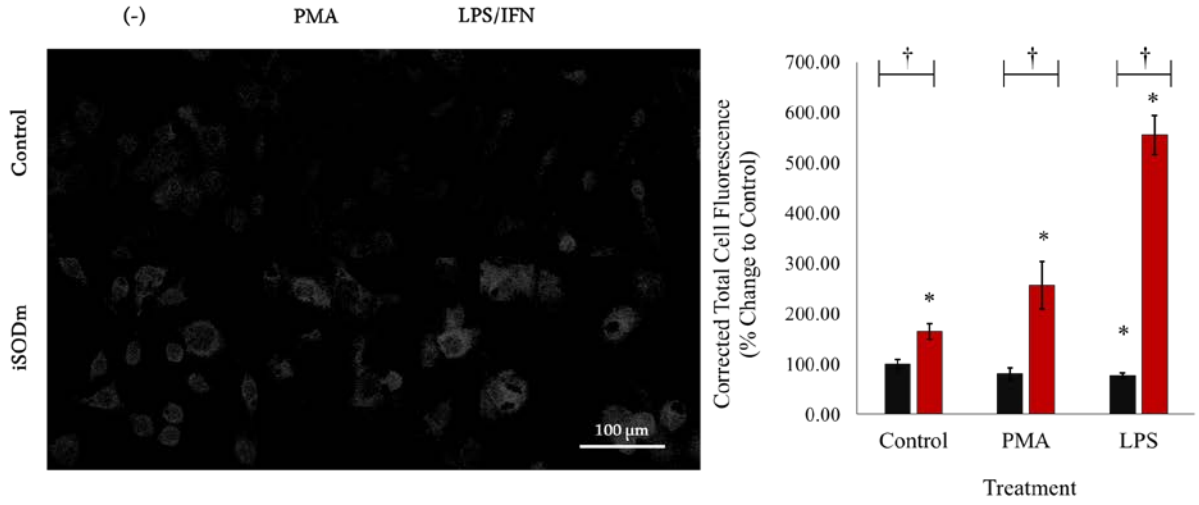

Figure 2-9 Arginase Activity in Stimulated HAPI Cells.

Arginase staining decreases upon stimulation of LPS in control microglia cells as measured by the corrected total cell flourescence. However, arginase signaling is significantly increased across all iSODm coating groups (± SEM; n = 20; $*$ $p < 0.05$ compared to glass control; † $p < 0.05$ compared to glass treatment).

Using the superoxide probe, dihydrorhodamine (DHR), the intracellular levels of superoxide were evaluated (Figure 2-10). The non-fluorescent probe, DHR readily crosses the cell membrane; however, once it has reacted with superoxide it becomes the charged and fluorescent compound, rhodamine 123. When rhodamine 123 (Rho123) is produced via the reaction between DHR and superoxide in the cell, Rho123 can no longer leave the cell, enabling

detection of intracellular superoxide levels. Microglia significantly increase in fluorescence following both PMA and LPS stimulation, suggesting an important role in intracellular superoxide levels in the inflammatory response. However, when cells are plated on the iSODm coating, these intracellular levels of superoxide are abolished.

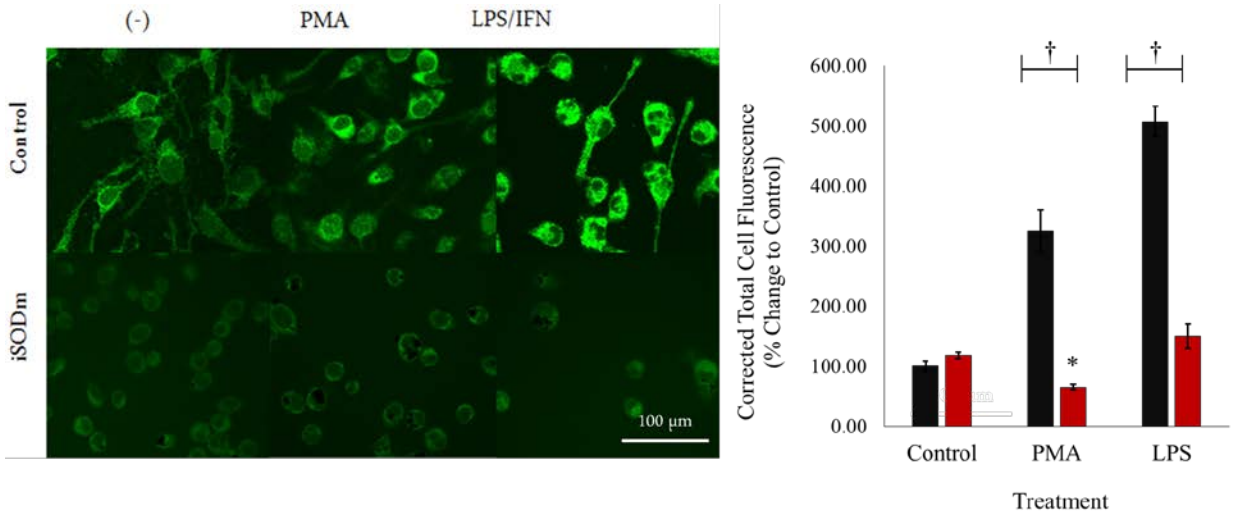

Figure 2-10 Intracellular ROS

Upon stimulation with either PMA or LPS, intracellular superoxide increases in microglia according to a significant increase in corrected total cell fluorescence. In all cases, intracellular superoxide is decreased in cells grown on the iSODm coating (± SEM; n = 20; * $p < 0.05$ compared to glass control; † $p < 0.05$ compared to glass treatment).

To determine effect of the iSODm coating on neuron growth, primary cortical cultures were grown on the iSOD coated coverslips for up to 5 days. Neuron density and neurite outgrowth were both dramatically increased on iSODm (**Figure 10**Figure 2-11). Besides the antioxidant properties of the coating, neuron growth has also been demonstrated to be improved with positively charged surfaces such as poly-lysine which shares structural similarities with the iSODm complex. In addition, the adhesion of microglia is decreased when plated on the iSODm surface. These two added benefits may provide optimal tissue interaction of implanted materials containing the iSODm.

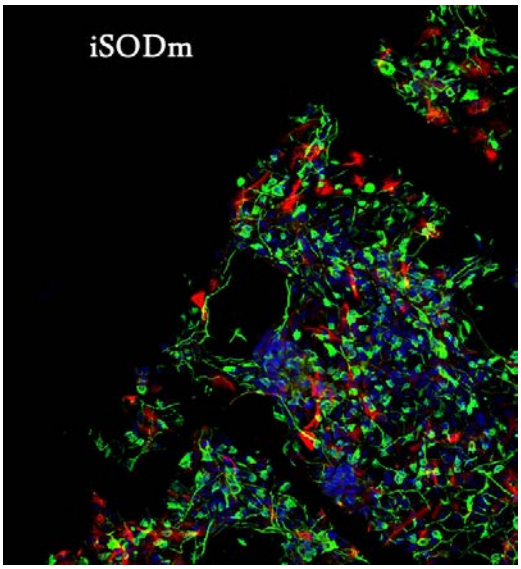

Figure 2-11 Neuron Growth on iSODm Coated Substrates.

Primary neuron cultures grown on samples with or without the iSODm coating. After 5 days, few primary microglia (β-III tubulin) or astrocytes (GFAP) are observed on glass samples. Both Neurons and Astrocytes readily grow on the cationic iSODm surface and neurite outgrowth is observed.

Neural electrodes modified with iSODm were implanted into rat cortex to investigate the effects an antioxidant coating had on neuron survival near the implant. Neuron numbers were compared between unmodified and iSODm-modified electrodes by counting cell bodies indicated by NeuN staining, a neuron cell body specific histological stain. Neuron cell bodies were counted within a 250 μm radius from the implant location and binned by 50 μm (Figure 2-12). Neuron death and neurodegeneration has been previously observed as early as 24 hr after neural electrode implant.[13] When comparing unmodified electrodes with iSODm-modified electrodes, improvements in neuron density from the first bin (0 μm – 50 μm) to the last bin counted (175 μm – 250 μm) were observed. Based on the *in vitro* results, improvements in the neuron density near the neural electrode could be a result of the dual antioxidant and neuron promotion of the iSODm coating. However, improvements to the neuron density beyond the closest region to the implant are more likely to be a result of solely the antioxidant effects of the coating. As has been described previously, neurodegeneration around neural implants spreads out from the 'kill zone' and continues to decrease cell density as far out as 300 μm.[13] The improvement in neuron survival may be due to the decrease in the oxidative environment in the nearby tissue. No differences were observed in microglia (OX42), astrocyte (GFAP), or bleeding (IgG) between unmodified and iSODm coated probes (Figure 2-13, Figure 2-14, Figure 2-15, respectively). However, considering the increase in neuron density around the iSODm coating, these cell types may be in different activation states.

Traditionally, as tissue dies near the implant site, oxidative species would be produced both by necrotic cells and inflammatory glial cells.[64] These oxidative species have been implicated in neurodegeneration and would explain the long-distance decrease in neuron density previously observed. However improvements of the neuron density as far out as 250 μm would

indicate a disruption of this oxidative pathway. Therefore, not only does the iSODm surface prevent local oxidative damage, but halts the neurodegeneration chain that decreases more distal neuron damage.

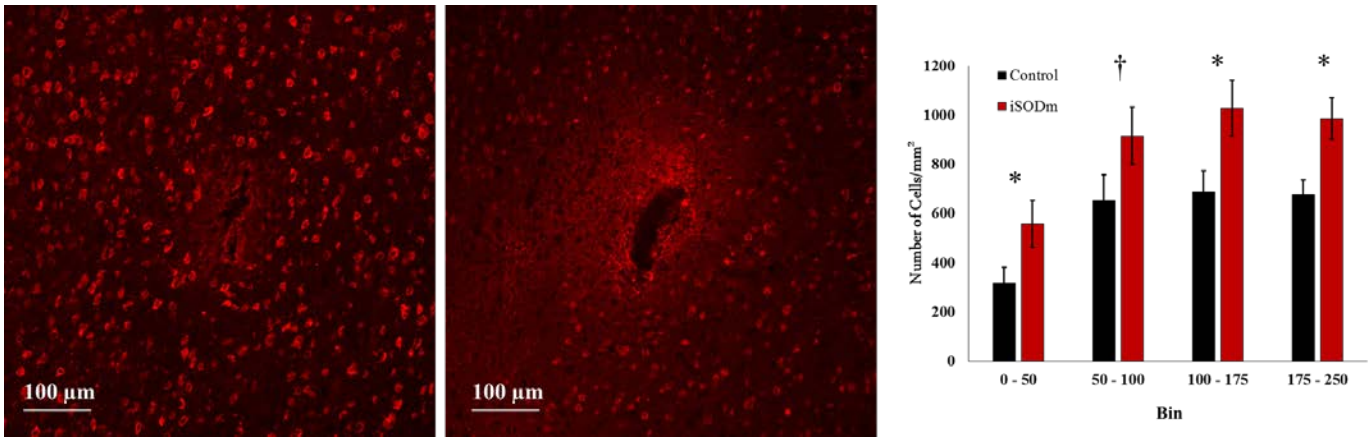

Figure 2-12 Neuron density is increased around iSODm coated Electrodes after 1 week.

Neuron density was calculated by counting neuron cell bodies (NeuN) at a cortical depth of ~ 1000 µm. Neuron count is significantly higher around probes coated with iSODm in the most crucial 50 µm as well as beyond 100 µm (± SEM; $n = 15$; $* p < 0.05$; † $p < 0.1$).

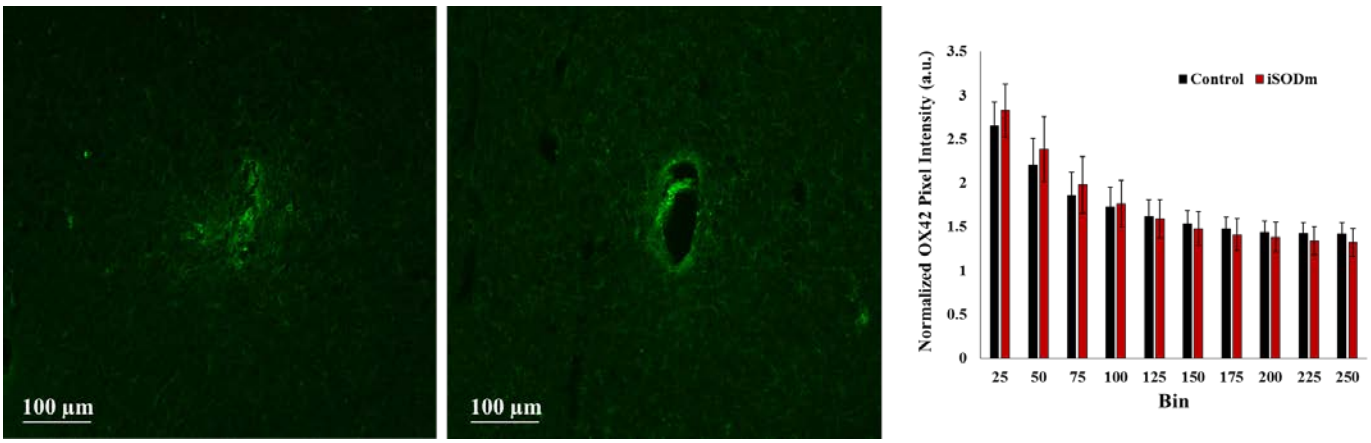

Figure 2-13 OX42 Analysis around Neural Implant after 1 Week.

Normalized intensity analysis of OX42 staining was compared between unmodified and iSODm coated probes. The intensity difference was compared at 50 µm. There was no significant difference between unmodified and iSODm coated neural probes after 1 week (± SEM; *n* = 15).

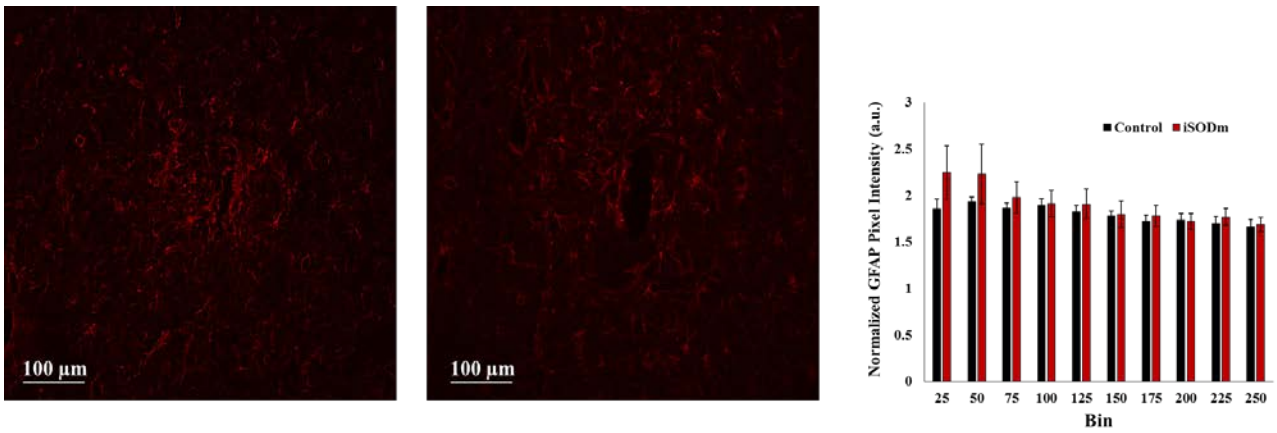

Figure 2-14 GFAP Analysis around Neural Implant after 1 Week.

Normalized intensity analysis of GFAP staining was compared between unmodified and iSODm coated probes. The intensity difference was compared at 50 µm. There was no significant difference between unmodified and iSODm coated neural probes after 1 week (± SEM; *n* = 15).

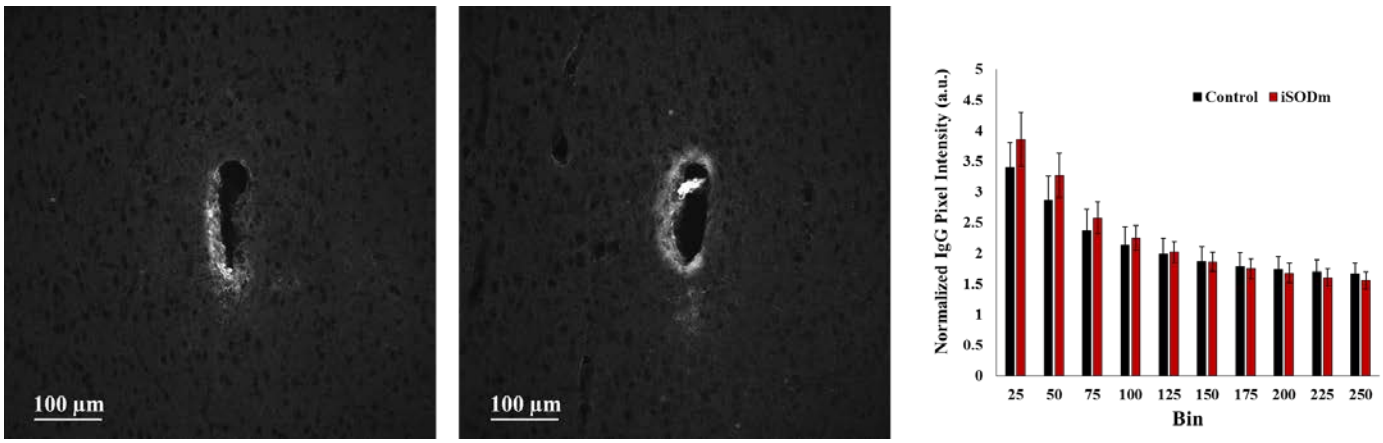

Figure 2-15 IgG Analysis around Neural Implant after 1 Week.

Normalized intensity analysis of IgG staining was compared between unmodified and iSODm coated probes. The intensity difference was compared at 50 µm. There was no significant difference between unmodified and iSODm coated neural probes after 1 week (± SEM; n = 15).

2.4 CONCLUSIONS

A novel coating based on a newly synthesized antioxidant superoxide dismutase mimic was successfully created. By preparing a functionalized SODm derivative, a monolayer coating was created that demonstrated similar antioxidant effectiveness as $Mn^{III}TE\text{-}2\text{-}Pyp^{5+}$. Based upon *in vitro* results, the iSODm coating effectively reduced superoxide production resulting in a decreased oxidative environment which ultimately affected HAPI cell signaling pathways by altering protein levels of iNOS, NADPH oxidase, and arginase. Following 1 week of the implant, a significant increase in neuron density around the implant site surrounding iSODm coated arrays was observed. Furthermore, the effective radius of the iSODm coating was surprisingly beyond 250 µm from the implant location suggesting an interruption of the typical

neurodegeneration propagation. The development of this iSODm coating could ultimately result in the improvement of implantable neural devices and aid in the clinical progression of these technologies.

3.0 ELECTROCHEMICAL DETECTION OF SUPEROXIDE USING HEMIN-ADSORBED GRAPHENE OXIDE NANOCOMPOSITE

3.1 INTRODUCTION

Clinical application of neural prosthetic devices is prevented due to the poor performance of these devices at chronic time points.[1, 2, 9, 11] While neuron proximity is the most important necessity for effective recording of neural signals, implanted devices are susceptible to an inflammatory response that creates a harsh environment. Often times an increased inflammatory response is coupled with progressive neuron cell death, or neurodegeneration.[13] Understanding the mechanism behind neurodegeneration near neural implants is of the greatest importance in designing new strategies for improving the tissue-electrode interface. To aid such fundamental understanding, real-time evaluation of the tissue state would be desired.

Neurodegeneration is a complicated process by which neurons die, often as a result of either acute trauma or chronic disorders. While the underlying mechanism for the onset of neurodegeneration may be different depending upon the condition, it is widely accepted that reactive species such as free radicals, reactive oxygen species (ROS), or reactive nitrogen species (RNS) play a role in mediating the cellular death.[3, 4, 41, 65, 75] One of the most studied reactive oxygen species, superoxide (O_2·-), can result in cellular damage through direct lipid peroxidation, DNA degradation, or the creation of even more highly reactive chemical species.[76-

[78] For this reason understanding the relative concentrations of superoxide is critical to diagnosing oxidative damage *in vivo* and in real-time.

Directly detecting levels of ROS/RONS *in vivo* is a complicated task considering the species high rate of reactivity. Furthermore, current histological methods provide only indirect evidence of oxidative damage, and often are incapable of demonstrating the dynamic role that oxidative species play in trauma.[13, 66] Given the need for real-time assessment of oxidative species, and the electrochemical origin of free-radical species, electrochemical detection methods have been a focus of ROS/RNS research. Often sensors are designed with inorganic sensing elements that are capable of interacting directly with oxidative species through electron-transfer (Figure 3-1).[79-82]

$$O_2^- + M^{3+} \longrightarrow O_2 + M^{2+}$$
$$O_2^- + 2H^+ + M^{2+} \longrightarrow H_2O_2 + M^{3+}$$
$$2O_2^- + 2H^+ \longrightarrow O_2 + H_2O_2$$

Figure 3-1 Superoxide Oxidation-Reduction Scheme

Efforts into designing electrochemical sensors for superoxide production have been limited by poor incorporation of sensing elements into prepared devices.[79] Using our laboratories previously established methods for improving sensor electrochemical properties, we have designed a hemin-based sensor through direct adsorption onto poly(3,4-ethylenedioxythiophene) (PEDOT) and graphene oxide (GO) nanofilms. We have demonstrated that using our hemin-PEDOT/GO electrode we are not only capable of detecting biologically relevant concentrations of superoxide, but also able to effectively detect superoxide during a mechanistic study.

3.2 MATERIALS AND METHODS

3.2.1 Chemicals and Materials

For preparation of electrode nanocomposites, hemin, 3,4-Ethylenedioxythiophene (EDOT), and phosphate buffered saline (PBS, pH 7.4, 10 mM sodium phosphate and 0.9% NaCl) were purchased from Sigma-Aldrich. Graphene Oxide was purchased from Cheap Tubes Inc. (Brattleboro, USA). The reagents for preparation of the superoxide generation system, xanthine oxidase, pterine, catalase, and cytochrome C were also purchased from Sigma-Aldrich.

3.2.2 Electrochemical Apparatus

Electrochemical pretreatment and deposition of nanocomposite films were performed with a Gamry Potentiostat, FAS2/Femtostat (Gamry Instruments). For electrochemical detection experiments using cyclic voltammetry, an Autolab Potentiostat/Galvanostat PGSTAT128N was used. For both electrode preparation and electrochemical detection experiments, a traditional three-electrode setup was used. Glassy carbon electrodes served as a working electrode, a silver/silver chloride reference electrode (CH instruments) and a platinum foil counter electrode.

3.2.3 Preparation of Hemin-PEDOT/GO Electrode

Electrochemical deposition of a PEDOT/GO nanocomposite was performed on glassy carbon electrodes (GCE, 3 mm diameter, CH instruments). Prior to electrodeposition, electrodes were pre-treated. GCEs were first polished with 1.0 and 0.05 μm alumina slurries and then directly

ultrasonicated in ethanol followed by Millipore H_2O. Finally, GCEs were electrochemically pretreated in 1 X PBS using both chronoamperometry (1.8 V for 200s) as well as cyclic voltammetry (5 cycles, 0.3 V to 1.3 V at 100 mV/s s.r.). Following pre-treatment, all GCEs were stored in 1X PBS to maintain the hydrophilicity. Conducting polymer films were prepared as described previously by our laboratory.[62] PEDOT/GO films were electrochemically deposited using a deposition solution containing EDOT (0.2 M) and GO (10 mg/mL). Charge limited deposition proceeded by applying a constant potential of 1.0 V until the charge density reached 100 mC/cm^2 on the macroelectrode.

Following electrochemical deposition, Hemin-PEDOT/GO electrodes were prepared by adsorbing hemin directly onto PEDOT/GO coated GCEs. A stock solution of hemin was first prepared by dissolving hemin in minimal 1 M NaOH and diluting with 1 X PBS to a final concentration of 10 mg/mL. The PEDOT/GO electrodes were submerged in the hemin solution for 24 hr and rinsed repeatedly with Millipore water prior to beginning sensor experiments.

3.2.4 Electrochemical Characterization of Hemin-PEDOT/GO Electrode

For characterization of Hemin-PEDOT/GO films as well as sensing experiments, cyclic voltammetry (CV) was used. A multiplex setup was used to decrease variance from solution preparation and to measure the same superoxide solutions with different probes. CV was measured from -0.8 V to 0.8 V at a scan rate of 100 mV/s. Initial CV measurements before and after electrode preparation were collected in 1 X PBS.

3.2.5 Generation of Superoxide

A similar enzymatic generation system for superoxide production was used as described above (2.2.5). However, the setup was modified to account for the iterative nature of the experimental design. For each trial, 3 different electrodes were placed into an electrochemical cell containing 15 mL of PBS. In between each addition to the cell, electrochemical measurements were collected. The first addition was catalase and xanthine oxidase, followed by pterine. For mechanistic studies, additional quantities of xanthine oxidase were added.

3.2.6 Analysis of Superoxide Detection Data

For analysis of the electrochemical data collected from the sensor experiments, a custom MATLAB script was created. The script allowed for measurement of both the peak cathodic and anodic current at the selected potentials. The oxidation and reduction peaks used to measure the response to superoxide production were -0.400 mV and -0.450 mV, respectively.

3.3 RESULTS AND DISCUSSION

3.3.1 Design and Characterization of Hemin Electrode

Metalloporphyrins are of great importance to the biosensor field given their effectiveness as sensing elements for a variety of electrochemical reactions. In particular the sensing of reactive oxygen (ROS) and nitrogen species (RNS) is highly dependent upon metalloporphyrin-based sensors given the affinity of these inorganic complexes for highly reactive free radicals.[79]

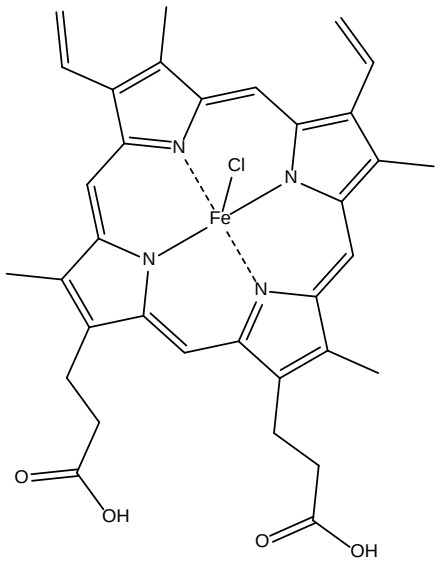

Figure 3-2 Structure of Hemin Sensing Element

Superoxide is one of the most interesting of the ROS/RNS given the radicals importance on cellular respiration, cell signaling, neurodegeneration and a wide variety of diseases.[54] Using the protoporphyrin IX complex, hemin, scientists have worked on creating sensors to measure superoxide protection in real time (Figure 3-2).[56, 83, 84] However, detection currents are often low

and un-reliable. To that end, we have designed a hemin-based sensor for the detection of biologically relevant superoxide concentrations.

To create a highly sensitive sensor for superoxide we relied upon direct adsorption of hemin onto PEDOT/Graphene Oxide electrodes. By combining the properties of the conducting polymer PEDOT with the unique chemical properties of graphene oxide, our laboratory has previously demonstrated an improvement biosensing application based on the nanocomposite's effects on impedance, charge-storage-capacity (CSC), etc.[62, 63] Furthermore, the structure of graphene oxide results in excellent adsorption of hemin and similar metalloporphryin complexes (Figure 3-3).[84] Given the highly conjugated structure for both the porphyrin backbone of hemin and graphene oxide itself, it is no surprise that tight adsorption of hemin onto graphene oxide and related structures has been demonstrated.[85]

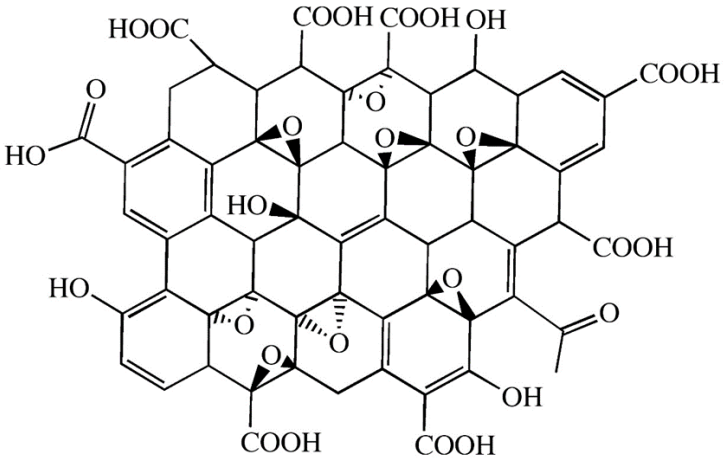

Figure 3-3 Structure of Graphene Oxide

Like other metalloporphyrin complexes, the oxidation and reduction of the iron conjugated at the center of the porphyrin results in clearly visible oxidation/reduction peaks using cylic voltammetry experiments. Prior to preparation of a hemin-PEDOT/GO electrode, we

verified the oxidation/reduction peaks in a 1 mM solution of hemin in PBS. Using glassy carbon electrodes we observe oxidation/reduction peaks centered at ~ - 400 mV (Figure 3-4).

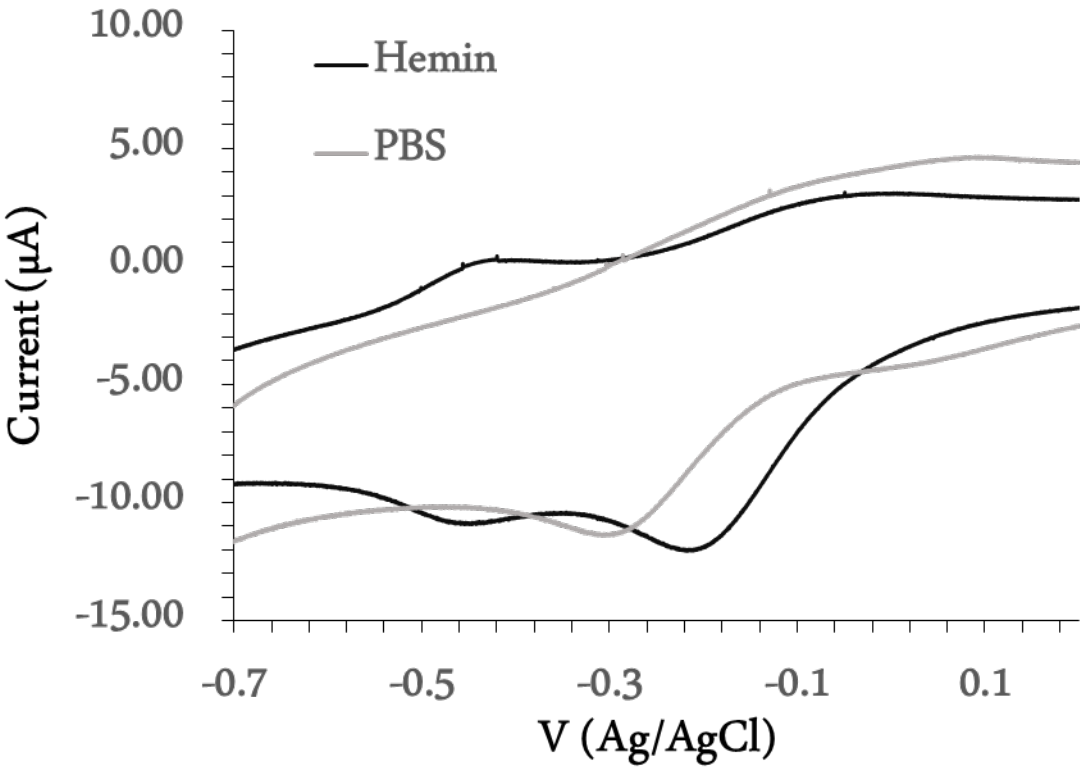

Figure 3-4 CV Curve for Hemin

The CV curve of 10 mM hemin in a PBS solution using a glassy carbon electrode (scan rate = 100 mV/s).

Once we had confirmed the hemin peaks in solution, we focused on preparation of a hemin-PEDOT/GO electrode. Deposition of PEDOT/GO film onto working macro-electrodes resulted in broadening of the CV curve; however, no peaks were present at the expected location of the hemin peaks (Figure 3-5). The increased area within the PEDOT/GO film is consistent with our previous work and reflective of an increase in the charge storage capacity of the film.[62] For preparation of the final sensor, hemin was directly adsorbed onto the surface of the

PEDOT/GO film. As expected, hemin peaks were evident with a redox potential at ~ -400 mV. However, interestingly, the charge storage capacity of the film decreased. Considering no delamination or visible damage of the films was observed following the adsorption, the change to the electrochemical properties of the film must be a result of the interaction between hemin and the graphene oxide in the film. It is well established that hemin complexes interact with graphene oxide and graphene-like materials through π-π interaction of the aromatic porphyrin rings and the aromatic graphene backbone. Among other properties, this results in an increase in the electron transfer rate and charge dissipation rate of the film, both of which may decrease the charge-storage capacity as observed here.[60, 86]

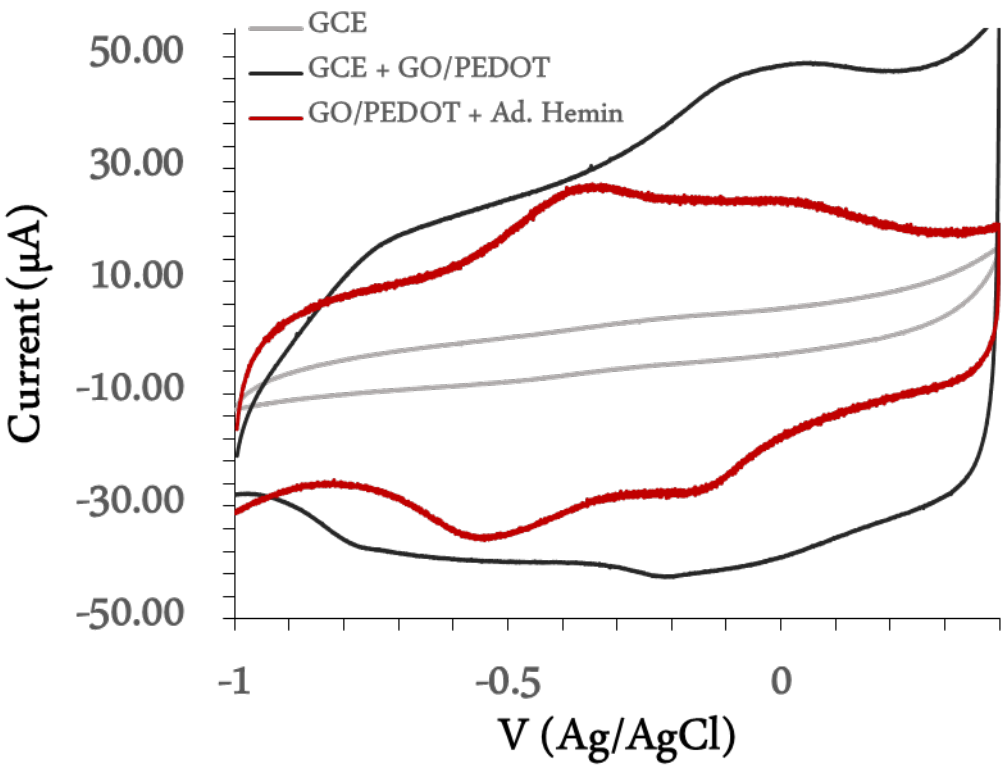

Figure 3-5 Adsorption of Hemin onto GO/PEDOT GCE

A comparison of the CV curves for a glassy carbon electrode (grey), a glassy carbon electrode following electrodeposition of GO/PEDOT (black), and a GO/PEDOT electrode following hemin adsorption (red).

3.3.2 Sensitivity of Hemin Electrode

The capacity for electrochemical detection of superoxide was compared between two electrode types. Hemin was directly adsorbed onto glassy carbon electrodes with or without a PEDOT/GO electrodeposited film. For the generation of superoxide, the xanthine oxidase system was used. The xanthine oxidase system is an effective method for generating a consistent rate of superoxide for a long duration.[25] Traditionally, xanthine oxidase is used in conjunction

with xanthine as a substrate. The oxidation of xanthine to uric acid results in the production of superoxide into the system. However, considering the antioxidant nature of uric acid itself, a slightly altered system was used. Pterine was used in place of xanthine to produce superoxide to prevent any antioxidant interferrants affecting the superoxide concentrations.[25]

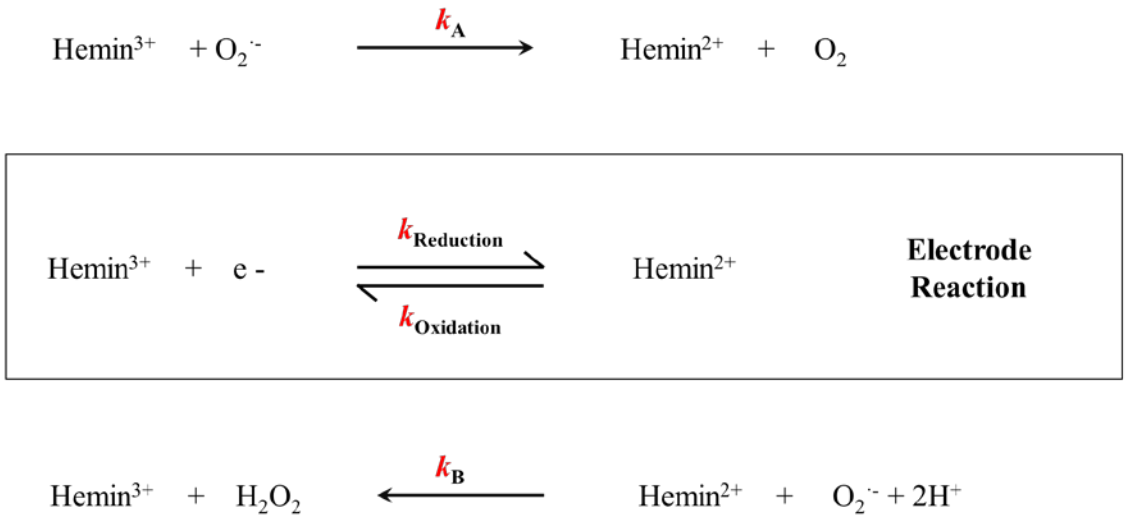

Figure 3-6 Hemin Electrochemical Sensing Scheme

The detection of superoxide by the hemin-PEDOT/GO electrode is dependent upon the electrochemical reaction occuring at the metal-centered metalloporphyrin (Figure 3-6). The oxidation and reduction peaks observed on the CV curves are a result of the oxidation and reduction of the iron ion at th center of the porphyrin complex. As the potential scans negatively, reduction of the hemin^{3+} complex occurs resulting in cathodic current. Conversely, as the potential scans positively, oxidation of hemin^{2+} results in the anodic peak. The relative magntidue of the cathodic and anodic peaks depend upon the concentrations of hemin^{3+} and hemin^{2+}, respectively. In the presence of superoxide, the concentrations of redox 'eligible' hemin

is artificially increased. Again, let us consider the case when the potential is scanning negatively. Following reduction of hemin^{3+}, [hemin^{2+}] is high. When superoxide is available, hemin^{2+} is oxidized back to hemin^{3+}. The superoxide-mediated formation of hemin^{3+} in turn increases the cathodic current as more hemin^{3+} is available for electrochemical reduction. The overall increase in current is dependent upon the concentration of superoxide as dictated by the reaction with rate k_B. Similarily, if we examine the scenario when scanning positively, the opposite is true. Superoxide artificially increases the concentration of hemin^{2+} by reducing hemin^{3+}.

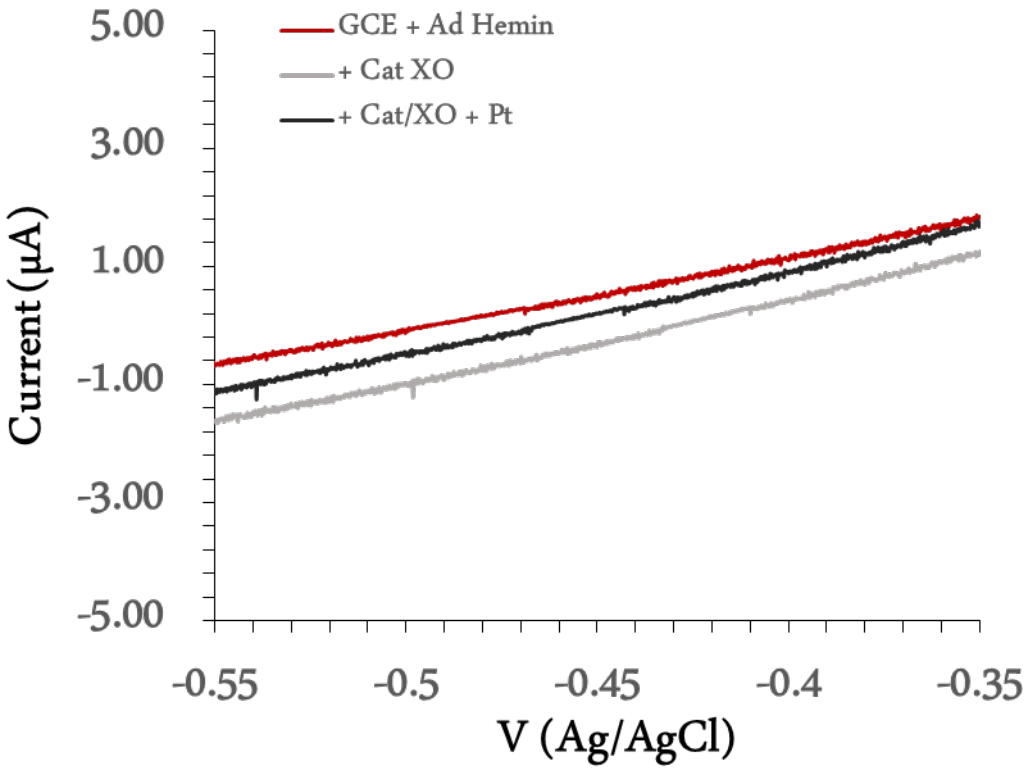

Figure 3-7 Superoxide Detection form GCE Electrode

The CV scan range used to detect superoxide shows no increase in the presence of superoxide for glassy carbon electrodes with or without hemin adsorption (scan rate = 100 mV/s).

Catalase was added to the system to remove any interfering hydrogen peroxide that would be produced by the spontaneous dismutation of superoxide. Reagents for the xanthine oxidase system were added in a step-wise fashion to determine the specificity of the detection setup. The current at the oxidation peak at ~ - 400 mV was evaluated for superoxide detection. Without a PEDOT/GO film, little hemin is adsorbed to the surface of pristine glassy carbon electrodes as indicated by the lack of any true peak in the base CV (Figure 3-7). Furthermore, little to no increase in current is observed following addition of the superoxide generating system.

As demonstrated earlier, hemin is effectively adsorbed to the surface of PEDOT/GO mainly due to the strong π-π interactions between the porphyrin and the graphene oxide. After addition of xanthine oxidase and catalase to the system we see no response in the oxidation peak at – 400 mV. However, effective superoxide detection is observed following addition of the substrate pterine. Once pterine is added to the reaction, a consistent increase in peak current is observed (Figure 3-8).

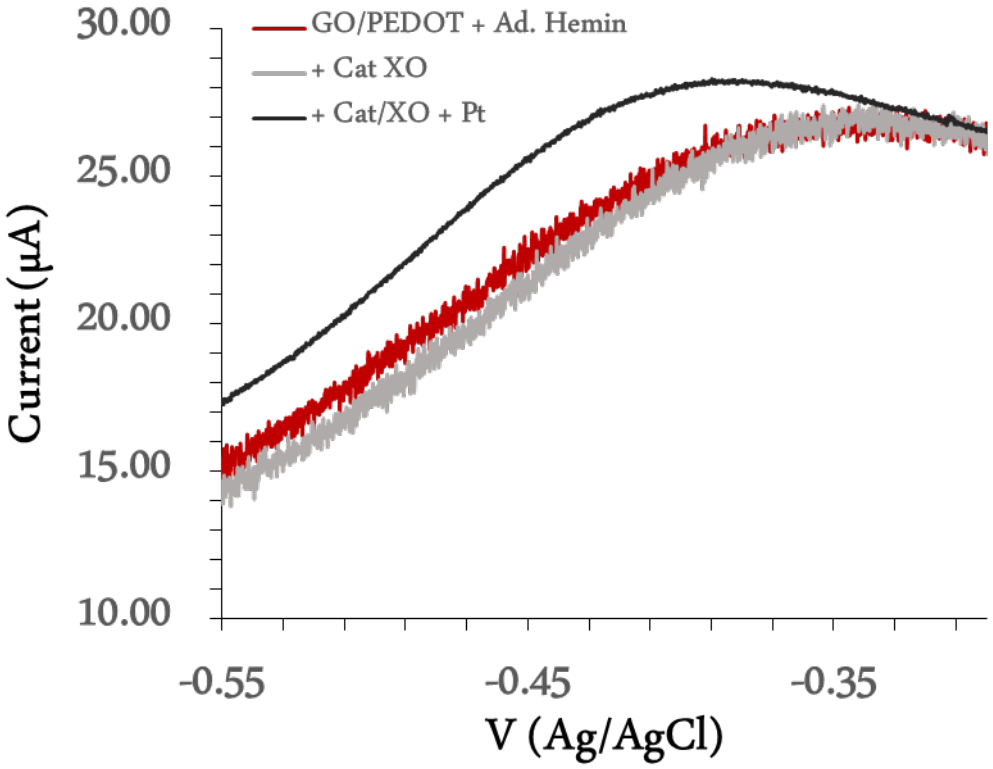

Figure 3-8 AdHemin-GO/PEDOT Sensing Peak

In the presence of superoxide (generated by 30 mU/mL xanthine oxidase with 100 µM pterin) the oxidation peak of hemin adsorbed on the GO/PEDOT electrode increases in detectable current.

Finally, by ranging the concentration of xanthine oxidase and measuring the peak current response, a calibration curve was constructed for the hemin sensor (Figure 3-9). The hemin-GO/PEDOT sensor showed linear sensing capabilities at low concentrations of xanthine oxidase, roughly 10 fold lower than previously constructed sensors.[56]

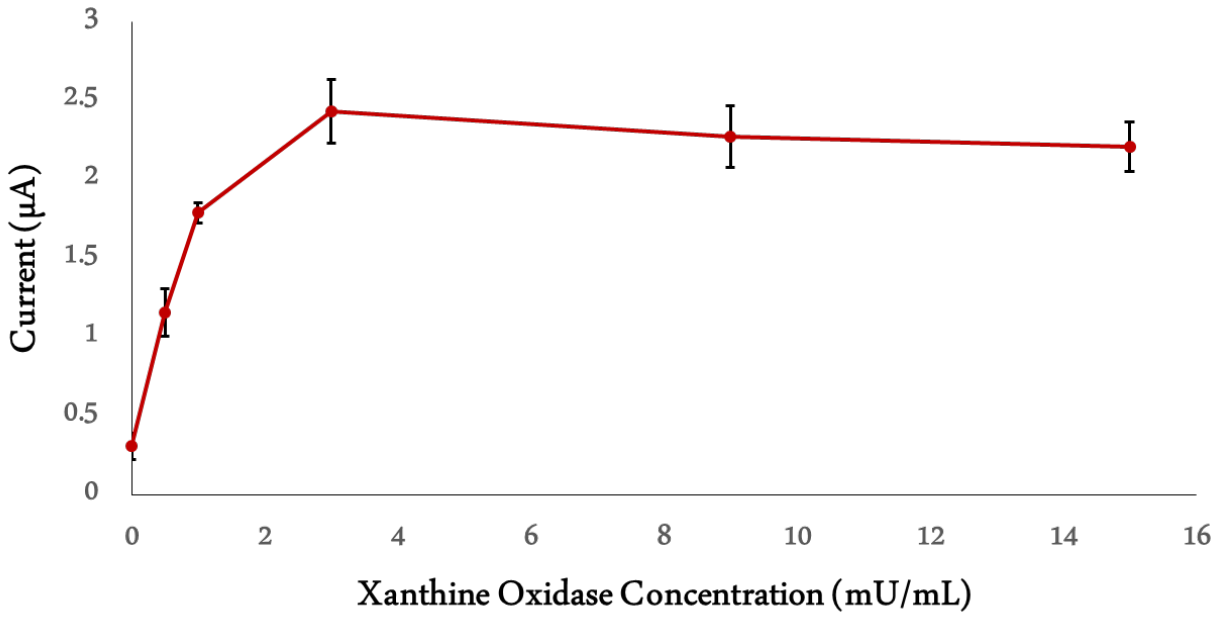

Figure 3-9 Calibration Curve for Hemin-GO/PEDOT Sensor.

The peak current increase measured by the Hemin-GO/PEDOT sensor was plotted vs concentration of xanthine oxidase (± SEM; *n* = 3).

3.3.3 Use of Hemin Electrode for Mechanistic Superoxide Study

To evaluate the performance of the hemin-PEDOT/GO electrode, we completed a mechanistic study of the xanthine oxidase-pterin superoxide generating system. As mentioned previously, the xanthine oxidase system is a widely accepted method for producing biologically relevant sources of superoxide.[25, 30] When the enzyme substrate is kept high in excess, the rate of superoxide production is maintained at a consistent rate (rate = k_1) until the substrate concentration is diminished (Figure 3-10). However, as the production of superoxide increases, the probability of spontaneous dismutation also increases (rate = k_2) until the two reactions are in equilibrium. With the addition of catalase, the product of spontaneous dismutation, hydrogen peroxide, is immediately removed. At equilibrium, the concentration of superoxide is constant until the concentration of pterin is diminished.

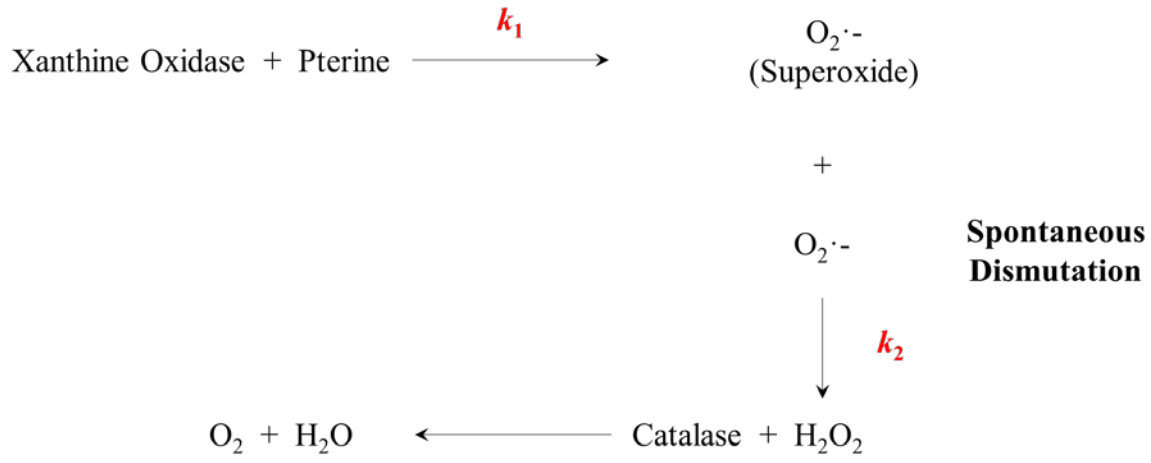

Figure 3-10 Superoxide Production and Dismutation Scheme

By measuring the electrochemical detection of superoxide using the hemin-PEDOT/GO electrode, we were able to map out the mechanism described above (Figure 3-11). To track the production of superoxide over time, the peak current (substracted from baseline) was plotted across time. After the addition of catalase and xanthine oxidase to the system, the peak current remained stable with a small electrochemical drift. Without pterine the rate of superoxide production is $k_1 \sim 0$ and there is not production of superoxide. However, following injection of pterine into the system, there is a short-lived time period where $k_1 > k_2$. During this interval, superoxide concentrations are increasing through the xanthine oxidase-pterin reaction and we observe an increase in peak current detected by the sensor. As the concentration of superoxide increases, the rate of spontaneous dismutation rapidly increases until the point when $k_1 \sim k_2$. The reaction has reached equilibrium and the hemin-PEDOT/GO sensor maintains a constant current. Small impulses of xanthine oxidase are not great enough to break through the equilibrium conditions until a large enough bolus is added. Once the xanthine oxidase concentration is increased enough, the rate of the production of superoxide is greater than the maximum dismutation rate ($k_1 >> k_2$). At this point superoxide generation increases and we observe a dramatic upswing in the peak current measured by the hemin-PEDOT/GO sensor. The current increases until the pterin substrate is exhausted at which point superoxide generation ceases, dismutation dominates, and the peak current begins decreasing back to pre-superoxide levels. Not only is the sensor effective at predicting the well-understood xanthine oxidase mechanism, but cytochrome C assay data is in support of the xanthine oxidase-pterin mechanism (Figure 3-11 insert).

In a separate sample, cytochrome c is added to the xanthine oxidase-pterin reaction. As superoxide is generated, cytochrome c is oxidized and increases in absorbance. Once the pterin is used up, cytochrome c oxidation stops, following a similar timeline to our electrochemical detection.

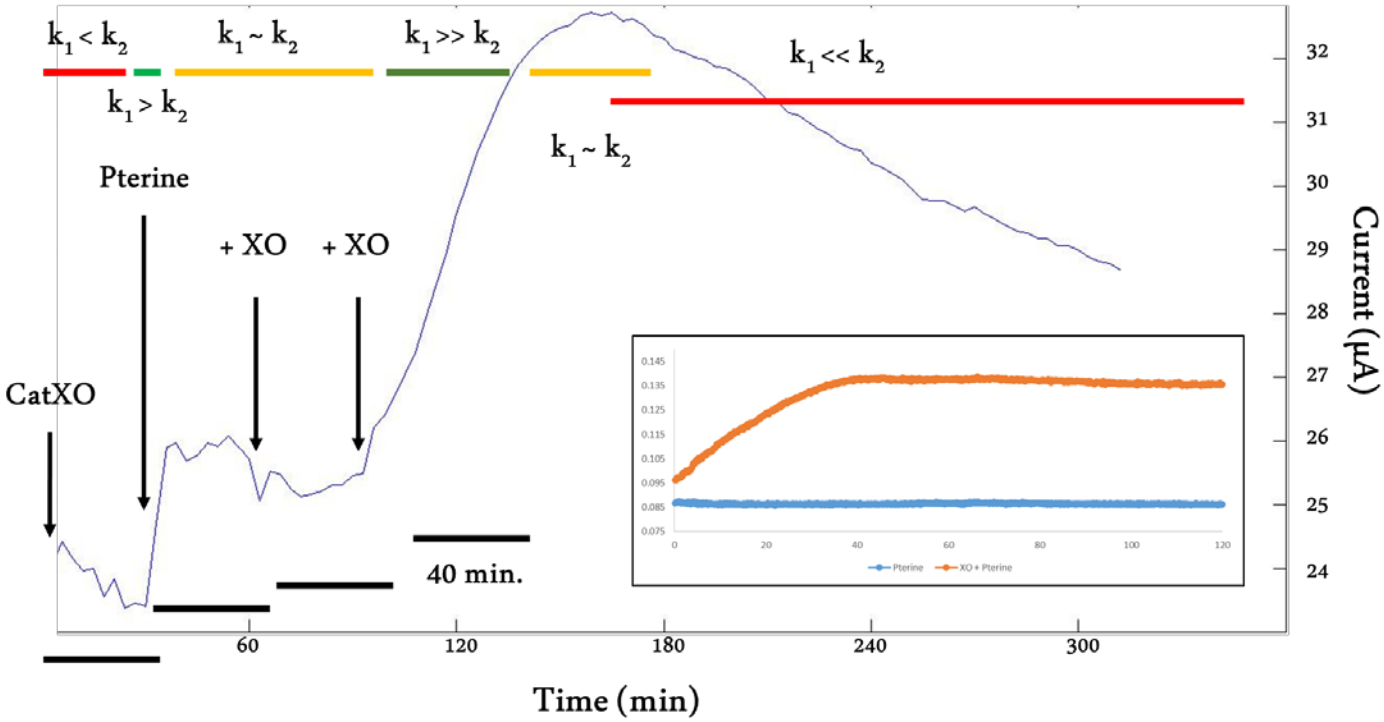

Figure 3-11 Superoxide Detection of Enzymatic Generating System

The Hemin-GO/PEDOT electrode was used to detect superoxide in a mechanistic study. Following the addition of the superoxide reagents, CV (scan rate 100 mV/s) were recorded. The peak current at – 0.55 V was plotted over time. The rate constants, *k*, refer to the constants described in Figure 3-9. (Insert) The absorption of cytochrome C was used to measure superoxide generated by the xanthine oxidase system. In the presence of xanthine oxidase and pterine, cytochrome C reduction occurred for ~ 40 min.

3.4 CONCLUSION

The ability to detect superoxide with a new hemin-PEDOT/GO electrode was investigated in this work. Unlike in the case of pristine glassy carbon electrodes, the metalloporphryin complex, hemin, readily adsorbed to the surface of PEDOT/GO modified electrodes as evidenced by the oxidation and reduction peaks of the electrode. The hemin modified PEDOT/GO electrode was effective at detecting superoxide production using cyclic voltammetry measurements. By recording peak oxidation current across time we were able to effectively track superoxide production using a mechanistic study of the enzymatic production of superoxide using xanthine oxidase. The development of this superoxide sensor could provide a new tool for understanding the role that superoxide plays in neurodegeneration as well as a diagnostic tool for determining the oxidative environment near chronically implanted neural electrodes.

4.0 IMPROVED L1 COATING OF PAYRLENE NEURAL ELECTRODES FOR USE IN NON-HUMAN PRIMATES

4.1 INTRODUCTION

The improvement of the tissue-electrode interface is essential for the development of promising neuroscience-based technologies such as neural prosthetic devices. One method of improving the abiotic/biotic interface is to 'mask' the implanted device using biomimetic strategies. Developed in our laboratory, a protein coating based on the neural cell adhesion molecule L1 has demonstrated great potential for improving neural electrode devices.[46, 47, 87, 88]

L1 is a glycoprotein and part of the immunoglobulin family. Important during the development and differentiation of new neurons, L1 functions as a homophilic binding site between neurons.[48, 49, 89] Due to the ability to improve neurite attachment and outgrowth *in vitro*, L1 has previously been used to improve the interface between silicon-based neural probes and the CNS.[46, 47] Furthermore, L1 coatings decrease microglia and astrocyte recruitment, thereby reducing the main sources of ROS/RNS found in the inflammatory response.[46] However, while L1 coatings have effectively improved the implantation site of silicon-based probes, little work to this point has been done on other probe designs and materials more closely ready for clinical use.

Poly(2-chlor-para-xylylene), or parylene C (PC), is a widely used material due to its unique combination of flexibility, electrical properties, as well as biocompatibility.[90-96] For this reason, biomedical devices including pace makers and deep brain stimulating electrodes often use parylene C as the insulating material. However, in the field of neural prosthetics, the performance of PC-based chronically implanted neural electrodes remains too unreliable for clinical acceptance.

Using the FDA-approved penetrating micro-electrode array, the BlackRock Utah Array, we applied our L1CAM biomimetic coating to a device of clinical relevance. By using the Utah Array, we have translated our technology from silicon-based applications to the unique chemistry and practical design of the PC-based array. We analyzed the performance of PC coated samples for chemical modification, *in vitro* bioactivity, and electrophysiological testing in a non-human primate neural prosthetic model.

4.2 MATERIALS AND METHODS

4.2.1 Chemicals and Reagents

For isolation of L1 via immunoaffinity chromatography, 3((3-chloamidopropyl)dimethyl-ammonio)-propanesulfonic acid (CHAPS) was purchased from Anatrace, and all other reagents and solvents including diethylamine hydrochloride and (4-(2-hydroxyethyl)-1-piperazineethanesulfonic acid) (HEPES) were purchased from Sigma Aldrich. The parylene dimer (dichloro-di-para-xylylene, SCS DPX-C) was purchased from Specialty Coating Systems (Indianapolis, Indiana). E18 Sprague-Dawley rat cortices were purchased from BrainBits, LLC and all other cell culture supplies were purchased from Fisher Scientific.

4.2.2 Isolation and Characterization of L1 Neural Adhesion Molecule

Isolation of the cell adhesion molecule L1 from both *Sprague dawley* and *Rhesus macaque* was achieved using the same method described previously.[49] An affinity column containing the 5H7 monoclonal antibody bound to Affi-Gel 10 (Bio-Rad) was supplied by Carl Lagenaur for purification of L1. Brain tissue was first homogenized and isolated using sucrose gradient differential centrifugation. Membrane tissue was then solubilized in 1% CHAPS and centrifuged at 40,000 g for 30 min to remove any contamination. The membrane solutions are run over the column at a rate of approximately 1 mL/min. For elution of the bound L1 from the column, 0.1 M diethylamine at a pH of 11.5 was used. Neutralization of the eluted L1 soltuion was achieved using 1 M (4-(2-hydroxyethyl)-1-piperazineethanesulfonic acid) (HEPES) in H_2O. L1 samples were used as prepared and required no additional processing. Elution from the column was tracked using the Amdio Black method. L1 solutions were spotted directly onto nitrocellulose membrane and submerged in Amido Black (MeOH) to visualize protein spots.

4.2.3 Parylene Coating

Chemical vapor deposition of parylene onto glass substrates was completed using the Special Coating Systems Labcoter® 2 Parylene Deposition System. For the deposition of > 1µm thick parylene-C, 1 g of DPX-C dimer was loaded into the deposition system. Prior to coating, glass coverslips (Dia. 8 mm, #1.5 Thickness, Electron Microscopy Sciences, Hatfield PA) were ultrasonicated in acetone then MeOH/H_2O. Samples were kept in a closed container prior to and after parylene C coating.

4.2.4 L1-Modification of Parylene Samples

Parylene-C coated coverslips were coated with L1 protein via protein adsorption. Dry parylene-C coated coverslips were exposed to oxygen plasma (30 W) for 1 min (Harrick Plasma, PDC-001). Oxygen flow into the plasma chamber was maintained at 1 L/min and pre-flushing of the chamber occurred for 15 min prior to generating plasma. Successful oxygen plasma was indicated by the blue hue of the plasma (as opposed to the traditional purple hue from air plasma). Oxygen plasma treated samples were immediately used for protein adsorption. Isolated L1 samples were applied directly onto parylene-C samples and allowed to adsorb for 1 hr. Samples were washed repeatedly with 1 X PBS prior to being used for cell culture experiments. To determine the coating quality, some samples were washed with 0.5 % Tween in PBS.

4.2.5 Primary Neuron Culture

Primary neuron cultures were prepared as described above (2.2.7). L1 bioactivity after preparing parylene-C coated samples, was verified with primary neuron cultures. E18 Sprague-Dawley rat cortices were purchased from BrainBits, LLC. The rat cortices were triturated with a 1 mL pipette and removed from the Hibernate MediaTM via centrifugation at 800g for 1 minute. Cells were re-suspended in Neurobasal (Fisher)/B27 (Gibco)/0.5 mM glutamine/25 µM glutamate (Sigma-Aldrich) culture medium and plated directly onto either coated samples in 48-well cell culture plates (Corning Costar) at a density of 2.5 x 10^5 cells/cm^2. Cells were grown in culture for 5 days at 37 °C in 5% CO2 and media was refreshed after day 3. Cells were fixed with 4% paraformaldehyde for 10 min. and stained with the monoclonal antibodies against neuronal class III β-tubulin (Covance).

4.2.6 Preparation of Functional Probe Coating Chamber

For coating of the BlackRock (Salt Lake City, Utah) Arrays, a special coating fluidics chamber was designed. The device for coating micro-electrodes (CoatME) was designed to support the array during ETO sterilization, storage, L1 coating, and transport. Using stereolithography (SLA) 3D printing, the chamber was printed with the WaterShed XC 11122 material, which is classified as biocompatible and chemical resistant according to ISO 109993. For *in vivo* experiments, a Utah array was loaded into the CoatME and sterilized with ETO. On the day of surgery, the array was exposed to oxygen plasma for 1 min (30 W, Harrick Plasma, PDC-001). The prepared monkey L1 solution was injected into the chamber using sterile tools in a sterile culture hood, and first passing through a 0.2 μm sterile filter. After 1 hr, the chamber was flushed with sterile PBS and transported to the surgical room.

4.2.7 Impedance Characterization of Utah Arrays

Impedance spectroscopy was used to monitor the electrode interface quality over time. Using an Autolab potentiostat, complex impedance was measured on a monthly basis by applying a 25 mV RMS sine wave with frequencies varied logarithmically from 10 Hz to 100 kHz. Impedance measurements were extracted at 1 kHz and plotted over time. The average 1 kHz impedance magnitude was averaged across all electrodes on an array and compared with using the Student’t t-test for unpaired data (p-value of < 0.05 is considered significant).

4.2.8 Non-Human Primate Implantation of Utah Arrays

Utah arrays with or without the L1 coating were transported for non-human primate implantation in the laboratory of Dr. Andy Schwartz. The 10 x 10 Blackrock Arrays were implanted bilaterally into the M1 cortex of the *rhesus macaque* using a similar approach as described previously.[97] All surgery was completed under gas isoflurane anesthesia. A craniotomy was created above the target location, in the M1 area. Both arrays were positioned near the implant location and fixed to the surface of the skull. In the case of the L1 array, it was kept moist by spraying sterile saline directly onto the probe. After the dura was opened, and the target area identified, the arrays were inserted using a pneumatic inserter. The original bone flap was replaced prior to closing of the craniotomy. All animal use and procedures were in accord with the Institutional Animal Care and Use Committees at the University of Pittsburgh. In addition to impedance measurements, electrophysiology recordings were measured using a Tucker-Davis Technologies (TDT) system.

4.3 RESULTS AND DISCUSSION

4.3.1 L1 Isolation and Bioactivity

The isolation of the L1 cell adhesion molecule (L1CAM) and L1CAM homologues has been achieved in a wide variety of species including rodents, fish, and even the fruit fly.[48, 49, 89] However, to our knowledge the isolation and characterization of non-human primate L1CAM has yet to be described. While isolation of *Sprague dawley* L1CAM has been successfully

isolated and applied to neural electrodes in our laboratory[46, 47], the isolation of *Rhesus macaque* L1CAM was essential to prevent unwanted immunogenic responses in non-human primate neural electrode studies.

L1CAM protein from *Rhesus macaque* was isolated from fresh brain tissue. Following membrane extraction, protein fractions were collected in 1 mL aliquots and tested for protein content, purity, and bioactivity. Fractions that indicated positive protein content using the Amido Schwartz protein detection assay were evaluated for protein purity using sodium dodecyl sulfate-polyacrylamide gel electrophoresis (SDS-PAGE). Isolation of pure L1CAM samples were verified by SDS-PAGE bands at ~ 240 kDa and ~ 150 kDa (Figure 4-1). L1 is a ~ 200-250 kDa cell surface protein; however, the band at ~ 150 kDa is a cleavage product that becomes cleaved in some cases endogenously to produce soluble L1.[48, 50, 51]

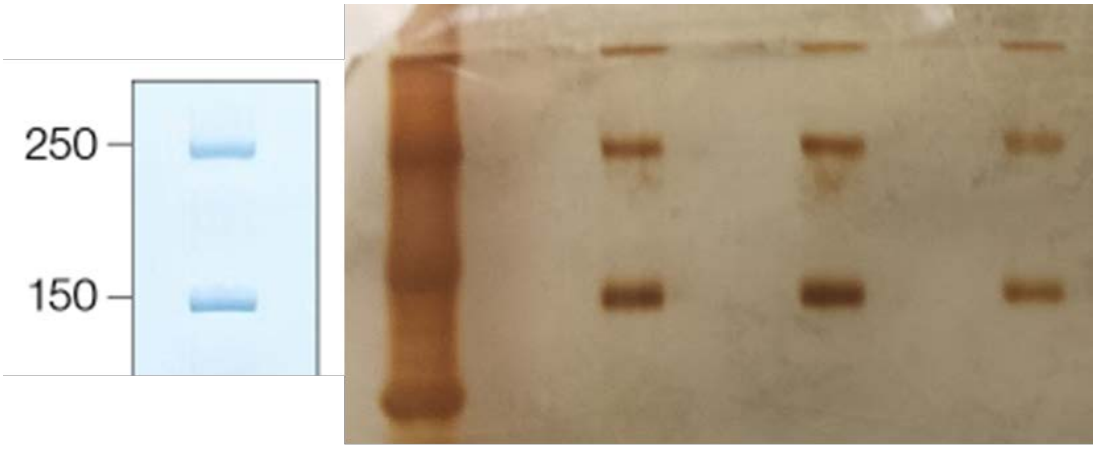

Figure 4-1 SDS-PAGE Gel of Isolated L1 Fractions

Lane 1 is a protein standard and lanes 1 – 3 are isolated L1 fractions. Pure L1 fractions can be identified by clear bands at ~ 240 kDa and ~ 150 kDa.

Bioactivity of purified L1CAM fractions was verified using a simple neuron cell culture assay on nitrocellulose coated samples. Following preparation of nitrocellulose coated culture dishes, aliquots from each isolated L1CAM fraction were pipetted onto designated areas on the dish. Fractions that resulted in 'spots' with robust neuron coverage were deemed bio-active. In spots without L1CAM, no neurite growth is observed. In addition to neurite growth on bioactive L1CAM spots, neuron growth was characterized by un-fasiculated extension. Unlike other adhesion proteins like laminin, L1CAM results in individual axons readily growing across the coated surface (Figure 4-2). Whereas in the case of laminin, cell bodies often spread out onto the surface and axons bunch into fasciculated fibers.[48]

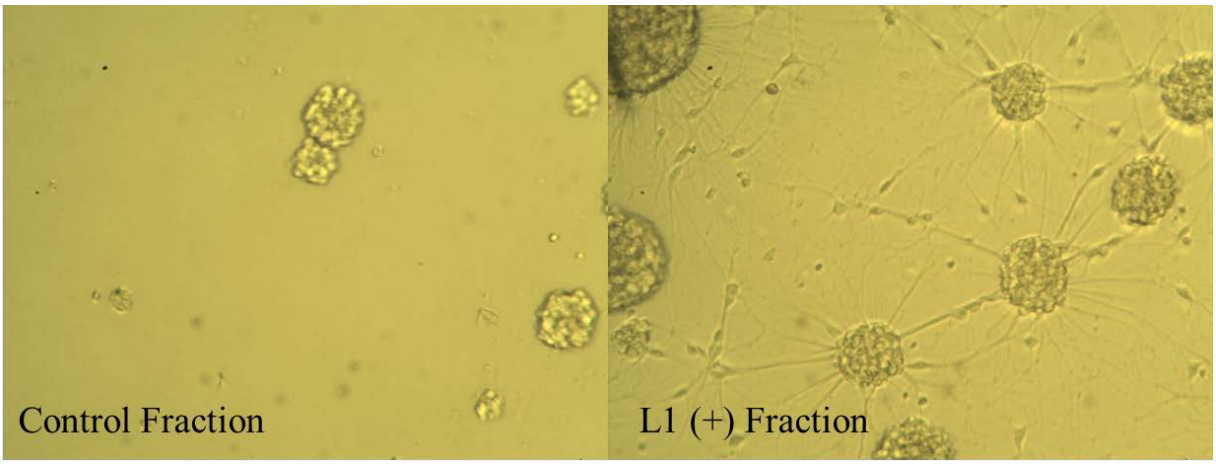

Figure 4-2 Nitrocellulose Bioactivity Assay for Isolated L1 Fractions

Primary rat neurons were cultured on nitrocellulose samples with or without monkey L1 protein. Cells plated directly onto nitrocellulose show minimal neurite extension. Conversely, L1 coated nitrocellulose results in neurite extension of cells.

4.3.2 Preparation of L1-Modified Parylene C Substrates

Parylene materials are frequently the coating of choice for implantable devices from peacemakers to neural electrodes such as the BlackRock Utah Array.[92] Halogenated derivatives like parylene C (chlorinated along the –para position) are increasingly implemented for these applications because of the relative ease of further chemical modification (Figure 4-3).[90]

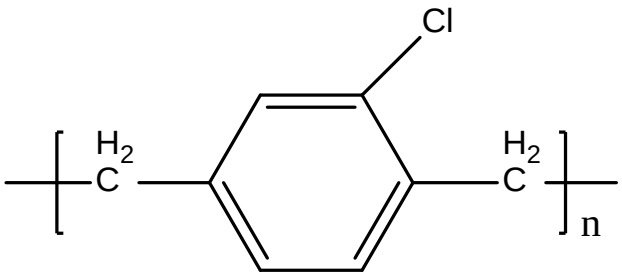

Figure 4-3 Structure of Parylene C

Prior to modification of the parylene-C on the BlackRock Utah Arrays for *in vivo* studies, it was necessary to demonstrate effective modification of parylene substrates and subsequent bioactivity of coated samples. Plasma treatment of polymer surfaces has proved to be a vital tool for materials scientists. Plasma treatment can be used to alter several characteristics of a surface including biocompatibility, cell adhesion, and protein adsorption.[91, 98] When the plasma is generated from O_2 gas, the hydrophilicity of the treated surface is increased through the generation of C-O and O=C-O bonds onto the surface. While the oxidation reaction sites are generally nonspecific, following O_2 plasma treatment of parylene-C samples we observe sharp increases in oxygen content using XPS as indicated in the O 1s peak (Figure 4-4).

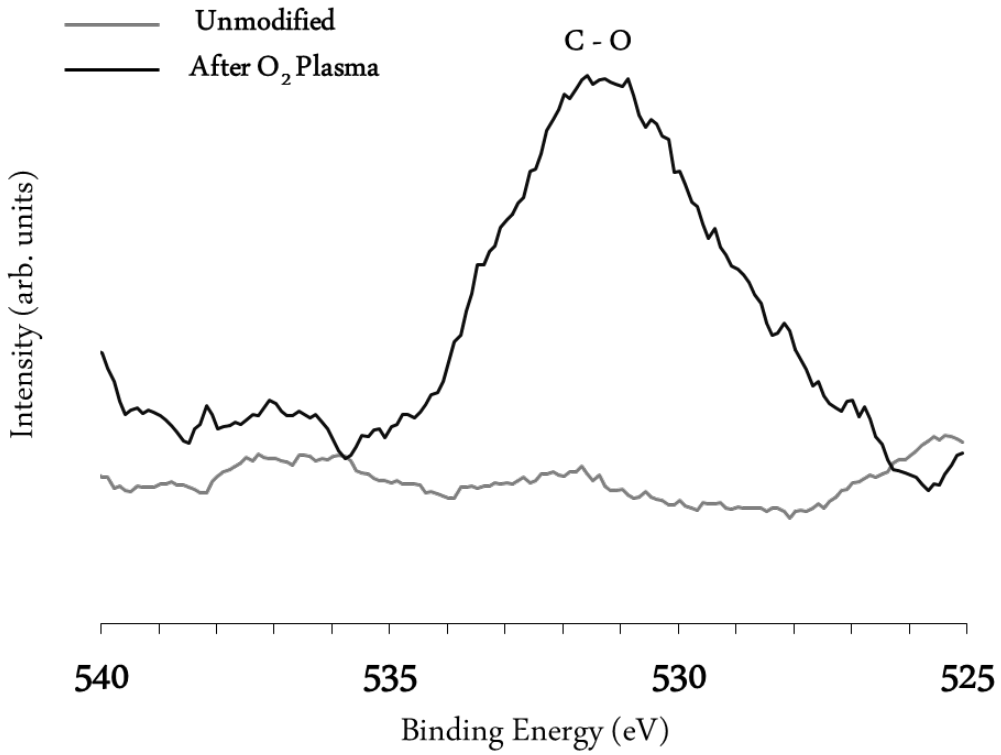

Figure 4-4 XPS Analysis of Parylene C Oxygen Peaks.

Following oxygen plasma treatment of unmodified parylene C substrates, incorporation of oxygen is indicated via the XPS peak at 532 eV.

Chemical state information is an effective method for determining changes to surface chemistry. Following O_2 plasma treatment we observe a shifting of traditional Carbon 1s peaks due to the increase in C-O and O=C-C bonds. Following oxygen plasma treatment XPS experiments demonstrate the formation of carboxylic acid groups on the parylene-C surface (Figure 4-5).

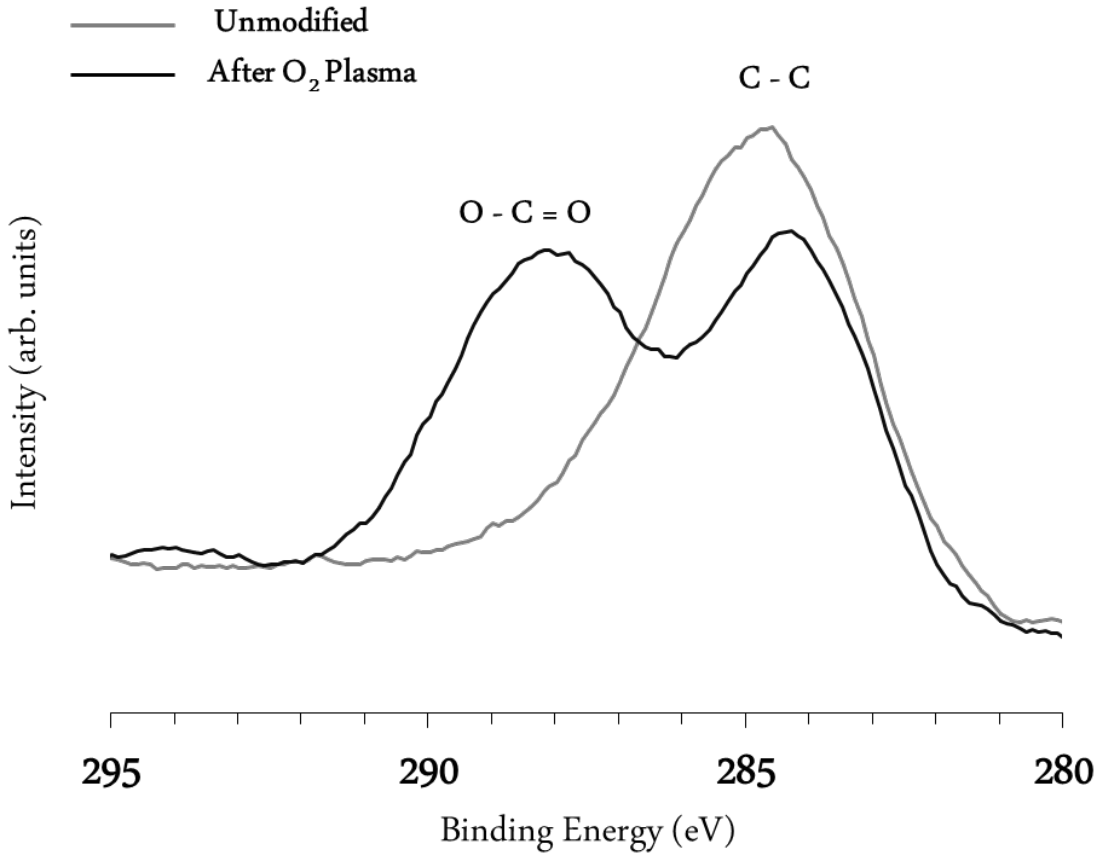

Figure 4-5 Depth of Parylene C Surface Modification.

Formation of carbonyl carbon is observed in XPS (289 eV) after exposure to oxygen plasma treatment.

Typically an increase in the hydrophilicity of a surface via O_2 plasma treatment decreases the level of protein adsorption onto the surface. However, this is not the case with glycoproteins such as L1CAM where the opposite trend is in fact observed.[99, 100] To verify this trend, we adsorbed L1CAM on parylene-C samples with or without prior O_2 plasma treatment (Figure 4-6). As is the case with L1-positive spots on nitrocellulose, neurons plated onto L1-coated parylene-C samples were characterized with long neurite projections. This L1-specific growth is not observed on pristine parylene C samples. Few neurites are ever observed on unmodified PC samples. The extensive neurite projection demonstrates effective preparation of a L1-PC coating with retained bioactivity.

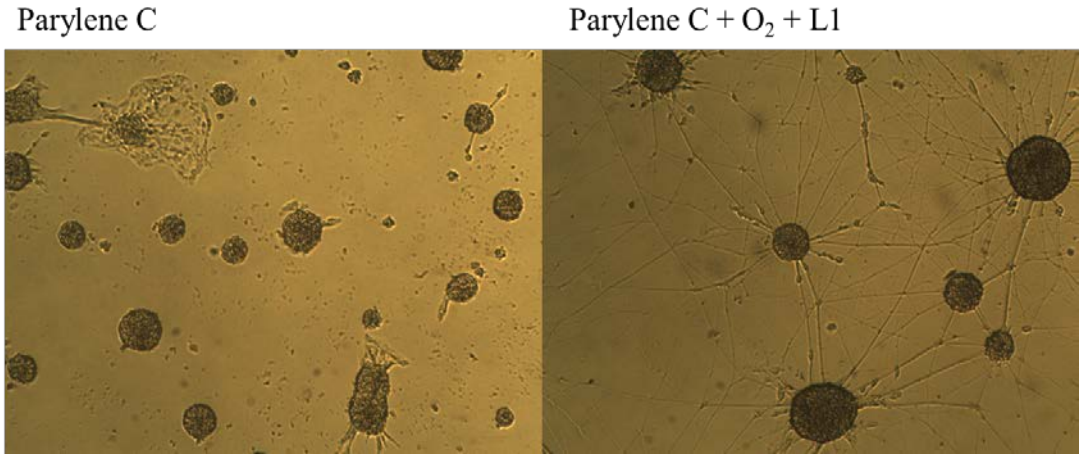

Figure 4-6 L1 Adsorption on Oxygen Plasma Treated Parylene C

Primary rat neurons were cultured on parylene C substrates with or without L1 adsorption. Adsorption of L1 was achieved following 1 min exposure to oxygen plasma. Neurons plated onto L1 coated samples demonstrate increased neurite extension.

Dissemination of novel coating strategies for neural implants requires adaptation of traditional coating procedures. To that end, we designed a fluidics-based coating chamber in order to effectively coat BlackRock Utah Arrays without the risk of damaging the delicate microelectrode tips. A biocompatible printing resin (WaterShed XC 11122) was used to 3D print a chamber that would satisfy clinical needs for handling, storage, and coating of neural implants (Figure 4-7).

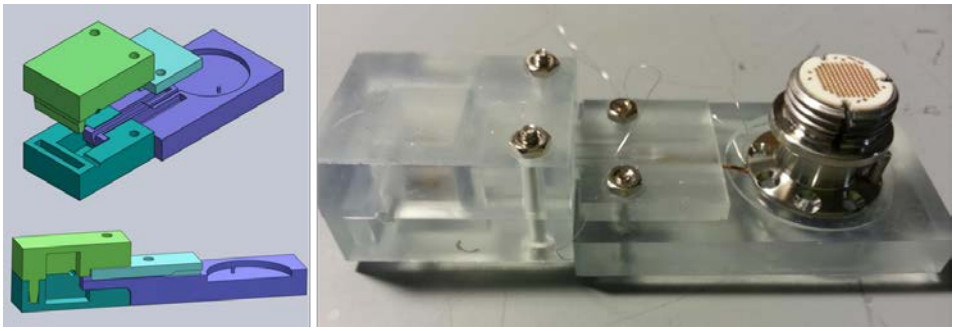

Figure 4-7 CoatME Device for Utah Array Coating Procedure

Prior to *in vivo* studies, we first verified that the CoatME device could effectively coat a BlackRock Utah Array. A Utah Array was loaded into the chamber and exposed to a similar 1 min O_2 plasma treatment as used for previous *in vitro* experiments. Following the plasma treatment, a solution of 100 µg/mL FITC-Albumin was injected into the chamber. Using fluorescence microcopy we demonstrated that fluorescently labeled protein effectively adsorbed to the surface of the array (Figure 4-8).

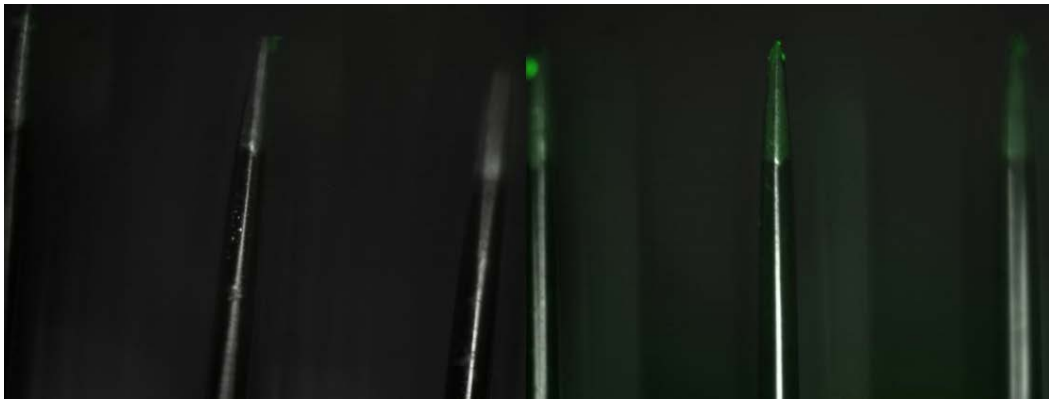

Figure 4-8 FITC-Albumin Adsorption on Surface Treated Utah Array

Following oxygen plasma treatment, FITC-albumin was adsorbed onto Utah Arrays using the CoatMe device. Following adsorption, the green fluorescent FITC-albumin protein is observed using fluorescent microscopy. (Left) Before FITC-albumin adsorption (Right) After FITC-albumin adsorption.

4.3.3 Functional Study of L1-Coated Utah Arrays in Non-Human Primates

To determine the effect of the L1 coating on the recording quality of neural implants, BlackRock Utah Arrays were implanted into the M1 cortical region of the *Rhesus macaque*. To reduce animal variance, control and L1-coated arrays were implanted into the same animal. Utah Arrays were coated using the CoatME device and transported to the lab of Dr. Andy Schwartz where all further surgical procedures and recording sessions were completed. After allowing the animal to recover, recording sessions were completed and neuron units were analyzed using custom Matlab scripts prepared by Dr. Zhanhong Du (Figure 4-9).

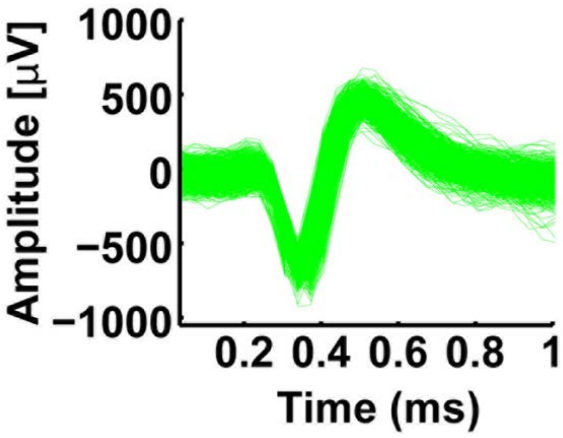

Figure 4-9 Representative Neuron Spike Data

Neural data collected from implanted Utah Arrays was thresholded into spike activity and sorted into isolatable units.

Two non-human primate experiments have been started at this point (a third experiment resulted in early animal termination). The first animal has shown a remarkable improvement in isolatable neuron signals for multiple years following the implant (Figure 4-10). This is in stark contrast to the control array in the same animal which resulted in no recordable data after the first two months (data not shown).

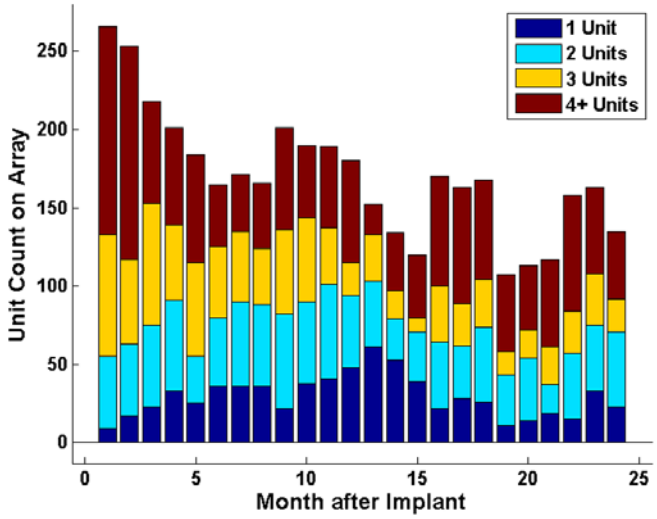

Figure 4-10 Neural Recording of L1 Modified Utah Array

The total number of units recorded form the implanted Utah Array coated with the L1 coating. The uncoated array stopped producing recordable units after 4 months. Units were grouped as the basis of total number of units per electrode from electrodes with only 1 recordable unit (Blue) to electrodes with 4 or more (Red).

Current neuron quality data for the second implanted monkey is not significant; however, the time-point is still early. A noticeable trend is already apparent in the measured 1 kHz impedance data. As early as the first month after the implant procedure, the impedance on the array modified with the L1 coating is significantly higher. While impedance increases can be observed from a result of cellular interactions, without histological data the true mechanism behind this increase is currently unknown.[12] Further recording sessions should elucidate the source of impedance difference between the arrays, and additional monkey implants will help to demonstrate the full effectiveness of the L1 coating on neural recording quality.

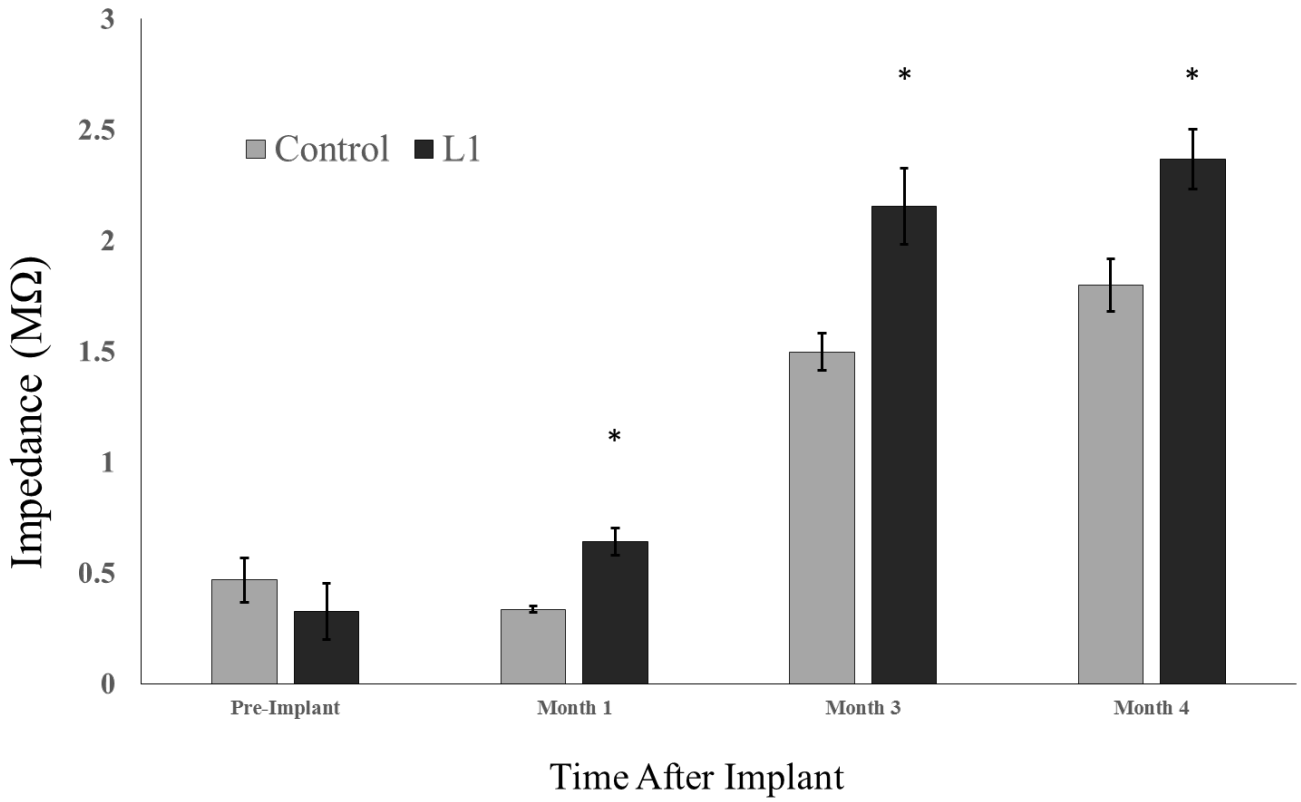

Figure 4-11 Impedance of L1 Coated Array Over Time.

Magnitude impedance (Z), measured at kHz for 4 months following the implantation of L1 coated Utah Arrays. After the first month, the average 1 kHz impedance was significantly higher for the L1 modified probe compared to an unmodified array (± SEM; $n = 96$; * $p < 0.05$).

4.4 CONCLUSIONS

In this study we described the analysis and optimization of a biomimetic coating for parylene C based neural electrodes. Using XPS we demonstrated effective surface activation following oxygen plasma treatment. For the first time we have isolated the L1CAM protein in the non-

human primate, *Rhesus macaque*. Using *R. macaque* L1CAM we effectively coated and demonstrated the bioactivity of coated PC samples *in vitro* using a primary neuron culture. In addition to improve the translational potential of the technology, we developed a new coating device, the CoatME, for handling, storage, and coating of FDA-approved neural electrode arrays. We demonstrated the effectiveness of this device and the benefits of the L1CAM coating by implanting coated Utah Arrays into the *R. macaque* and found a dramatic increase in neural recording quality for several years. By continuing to develop the L1CAM coating, this technology may improve the performance and thus clinical acceptance of neural electrode-based technology in the near future.

5.0 MESOPOROUS SILICA MAGNETIC NANOPARTICLES FOR NON-INVASIVE CONTROLLED DRUG DELIVERY

5.1 INTRODUCTION

Improvement of the interface between chronically implanted neural electrodes and central nervous system tissue (CNS) is believed to be a result of a combination of new coating strategies, electrode design, and treatment of nearby inflammation.[1, 2] Regarding the latter methodology, treatment to the central nervous system is often made difficult by the limitations imposed by the blood-brain barrier (BBB).[101] In order to supply the region near an implant with anti-inflammatory agents, cell survival factors, etc., new drug delivery systems are being actively researched.

One of the most promising methods for drug-delivery into the CNS is through synthetic drug-carriers. Nanoparticles based on mesoporous silica are of great interest considering the biocompatible nature of silica nanomaterials.[57, 102] Furthermore silica nanoparticles can be loaded with a wide variety of drugs, biomolecules, and other compounds of interest for the purposes of drug delivery. However, the inadequate control over drug-release from silica nanocarriers in combination with the lack of targeting specificity limits the potential of these materials.

In order to improve the targeted drug release of silica nanoparticles, magnetic nanoparticles (MNP) are currently being researched.[38, 43, 102] Magnetic nanoparticles have been

successfully incorporated into silica nanoparticles in order to increase the functionality of these nanomaterials. Silica magnetic nanoparticles (sMNP), like silica nanoparticles, can be loaded with a wide variety of molecules and have demonstrated the ability to cross the blood-brain barrier. These properties alone make sMNP a potential vessel for drug-delivery directly into the CNS.[37, 38] Due to the magnetic nature of sMNP, these nanoparticles can be manipulated with magnetic fields to improve the targeting capabilities of the technology. By using static magnetic fields, sMNP have been previously targeted to CNS accumulation.[37] In addition to tissue targeting, drug-release from sMNP can be controlled via application of a high-frequency magnetic fields.[43]

In this work we describe the preparation of drug-loaded nanoparticles for the purpose of drug-delivery into the CNS. We have expanded upon earlier research by optimizing drug-release performance using high-frequency magnetic field. In order to translate the technology for clinical use, we have adapted the technology to work with a 7-Tesla MRI scanner.

5.2 MATERIALS AND METHODS

5.2.1 Chemicals and Reagents

Reagents for magnetic silica nanoparticles were purchased from Sigma Aldrich including Fe(NO3)3·9H2O, silicon tetraethoxide (TEOS), HCl, and NaOH. For drug-loading experiments, ropivacaine was graciously supplied by Venkat Mantha MD (University of Pittsburgh Medical Center). Filtration devices (Amicon Ultra-0.5 NMWL 3,000) for nanoparticle separation were purchased from EMD Millipore. Dialysis tubing (3.5 MWCO) was purchased from Fisher Scientific. A modulated power supply was purchased from Accel Instruments for the construction of an alternating magnetic field coil.

5.2.2 Synthesis of Mesoporous Silica Magnetic Nanoparticles

Preparation of mesoporous silica magnetic nanoparticles (sMNP) was carried out using the sol-gel process as described previously.[43] Briefly, a silica sol was prepared with silicon tetraethoxide (TEOS), 2 N HCl, and absolute ethanol in the ratio of 41.6 g/10 mL/12 mL at room temperature. The sol was stirred at r.t. for 2 hr open to the atmosphere in a round bottom flask equipped with a magnetic stirrer. Following the 2 hr aging process, $Fe(NO_3)_3 \cdot 9H_2O$ was dissolved in ethanol and added to the reaction in a ratio of Si/Fe = 1/1. To effectively load the model drug into the nanoparticles, the molecule of choice (ropivacaine/fluorescein) was added directly to the solution. To simultaneously hydrolyze the iron and deposit the silica, the pH of the solution was brought to pH ~ 2.7 with 1 N NaOH. However, care was taken to raise the pH slowly by adding in 100 µL NaOH every 2 min. to create uniform and reproducible sMNP. After the pH reached

2.7, the sol-gel was stirred for 24 hr. Experience demonstrated that repeated centrifugation and sonication resulted in aggregation, destruction, and pre-mature release of loaded drug from sMNP. To prevent these results, separation of sMNP from the reaction solution was achieved via dialysis. The acidic sol-gel suspension was transferred to SnakeSkin dialysis tubing (3.5 MWCO) and dialyzed in Millipore water. The water was changed repeatedly over the course of 24 – 48 hr until the pH of the water remained at pH ~ 7. The resulting sMNP water suspension was used as is for release experiments.

5.2.3 Characterization of Magnetic Nanoparticles

Morphology and uniformity of prepared sMNP were examined. The morphologies of the sMNP were examined under scanning electron microscopy (JEOL JSM-6510LV/LGS, SEM). Preparation of sMNP without aggregation was achieved by diluting nanoparticle suspensions 1:100 in water and dropping 10 – 20 μL droplets onto gold coated silicon wafers that were being heated on a hot plate. Size and uniformity of sMNP were measured using a dynamic light scattering spectrometer (Brookhaven 90+ quasi-elastic light scattering spectrometer).

5.2.4 Magnetic Coil Design and Stimulation

Drug-loaded magnetic nanoparticles were exposed to high-frequency magnetic field (HFMF) to examine the release properties following external magnetic stimulation. For construction of a custom coil, litz wire was wound around a dielectric permeability core to produce a coil with inductance ~ 1 mH and DC resistance equal to 0.5 Ω. Current signals were driven by a bench top frequency generator and amplified using a modulated power supply from

Accel Instruments (TS200-0A, -5 A to + 5A). To achieve high field strengths at the examined frequency range (50 kHz – 100 kHz), the resonant technique was used to create RLC circuits where the coil and a given capacitor were in resonance. Samples of sMNP in PBS were loaded into glass tubes and were exposed at a variety of field strengths, frequencies, and durations. Following stimulation, samples were removed and filtered using Amicon Ultra-0.5 filtration devices. The filtrate was examined for drug release by collecting the absorbance spectrum and identifying the respective peak for the model drug.

5.2.5 MRI Stimulation

A 7 tesla human MRI scanner was used to generate gradient fields used for MRI-triggered release from sMNP. Prior to *in vivo* experiments, MRI-triggered release was demonstrated by measuring release from sMNP inside custom constructed dialysis sample tubes. Using the constructed dialysis sample tubes, sMNP suspensions were exposed to gradient field stimulation. The field was realized by applying a designed Echo Planar Imaging sequence (EPI). The applied gradient fields were about 1.7 kHz and the field intensity is 16 mT/m. The samples were placed at a location 80 cm away from the imaging iso-center in order to generate a 12 mT gradient field.

For *in vivo* MRI-triggered, magnetic nanoparticles loaded with fluorescein (10 µL, 20 mg/mL) were injected 2 mm into the rat brain. The rat skull was placed 80 cm away from the imaging iso-center and were exposed to 10 min gradient field stimulation (EPI, 1.7 kHz, 12 mT). Following the MRI gradient field, a contralateral sMNP injection was used as a control for sMNP release. The animal was immediately sacrificed, the brain removed, and flash frozen (-80

°C). Tissue was prepared by cutting 30 µm thick sections and slices were imaged using bright field microcopy to observe sMNP and fluorescence microcopy to observe fluorescein release.

5.2.6 Preparation of Silica Magnetic Nanoparticle Coating

Magnetic nanoparticles for use in coating experiments where prepared as described above; however, with the exception that no drug was loaded into the particles. Surface treatment of silica magnetic nanoparticles was carried out as follows. Silica magnetic nanoparticles (20 mg/mL) in H_2O were diluted into 150 mL methanol. The solution was mixed with equal amounts of glycerol and sonicated for 30 min. After sonication, the nanoparticles were transferred to a round bottom flask and 10 mL of APTES was added to the reaction. The reaction flask was heated to 85 °C in an oil bath and a hot plate equipped with a temperature probe. After 3 hr, the functionalized nanoparticles were transferred to a dialysis tube and dialyzed for 3 days. The final nanoparticle suspension in H_2O was re-concentrated to 20 mg/mL via evaporation.

Meanwhile, silanized glass coverslips were prepared as described above (2.2.4). Following attachment of the heterobifunctional cross-linker, the functionalized glass samples were submerged in the suspension of surface treated sMNP (20 mg/mL). After, 1 hr the samples were rinsed with water and used for primary neuron culture experiments.

5.2.7 Primary Neuron Culture

The effect on neuron growth and proliferation from a sMNP coated surface was determined by plating primary neurons directly onto sMNP-coated glass samples. E18 Sprague-Dawley rat cortices were purchased from BrainBits, LLC. The rat cortices were triturated with a 1 mL

pipette and removed from the Hibernate MediaTM via centrifugation at 800g for 1 minute. Cells were re-suspended in Neurobasal (Fisher)/B27 (Gibco)/0.5 mM glutamine/25 µM glutamate (Sigma-Aldrich) culture medium and plated directly onto either glass or sMNP coated glass coverslips in 24-well cell culture plates (Corning Costar) at a density of 2.5 x 105 cells/cm2. Cells were grown in culture for 5 days at 37 °C in 5% CO2 and media was refreshed after day 3. Cells were fixed with 4% paraformaldehyde for 10 min. and were imaged under bright field microscopy to determine cell growth.

5.2.8 Release Measurements

Release of ropivacaine and fluorescein were quantified using a Spectromax M5 spectrophotometer. Following release, concentration of ropivacaine and fluorescein were determined by measuring the absorance ($\lambda \sim 230$ nm) or fluorescence ($\lambda_{ex/em} \sim 490/520$ nm), respectively. Concentrations were determined by creating a calibration curve from a dilution series. Averages of release solutions were compared using the Student's t-test (*p*-value > 0.05).

5.3 RESULTS AND DISCUSSION

5.3.1 Characterization of Synthesized Magnetic Nanoparticles

Mesoporous silica materials have grown in importance for new biomaterials given the combination of biocompatibility in addition to the capacity for drug loading and delivery.[57] By

combining the properties of silica nanomaterials with the capabilities of magnetic materials, we have engineered a system for controlled drug release (Figure 5-1).

Using the sol-gel process we were able to create silica magnetic nanoparticles encapsulating a drug of interest. To model drug-release we loaded the nanoparticles with two different molecules. Firstly, we loaded the nanoparticles with ropivacaine, a common anesthetic. While ropivacaine is an effective anesthetic, low concentrations enter the blood stream could be fatal. Therefore, controlled and targeted drug release are essential for proper administration. For MRI experiments we used the model drug fluorescein for *in vivo* visualization purposes.

By combining the base catalyzed hydrolysis of magnetic nanoparticles with the hydrolysis of tetraethyl orthosilicate, mesoporous silica magnetic nanoparticles could effectively be prepared in a single step.

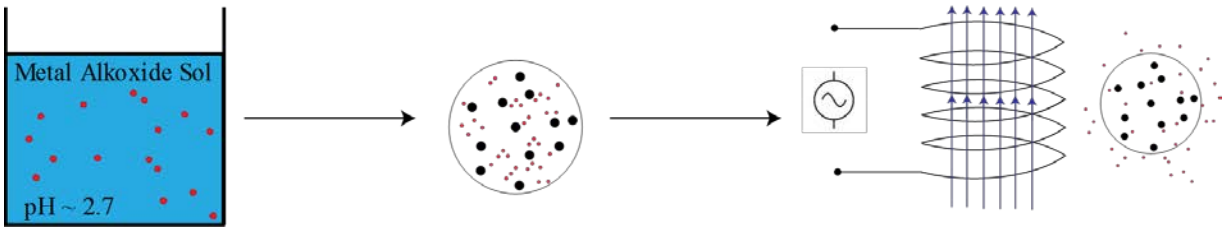

Figure 5-1 Design of Silica Magnetic Nanoparticle Drug Release Paradigm

Silica magnetic nanoparticles were prepared and loaded with model drug using the sol-gel process. Release of drug from the nanoparticles was monitored following exposure to high-frequency magnetic field stimulation.

Following preparation of sMNP, the nanoparticles retained the magnetic properties of typical iron oxide nanoparticles, demonstrating the capacity for magnetic separation (Figure 5-2). However, characterization of silica based nanomaterials can prove to be difficult. Without care,

sol-gel networks can easily form resulting in polymerized 'islands'.[58] In order to properly image nanoparticles under scanning electron microscopy, a combination of alcohol dehydration as well as fast-drying techniques were used. Nanoparticles imaged with these conditions demonstrated uniform spherical shape and 'nano' scale size (Figure 5-2).

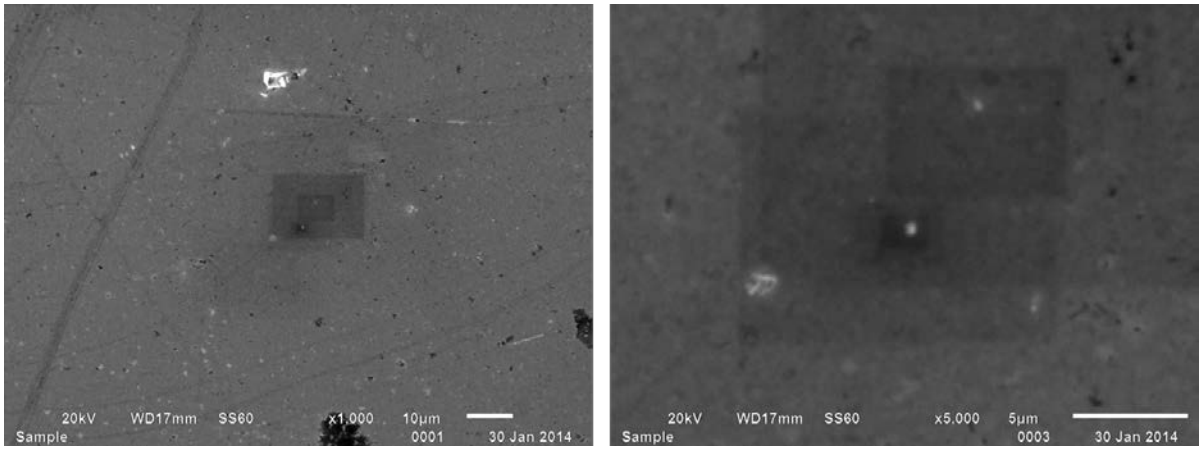

Figure 5-2 Scanning Electron Microscopy of Silica Magnetic Nanoparticles.

SEM images of prepared silica magnetic nanoparticles were collected using dilute samples to prevent aggregation. The observed nanoparticles were uniform in size and spherical in shape.

While SEM techniques allowed for a general observation of the size and morphology of the prepared nanoparticles, we relied upon the more quantitative nature of dynamic light scattering (DLS) particle size analysis for accurate representation of the uniformity of the nanoparticles. DLS results verify that prepared sMNP were of the 'nano' size roughly ~ 150 nm in diameter (Figure 5-3).

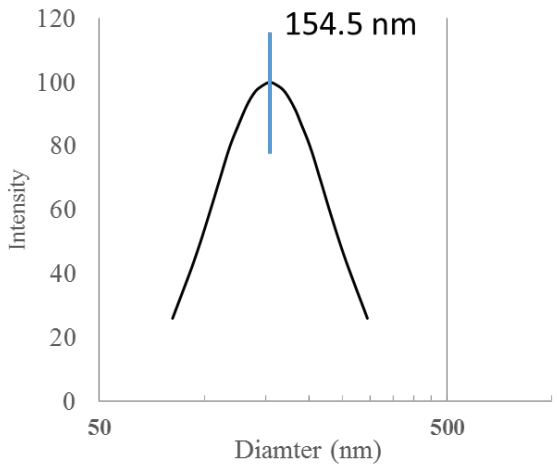

Figure 5-3 Size and Distribution of Drug Loaded Magnetic Nanoparticles.

Dynamic light scattering correlation spectroscopy using a NanoBrook 90Plus particle analyzer was used to determine the size and distribution of fluorescein loaded magnetic nanoparticles. The effective diameter of the synthesized nanoparticles was 154.5 nm with a polydisperisity index of 0.166.

5.3.2 Drug-Release Performance via Magnetic Stimulation

Loading drugs into silica magnetic nanoparticles creates a valuable technology for drug delivery that can be stimulated with a noninvasive magnetic stimulation paradigm. Prior to demonstrating the release of drugs from sMNP, the stability of the nanoparticles was evaluated. Nanoparticle suspensions were incubated at room temperature and physiological temperature for 24 hr. Following 24 hr, there was not a significant difference in the amount of passive ropivacaine released between samples at room temperature and samples incubated at physiological temperatures (Figure 5-4). Further experiments demonstrated that significant release could be stimulated by placing nanoparticle suspensions in 80 °C (data not shown).

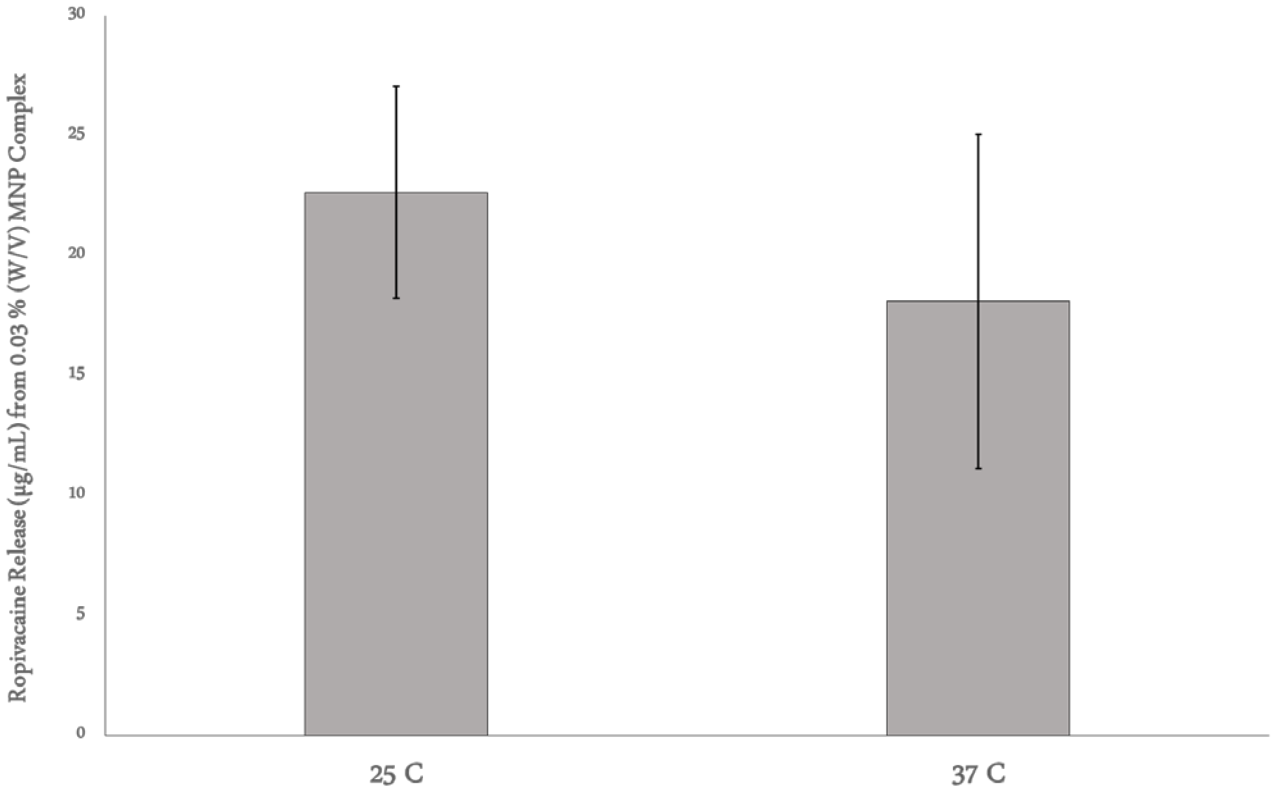

Figure 5-4 Temperature Stability of Ropivacaine Loaded Silica Magnetic Nanoparticles.

Passive ropivacaine release following synthesis was measured at both room and physiological temperature ($\lambda \sim 230$ nm; ± SEM; $n = 3$; * $p < 0.05$).

Once we had verified the stability of the nanoparticles, we tested the effect of high-frequency magnetic stimulation on the release properties of the sMNP. Using a 4G magnetic field created by a home-built coil driven by an amplified frequency generator, we observed significant increase in ropivacaine release almost instantaneously (Figure 5-5). The magnetic triggered drug release resulted in over a 100% increase in ropivacine when compared to the 24 hr passive release (room temperature). The increase between prolonged exposure to the high-frequency magnetic field (60 min) and shorter durations was not significant, suggesting that the majority of the contents of the nanoparticles were released from a short impulse.

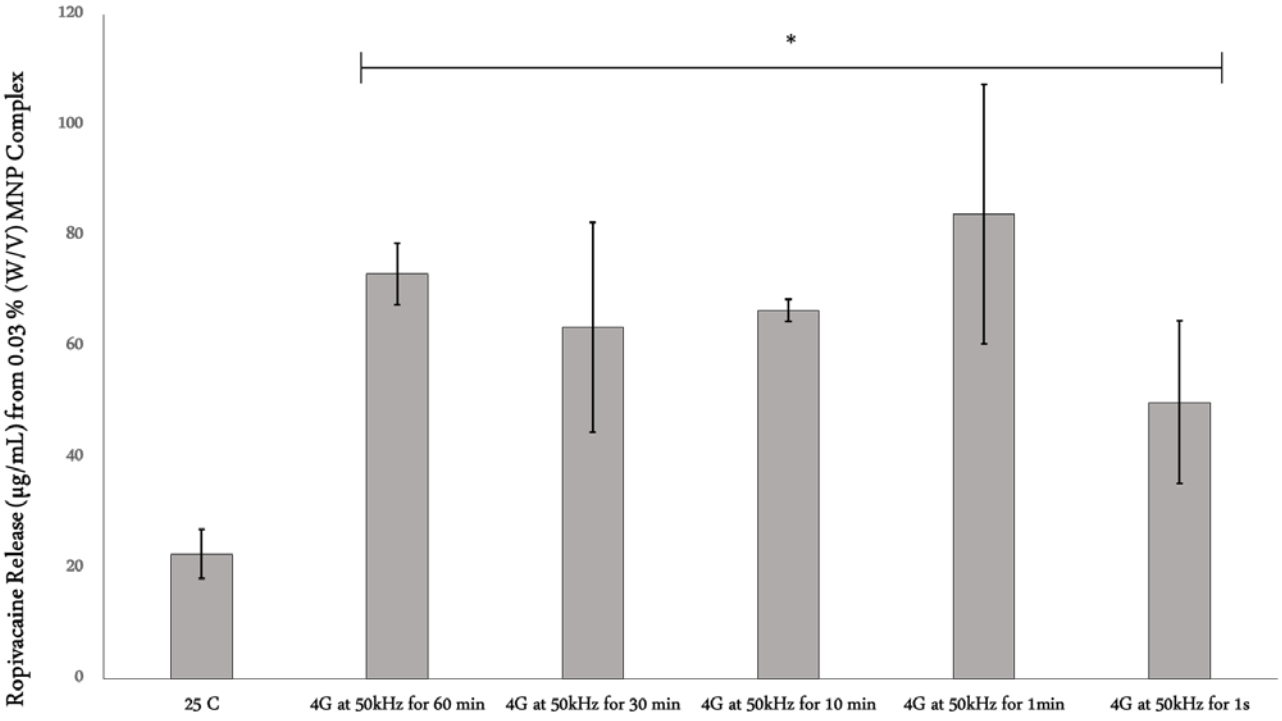

Figure 5-5 Time-Dependence of HFMF Triggered Drug Release.

MNP-Ropivacine complexes (0.03 % w/v) were exposed to RF magnetic fields (4G, 50 kHz) for varying durations (± SEM; $n = 3$). Release following 60 min, and 10 min, exposures is statistically significant from passive release (24 hr) ($p < 0.05$). Differences between exposure times are not statistically significant ($p > 0.05$) indicating only short-term exposure time necessary for ropivacaine release. Ropivacaine release was determined by measuring the peak absorbance of the released solution after filtering the nanoparticles through 100K MWCO filters ($\lambda = 230$ nm).

We also examined the importance of field strength on the release profile of magnetically triggered release from silica magnetic nanoparticles. At a field strength of 0.4 G, we observed no significant increase in drug release when compared to room temperature passive release (Figure 5-6). However, intermediate drug release was observed following stimulation with a 2G 50 kHz field suggesting a close to linear response at the field strengths tested. Further testing is

necessary to determine the full extent of the field strength vs. drug release profile. However, due to the constraints of our circuit setup, power supply, and coil, a field strength of 4 G was the highest we could test.

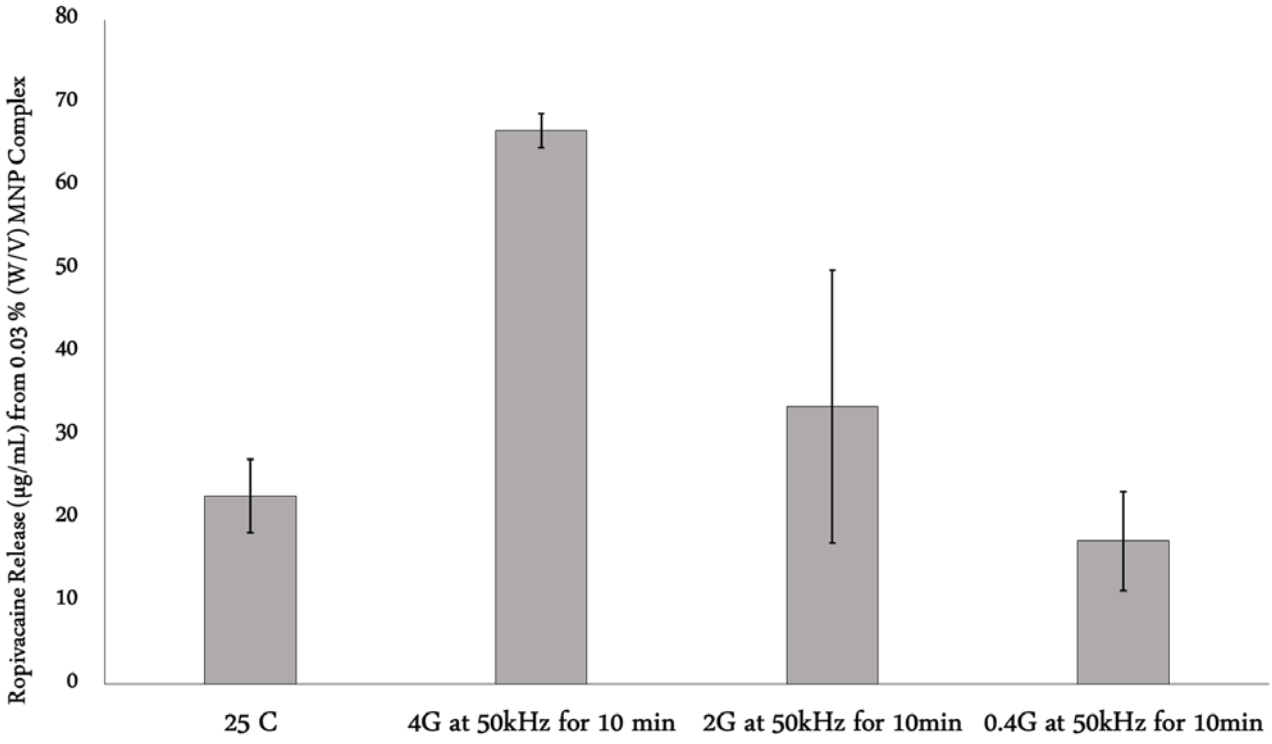

Figure 5-6 Field Intensity Dependence on HFMF Triggered Drug Release

MNP-Ropivacine complexes (0.03 % w/v) were exposed to RF magnetic fields for 10 min. (50 kHz) at varying magnetic field strengths (± SEM; $n = 3$). Only release following exposure to 4G field strength is statistically significant from passive release (24 hr) ($p < 0.05$). 4G triggered release is also statistically different than release triggered with 2G and 0.4 G field strengths ($p < 0.05$). Ropivacaine release was determined by measuring the peak absorbance of the released solution after filtering the nanoparticles through 100K MWCO filters ($\lambda = 230$ nm).

To examine the effects of frequency, we observed drug release under both high and low frequencies conditions. When looking at low frequencies, we compared a 1 kHz magnetic field to the standard 50 kHz field at 4 G. We found that low frequency stimulation was not capable of driving drug release from nanoparticles when the field strength was 4 G (Figure 5-7). Magnetic-triggered drug release is thought to be a result of local hyperthermia caused by the motion of the iron oxide cores inside the mesoporous silica matrix.[43] If the frequency of the magnetic stimulation is too low, then the required 'motion' of the iron oxide particles may not be great enough to cause swelling of the silica matrix and subsequent drug release.

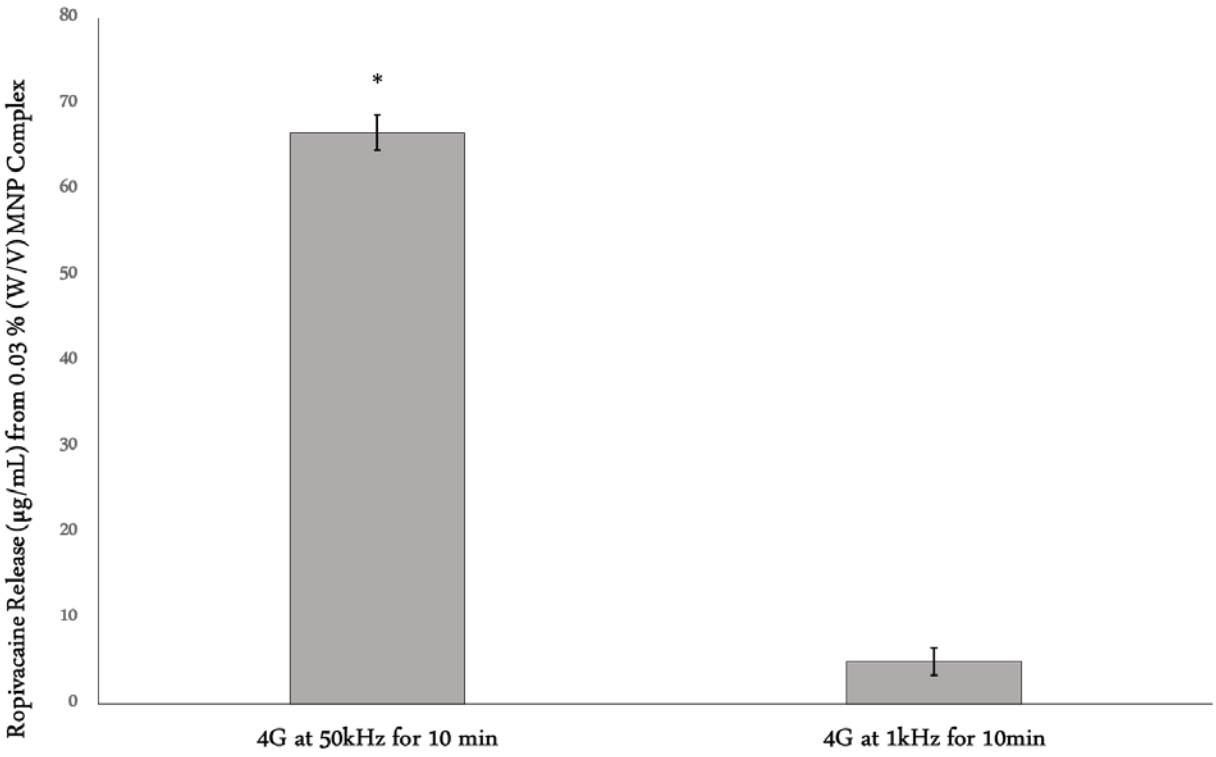

Figure 5-7 Low Frequency Dependence on HFMF Triggered Drug Release.

MNP-Ropivacine complexes (0.03 % w/v) were exposed to RF magnetic fields (10 min, 4G) at varying RF frequencies (± SEM; $n = 3$). Only release following exposure to 4G field strength is statistically significant from passive release (24 hr) ($p < 0.05$). Ropivacaine release was determined by measuring the peak absorbance of the released solution after filtering the nanoparticles through 100K MWCO filters ($\lambda = 230$ nm).

Likewise, we evaluated the impact that frequencies higher than 50 kHz had on the drug release from silica magnetic nanoparticles. However, due to the difficulties with driving high currents through inductors at high frequencies, we were unable to test 100 kHz at 4 G. Therefore, for the purposes of testing the 100 kHz frequency, we examined nanoparticle release at 50 kHz vs. 100 kHz at a field strength of 2 G (Figure 5-8). Unlike the trend we observed with low frequencies, there was no significant difference between higher frequencies. A possible source for this is most likely related to the relaxation time for the magnetic nanoparticles. The

commonly accepted hyperthermia mechanism requires agitation of the nanoparticles, increasing the local temperature, and resulting in drug release from the swelled nanoparticles. As the frequencies increase, at a certain point the nanoparticles can no longer 'move' in phase with the stimulation.[103] However, as we observed with the effect of field strength, the drug release properties of the nanoparticles are most certainly a function of both the field strength and frequency.

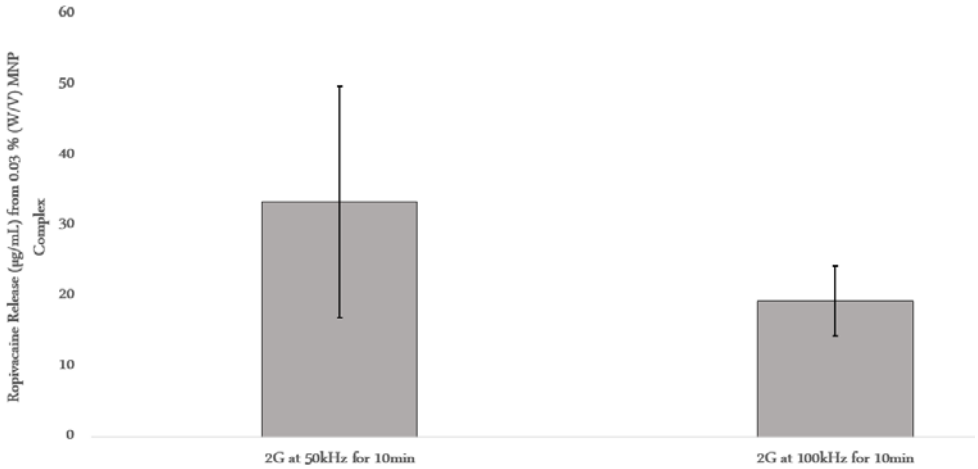

Figure 5-8 High Frequency Dependence on HFMF Triggered Drug Release

MNP-Ropivacine complexes (0.03 % w/v) were exposed to RF magnetic fields (10 min, 2G) at varying RF frequencies (± SEM; *n* = 3). Magnetic field-triggered release is statistically insignificant between 50 kHz and 100 kHz stimulation. Ropivacaine release was determined by measuring the peak absorbance of the released solution after filtering the nanoparticles through 100K MWCO filters (λ = 230 nm).

5.3.3 Drug Release following MRI stimulation *In Vivo*

A 7-Tesla human MRI scanner was used to test the ability of a clinical grade MRI to cause drug release of loaded nanoparticles *in vivo*. For the applied field, a gradient field was created using the designed Echo Planar Imaging sequence (Figure 5-9). Using the designed EPI, the maximum stimulation frequency that could be applied was 1.7 kHz. However, the gradient field intensity was 16 mT/m. Furthermore, inside the MRI scanner exists a permanent 7T static field.

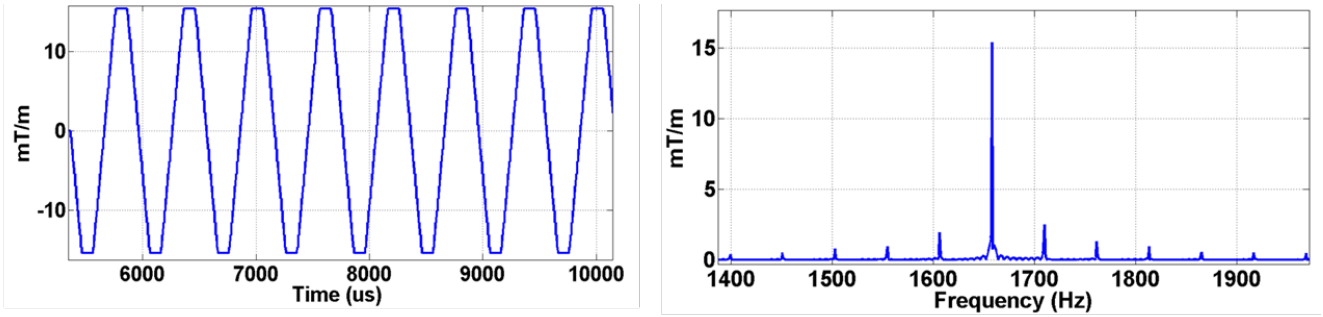

Figure 5-9 MRI Gradient Field Stimulation Paradigm

(A) Gradient field generated by MRI gradient coil when applying designed EPI sequence. (B) Fourier transform of the applied fields. The major frequency component is ~ 1.7 kHz and intensity is about 16 mT/m.

Given the high strength of the static field, 7T, a series of tests were conducted to verify that high field strengths alone would not cause drug release from nanoparticles. Nanoparticle (fluorescein loaded) suspensions were stored in various positions in the MRI scanner, and nearby rooms for 3 hr to determine the release properties. Static field (even at 7T) was not sufficient to cause release of fluorescein from nanoparticles (Figure 5-10).

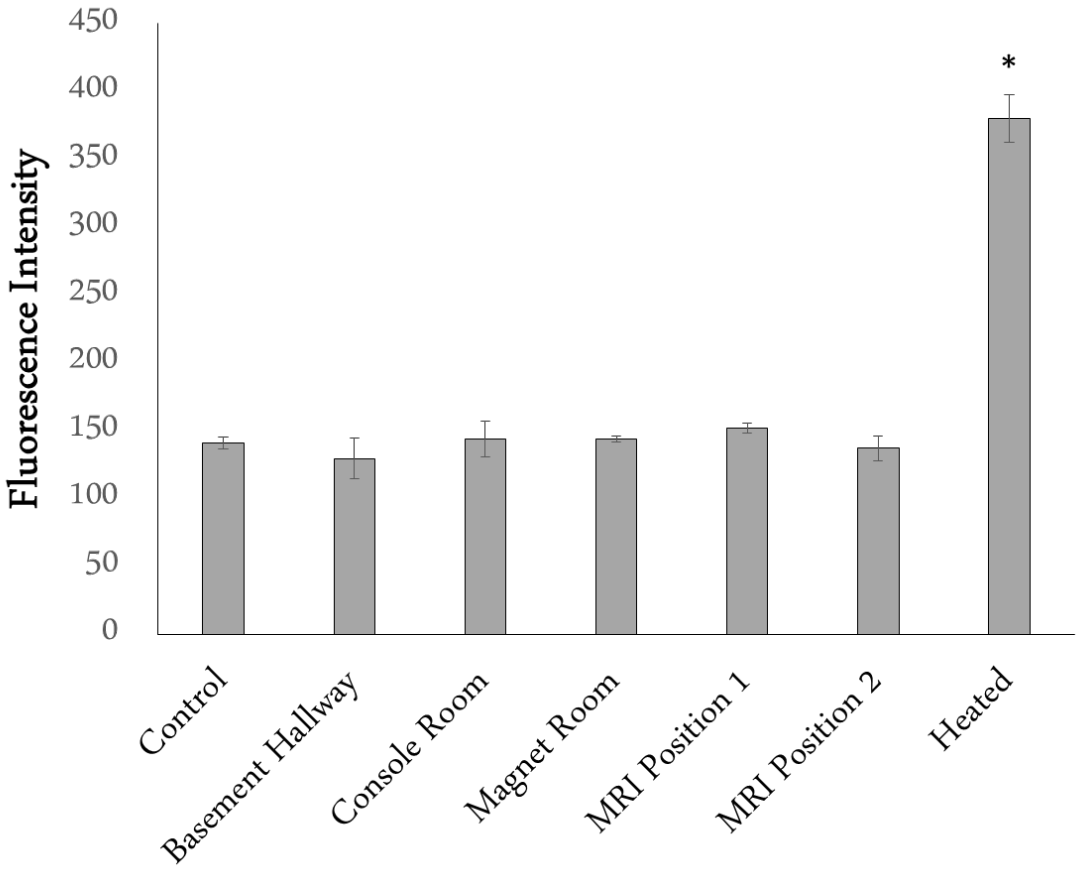

Figure 5-10 Static Field Effects on Silica Magnetic Nanoparticle Drug Release

MNP-FITC complexes were exposed to several different conditions for 1 hr. Afterwards the release of fluorescein was measured by first separating the nanoparticles via centrifugal filtration and then measuring fluorescence (λ_{ex} = 485 nm λ_{em} = 535 nm). MRI positions 1 and 2 were inside the MRI instrument at different positions (7T static field). Samples in the basement, console room, and magnet room were tested for the effect of remnant fringe fields. The heated sample (80 °C) was used as a positive control for FITC release.

Detection of fluorescein release from nanoparticles requires separation of the nanoparticles from the 'release solution' because nanoparticles scatter the light in the spectrophotometer detection equipment. Fluorescein loaded nanoparticles were placed into custom designed dialysis tubes for MRI release experiments (

Figure **5-11).**

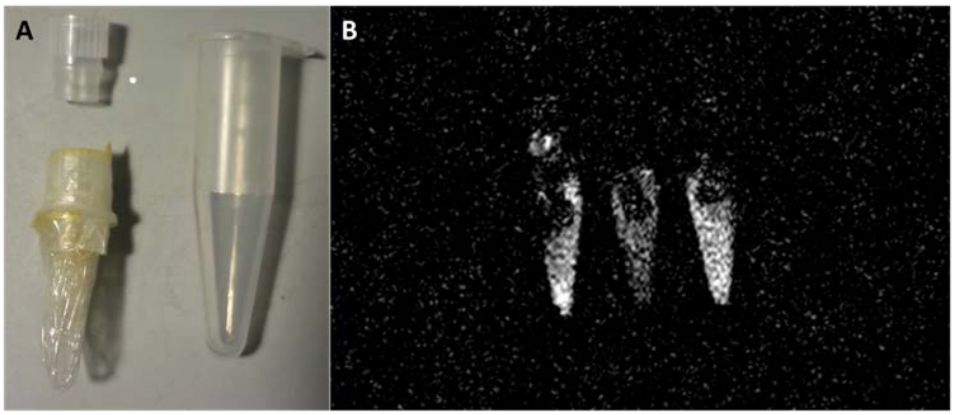

Figure 5-11 MRI Triggered Release *In situ* Design

MNP-FITC complexes were loaded into constructed dialysis sample tubes. (A) The dialysis tube allows for diffusion of released fluorescein following triggered release while preventing the light scattering nanoparticles from interfering in the fluorescence measurements. (B) Localizer images demonstrate the contrast agent properties of the Magnetic Nanoparticles as they appear black in the MRI scan.

Fluorescein loaded nanoparticles were placed into the dialysis tubes and placed into the MRI scanner. Fluorescence measurements of the dialyzed solution were measured every 10 min. to determine fluorescein release. After passive release had plateaued, MRI gradient field stimulations were applied to the samples, resulting in an increase in fluorescein solution (Figure 5-12).

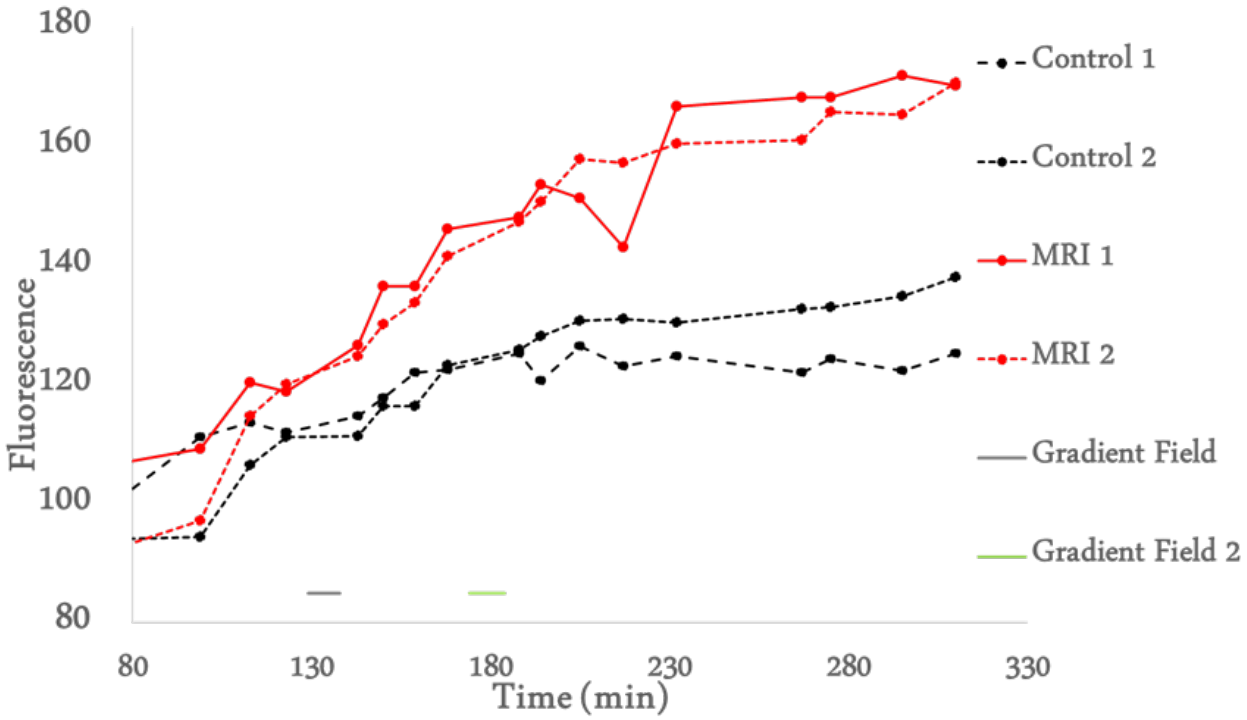

Figure 5-12 MRI Gradient Field Triggered Drug Release

Using the custom built dialysis sample tubes, fluorescein release was detected over time following MRI stimulation. Magnetic nanoparticles loaded with fluorescein were loaded into the samples tubes and passive release was allowed to occur until fluorescein diffusion plateaued (~ 80 min.). Afterwards we applied echo planar (EPI) sequence to apply a stimulation ~ 1.7 kHz, 8mT

Following our demonstration of the ability to trigger drug release from silica magnetic nanoparticles using a human MRI scanner, we moved on to a proof-of-concept study in the rodent brain. Magnetic nanoparticles were injected directly into the cortex of a *Sprague dawley*. The cortical region was then imaged using the MRI scanner (Figure 5-13). Once the region of interest was determined, the rat was exposed to the same gradient field used for the dialysis tube experiments. As a control, fluorescein loaded nanoparticles were also injected into a bilateral location immediately after the stimulation.

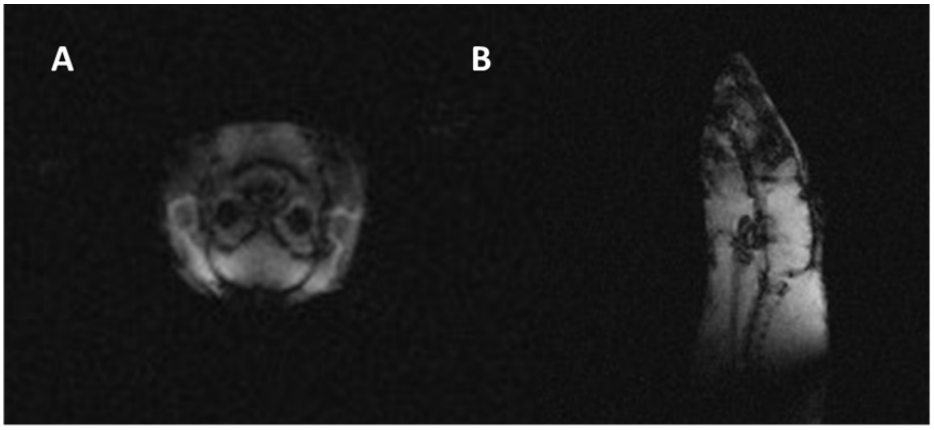

Figure 5-13 MRI Scan of Rodent Brain Target Site

Images of rat central nervous system before magnetic nanoparticle injection (A) axial, (B) sagital.

By sacrificing the animal and visualizing cortical slices with fluorescence microscopy, we were able to identify the nanoparticle injection site. Nanoparticles were easily identified by dark regions within the slice under bright field microscopy (Figure 5-14). In both cases (with or without gradient field stimulation), the nanoparticles were localized at the injection site and did not diffuse in the short time following the injection. Using fluorescence microscopy we observed a sharp contrast between nanoparticle sites with or without gradient field stimulation. Almost no visible fluorescein staining was observed in regions that were not exposed to MRI gradient fields. However, the nanoparticle injection site that was exposed to the 1.7 kHz EPI gradient field resulted in dramatic staining of the nearby tissue. Accumulation of the released fluorescein onto nearby cell bodies can easily be observed near the injection site.

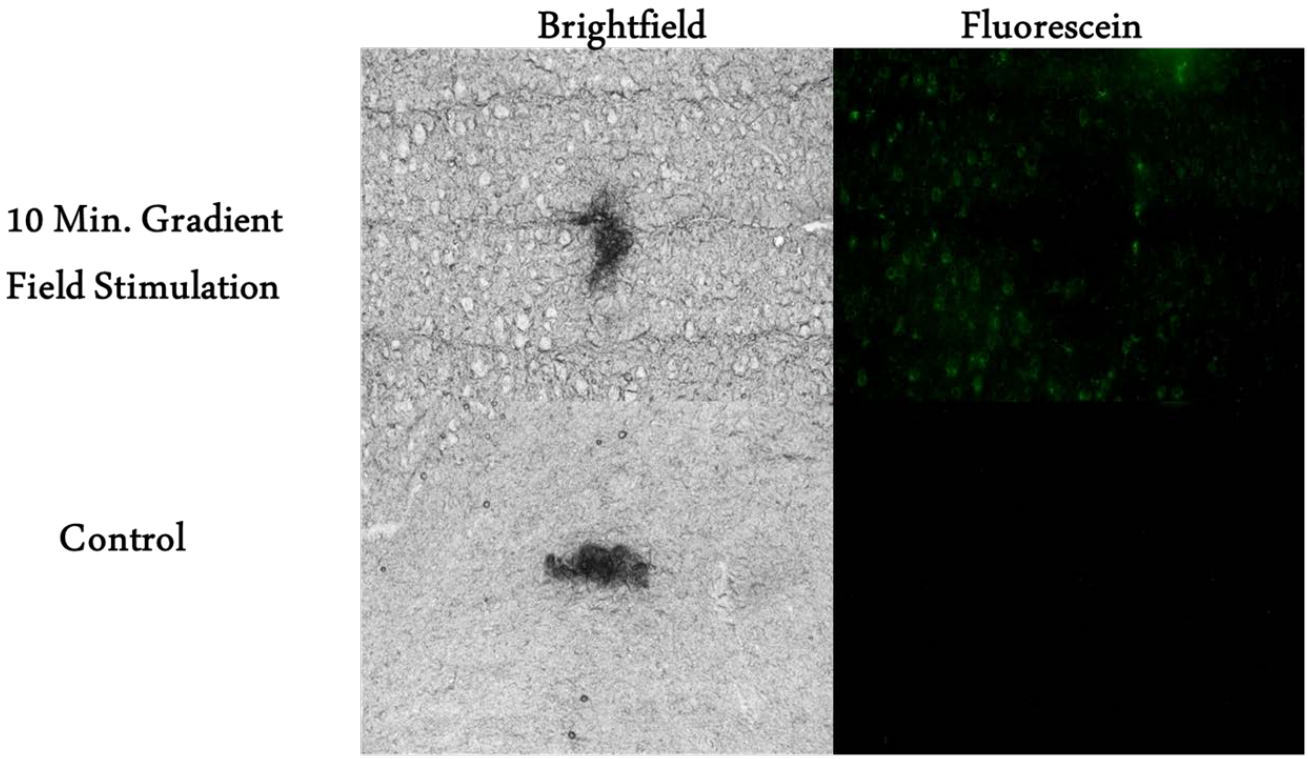

Figure 5-14 *In Vivo* Release of Fluorescein from MRI Triggered Silica Magnetic Nanoparticles

Magnetic nanoparticles (10 µL, 20 mg/mL) were injected ~ 2 mm into the rat brain and exposed to 10 min. gradient field stimulation (1.7 kHz, 8 mT) or injected directly afterwards to serve as a control (no stimulation). Following stimulation, the animal was immediately sacrificed, the brain removed and flash frozen (-80 °C). Sections were cut at 30 µm thick and slices were imaged using brightfield and fluorescence microscopy. Images depicted are at ~ 1300 µm deep and using 10X magnification. Magnetic nanoparticles appear as a dark mass in the brightfield. Using fluorescence microscopy there is a clear increase in fluorescence in tissue surrounding magnetic nanoparticles stimulated with the MRI gradient field.

5.3.4 Silica Magnetic Nanoparticle Coating

Drug delivery to the central nervous system poses many problems, including the ability to cross the blood-brain barrier. We have effectively demonstrated that silica magnetic nanoparticles have great promise for noninvasive controlled drug release; however, delivery to the CNS still remains a major hurdle. However, by anchoring silica magnetic nanoparticles to the surface of neural probes we could create a drug release device on the surface of the probe that could be controlled via an externally delivered magnetic field.

To create a silica magnetic nanoparticle coating, we first functionalized prepared nanoparticles with reactive functional groups. Silanol groups on the surface of magnetic nanoparticles can react in similar ways to an activated glass substrate.[104, 105] Using the organosilane, APTES, we modified the nanoparticles with the $–NH_2$ functional group (Figure 5-15).

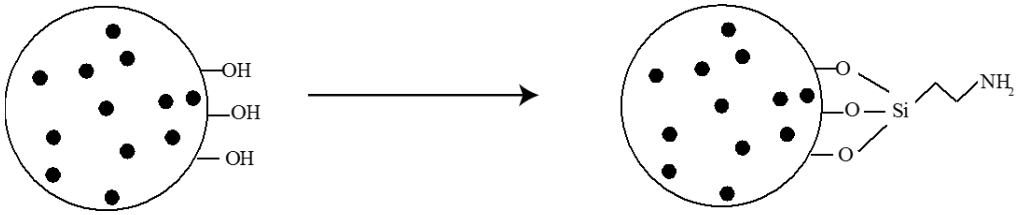

Figure 5-15 Silica Magnetic Nanoparticle Functionalization Scheme

Functionalization of silica magnetic nanoparticles was completed using the organosilane linker, 3-aminopropyltriethoxysilane (APTES).

By functionalizing the nanoparticles with an amine group, we were able to use the coupling agent, GMBS, to couple the nanoparticles to a silanized surface. To that end we again used silane chemistry to functionalize the surface of glass. Once again the organosilane linker created a free amine group on the surface of our glass samples. The silane-functionalized glass samples were then reacted with the activated nanoparticles to couple the silica magnetic nanoparticles onto the surface of the glass (Figure 5-16).

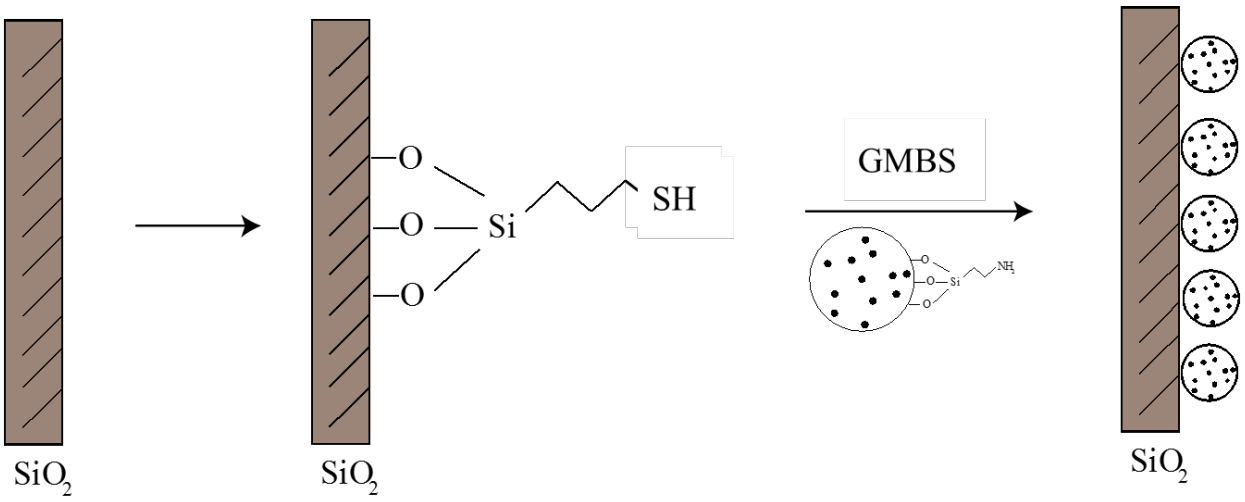

Figure 5-16 Silanization Scheme for Functionalized Silica Magnetic Nanoparticles.

Preparation of silica magnetic nanoparticle coating was achieved via a dual-silane strategy. Silicon surfaces were treated with a thiol-containing organosilane and coupled to silanized nanoparticles using *N*-ɣ-maleimidobutyryloxy succinimide ester (GMBS).

To determine the uniformity of the coating we examined the samples under scanning electron microscopy. Under SEM we observed that the nanoparticles were in fact coupled to the surface. The nanoparticles were also less prone to typical 'island' formations as seen when

drying free silica nanoparticles. However, uniform coverage of the nanoparticles were only observed at regions near the edge of the sample, suggesting elevated concentrations would be necessary for fully uniform samples (Figure 5-17). Interestingly, ‘cross’ shaped aggregations of the nanoparticles were observed that are not seen when drying nanoparticles directly onto glass samples. It is likely that these substrates may in fact be cross-linked nanoparticles when you consider the cross-reactivity for activated silica nanoparticles with amine-functionalized nanoparticles. The unique ‘cross’ shape could be a result of the magnetic moment of the nanoparticles that influences the overall gross morphology of the nanoparticle structures.

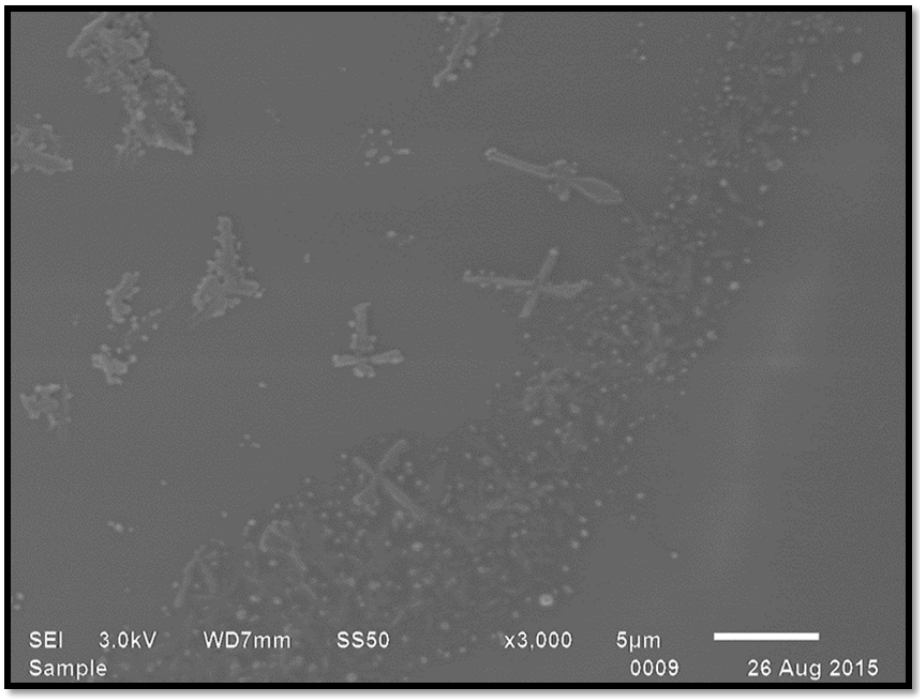

Figure 5-17 Scanning Electron Microscopy of Silica Magnetic Nanoparticle Self-Assembled Monolayer.

SEM Images of the silica magnetic nanoparticle surface show sub-micron nanoparticles coated onto the surface of the glass samples. A region of uniform coverage is observed at edges of the sample. Macro-structures are observed throughout the sample where magnetic nanoparticles collect into ‘cross’-like shapes.

To determine the biocompatibility of the silica magnetic nanoparticle coating, we plated primary neuron cultures directly onto samples coated with the nanoparticles. Not only did neurons readily grow onto surfaces coated with the sMNP, but neurite extension rivaled what we observe with L1CAM coatings (Figure 5-18). The magnetic field of a neuron is a well-known phenomenon and the basis for such technologies as trans-cranial magnetic stimulation. In addition the relationship between magnetic fields of nearby neurons is thought to be important for development and is being manipulated for new nerve guide technologies. [52, 106] With this understanding, the magnetic nature of the coating may in fact be responsible for the neurite proliferation we observe in culture.

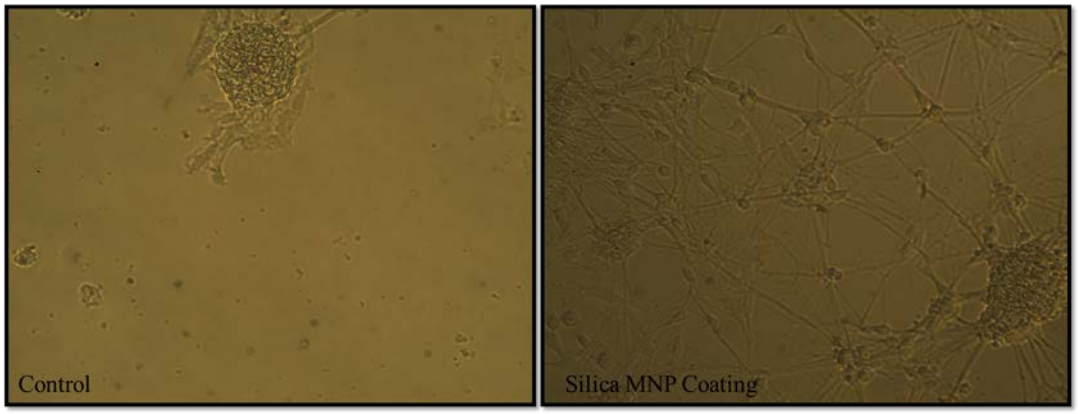

Figure 5-18 Primary Neuron Proliferation on sMNP Coating.

Primary neuron cultures were grown on the silica magnetic nanoparticle coating. Neurite growth and cell adhesion is observed in samples with the coating.

5.4 CONCLUSIONS

To establish a new method for drug-delivery into the central nervous system, we have optimized the stimulation and release properties of silica magnetic nanoparticles. By combining the biocompatible properties of silica materials with the magnetic separation and controlled-release properties of magnetic nanoparticles, we have demonstrated a noninvasive method for controlled drug-release. In addition, we have adapted the technology for use with clinical grade MRI instrumentation and provided a 'proof-of-concept' for *in vivo* drug release into the CNS using a 7-Tesla MRI scanner. Furthermore, for the purposes of improving the interface between neural tissue and implanted probes, we were able to anchor sMNP directly to the surface of silicon samples. Not only did our dual-silane method enable incorporation of sMNP into self-assembled monolayers, but we observed a remarkable improvement in neuron attachment and proliferation. Combined with the noninvasive drug-release techniques described, we have demonstrated the potential of sMNP for drug-delivery into the CNS in order to treat the inflammatory response nearby neural electrodes.

6.0 CONDUCTIVE POLYMER-MAGNETIC NANOPARTICLE NANOCOMPOSITE FOR IMPROVED ELECTROCHEMICAL DRUG-RELEASE

6.1 INTRODUCTION

New methods for controlled drug release are of great importance to the medical field, particularly for neural technologies considering the difficulty in targeted drug release into the central nervous system (CNS).[107-110] Neural prosthetic technologies represent a unique circumstance where an electrically active device is implanted into the tissue. While the inflammatory response to such devices poses a problem to the development of a stable interface between host tissue and an inorganic material, the individual electrodes create potential sites for externally controlled drug release.[61, 111]

Drug release from electrodes has increased in importance with the development of new conducting polymer nanomaterials. In addition to improved recording performance gained by deposition of conducting polymer films onto electrodes, these polymers enable drug-loading and subsequent drug-release into nearby tissue. Typically drugs loaded into the polymer, as dopants, are released by electrically stimulating the electrode and thereby 'ejecting' the drug into the surrounding area. However, the quantity of drug loaded is often restricted by the surface are of the material.

Recently materials combining both conducting and magnetic properties have gained the interest of scientists in fields ranging from electronics to optics.[55] Nanomaterials with this dual-functionality result in new methods of manipulation previously unexplored. However, combining the two materials for the purpose of drug-delivery has yet to be investigated. In this work we have prepared nanoparticles with both conductive and magnetic properties for the purpose of improving the drug-loading and release properties of electrodeposited nanofilms.

6.2 MATERIALS AND METHODS

6.2.1 Chemicals and Reagents

For preparation of conductive-magnetic nanoparticles, ferrous sulfate, polyethylene glycol (PEG, M_n = 4000 g mol^{-1}), $FeCl_3 \cdot 6H_2O$, NaOH, H_2SO_4, HCl (37%), H_2O_2, polyviynyl alcohol (PVA), and pyrrole monomer were purchased from Sigma Aldrich. The pyrrole monomer was purified via vacuum distillation and stored frozen in a low-temperature desiccator.

6.2.2 Synthesis of Conductive Magnetic Nanoparticles

Fe_3O_4 magnetic nanoparticles were prepared using the following precipitation-oxidation method described previously.[55] In a 3-neck round bottom flask, equipped with a condenser, magnetic stir bar, and nitrogen inlet, 70.0 g of PEG (M_w = 4000 g mol^{-1}) was added to 3.0 g $FeSO_4 \cdot 7H_2O$ in 140 mL H_2O. The reaction was bubbled in N_2 for 30 min and 0.6 mL of H_2O_2 (37%) was added. The temperature was increased to 50 °C and the PH increased to ~ pH 13 using 3M NaOH. After

24 hr, the magnetic fluid was dialyzed with SnakeSkin dialysis tubing (3.5 MWCO) in Millipore water for 48 hr. Afterwards, the magnetic nanoparticles were separated via magnetic field separation, repeatedly washed with Millipore water, and dried under vacuum.

Incorporation of the Fe_3O_4 magnetic nanoparticles into Fe_3O_4-PPy nanoparticles was accomplished by chemical polymerization of polypyrrole around the previously synthesized magnetic nanoparticles. The *in situ* emulsion polymerization was carried out in a three-neck round bottom flask, equipped with a magnetic stir bar, nitrogen inlet, and condenser. Sodium *p*-dodecylbenzenesulfnate (NaDS, 1.5 g) was dissolved in 90 mL H_2O in the round bottom flask and stirred for 15 min followed by the addition of 500 mg Fe_3O_4 and 500 mg fluorescein. After an additional 15 min, 5 mL of pyrrole as added to the reaction and stirred for 1 hr. In a separate flask, $FeCl_3$ was dissolved in water containing 12 mg/mL poly(vinyl) alcohol (PVA, M_w 13000-23000) with an oxidant: monomer molar ratio of 0.5. The oxidant solution was then added dropwise to the reaction while on ice. The polymerization continued for 12 hr at 0-5 °C. The fluorescein loaded Fe_3O_4-PPy nanoparticles were dialyzed with Millipore water for 2 days and purified via magnetic separation.

6.2.3 Preparation of Conductive Magnetic Nanoparticle Electrode

The fluorescein loaded Fe_3O_4-PPy nanoparticles were electrochemically deposited onto gold coated silicon wafers with a chromium adhesion layer. The polymerization solution consisted of fluorescein loaded Fe_3O_4-PPy and an additional 0.5 M pyrrole monomer. For control samples, 0.1 M fluorescein was added to the deposition solution. Polymerization occurred using a Gamry potentiostat, FAS3 femtostat (Gamry Instruments) using the traditional three-electrode system. The gold coated silicon wafer served as the working electrode in addition to a silver/silver

chloride reference electrode (CH instruments) and a platinum foil counter electrode. Prior to deposition, a static neodymium magnet was placed behind the electrochemical cell to locate the nanoparticles to the electrode surface. After approximately 2 min a visible change in the solution could be observed with the dark Fe_3O_4-PPy nanoparticles aggregated around the working electrode. Polymerization was conducted at 0.8 V for 200s. Samples were soaked in PBS for 30 min then rinsed in deionized water and allowed to air dry prior to release.

6.2.4 Electrochemical Release

Electrochemical release was conducted into fresh PBS. Fluorescein release from fluorescein loaded Fe_3O_4-PPy was stimulated by using a repeating negative potential. Each stimulation consisted of five repeats of a -1 V for 5 s interval followed by a 0 V for 5 s interval. Following release, samples were collected and fluorescence was immediately quantified on a Spectromax M5 spectrophotometer. Following release fluorescein in the solution was quantified by measuring the fluorescence (λex/em ~ 490/520 nm). Averages of release solutions were compared using the Student's t-test (p-value > 0.05).

6.3 RESULTS AND DISCUSSION

6.3.1 Preparation of Conductive Magnetic Nanoparticles

Materials with both conductive and magnetic properties are extremely useful; however, little work has been done on the drug-release capabilities of such materials. We combined previously used methodology to create magnetic nanoparticles entrapped along with the model drug, fluorescein, in a larger polypyrrole conducting polymer nanoparticle (Figure 6-1).

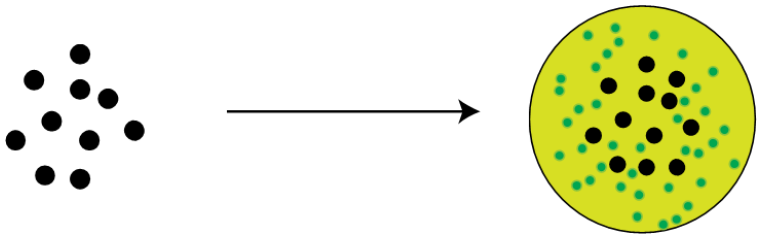

Figure 6-1 Synthesis Scheme for Magnetic-Conductive Nanoparticles

Once we synthesized the particles, we verified size and morphology using scanning electron microscopy. The particles were roughly 200 nm in diameter and fairly uniform in size distribution (Figure 6-2). The nanoparticles demonstrated excellent magnetic separation properties while suspended in water. The incorporation of PVA was necessary for preparing suspendable nanoparticle preparations. Previous efforts to prepare conductive-magnetic nanoparticles without PVA resulted in insoluble particles that were unable to be dispersed in aqueous conditions.

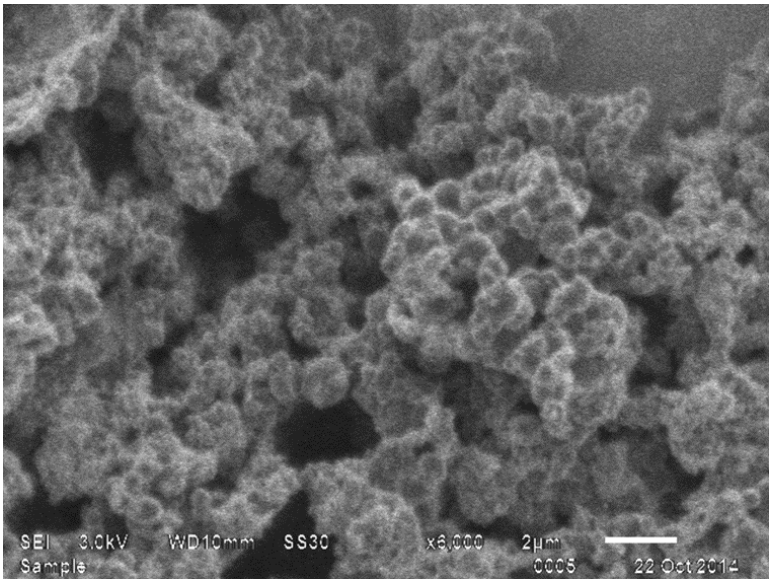

Figure 6-2 SEM of Prepared Magnetic-Conductive Nanoparticles.

SEM images of the magnetic-conductive nanoparticles demonstrate spherical shape of prepared particles.

6.3.2 Preparation and Release Performance for Conductive MNP Electrode Film

Using the prepared conductive-magnetic nanoparticles we designed a release paradigm that is traditionally used to release drug from conducting polymer nanocomposites (Figure 6-3).[61, 111] However, because of the unique magnetic properties of the nanoparticles we were able to use magnetic separation techniques to increase the concentration of the nanoparticles at the surface of the electrode. By placing a neodymium magnet behind the working electrode during electrodeposition, a thick black coating was created. Additional pyrrole monomer was added to the deposition solution to increase adhesion of the coating.

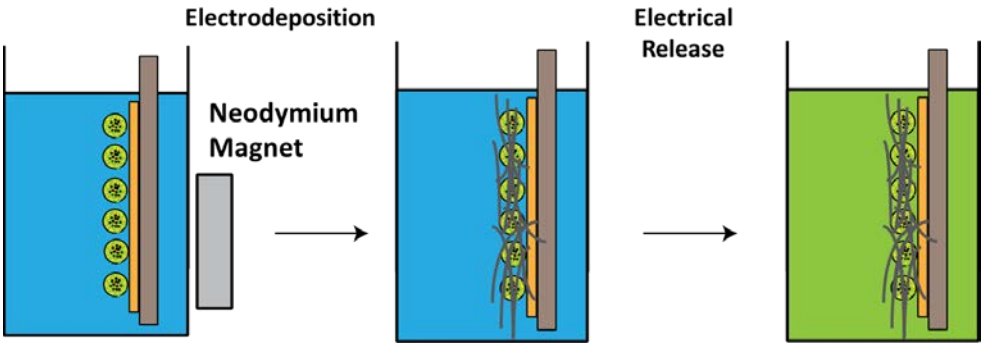

Figure 6-3 Electrodeposition of Magnetic-Conductive Nanoparticle.

Electrodeposition was carried out using a two-step process. First nanoparticles were aggregated at the electrode surface using a neodymium magnet placed behind the electrode. Afterwards, electrodeposition was completed to polymerize polypyrrole. Electrical stimulation was used to trigger drug release from the prepared films.

After deposition of the coating we examined both the PPy control and PPy/Fe_3O_4 films with scanning electron microscopy. As expected, the control film was smooth and evenly coated the morphology of the working electrode. The conductive-magnetic film was much different in morphology, characterized by rough, 'birds-nest' like structures covering the surface of the electrode (Figure 6-4).

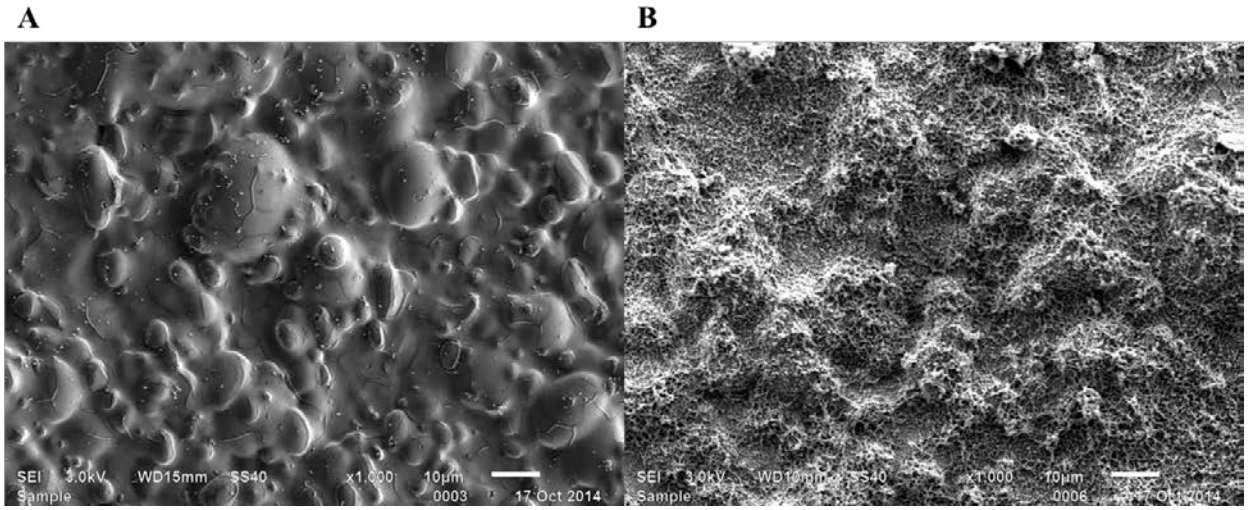

Figure 6-4 Scanning Electron Microscopy of Magnetic-Conductive Nanocomposite Film.

SEM images illustrate the differences between nanocomposite films with or without magnetic-conductive nanoparticles. Polypyrrole films polymerized with fluorescein are smooth and coat the contours of the electrode surface (a). Polymerization in the presence of magnetic-conductive nanoparticles results in a rough, dense network (b).

For electrochemically controlled drug release from the prepared films, electrodes were submerged into electrochemical cells containing fresh PBS. Electrodes were washed beforehand with copious amounts of PBS to wash away any loosely bound fluorescein/monomer. By exposing the cell to UV light we were able to visualize the release from the macro-electrodes (Figure 6-5). Release from the PPy/Fe_3O_4 film resulted in a bright green color change to the probe as well as the nearby solution (Figure 6-5). This change was not visible by eye in the control condition and demonstrated the dramatic increase in fluorescein release from the PPy/Fe_3O_4 film.

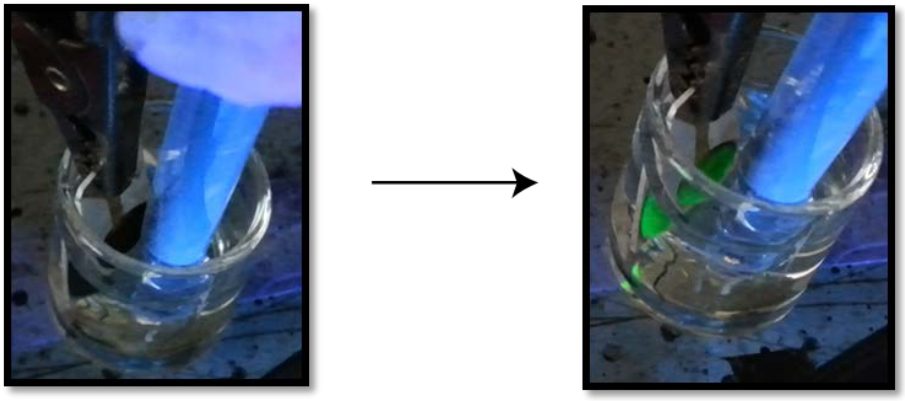

Figure 6-5 Electrochemical Release from Magnetic-Conductive Nanocomposite Film.

Electrochemical release from magnetic-conductive nanocomposite results in immediate fluorescein release that can be visualized with a handheld UV lamp.

We were able to quantify the fluorescein release to compare the control and PPy/Fe_3O_4 films using fluorescence measurements of the release solution. Following electrochemical stimulation, we measured the fluorescein released and found that the PPy/Fe_3O_4 resulted in an increase of over 500% (Figure 6-6). This dramatic increase in fluorescein release is not surprising considering the extreme differences observed in the film morphologies of the two tested coatings.

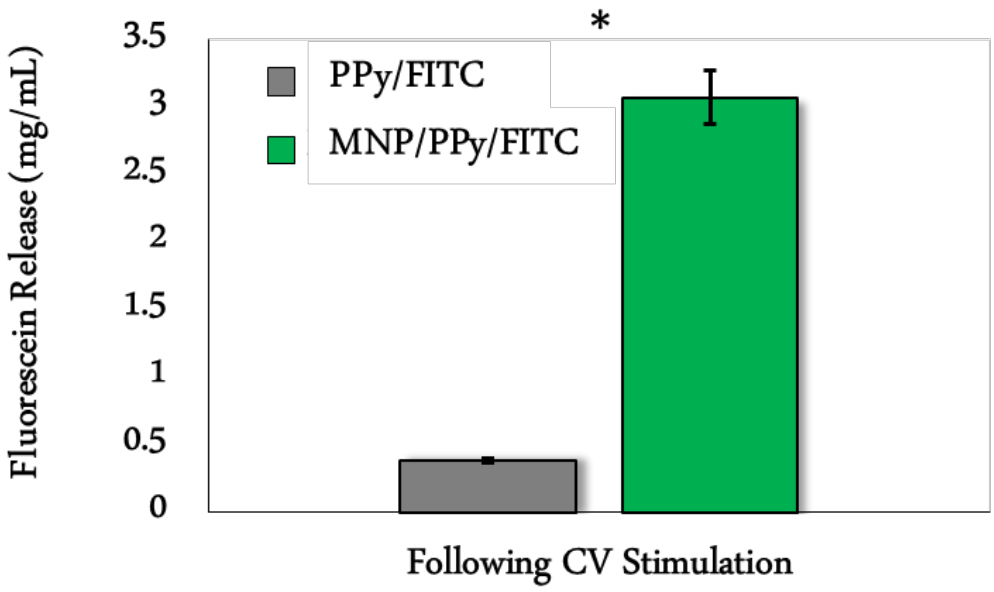

Figure 6-6 Quantitative Fluorescein Release from Magnetic-Conductive Nanocomposites

Fluorescein concentration ($\lambda_{ex/em}$ ~ 490/520 nm) was measured following electrical stimulation of fluorescein-doped polypyrrole films (PPy/FITC) and the magnetic-conductive nanocomposite film (MNP/PPy/FITC). Release from the magnetic-conductive film was significantly higher than traditional PPy/FITC films (± SEM; $n = 3$; * $p < 0.05$).

6.4 CONCLUSIONS

To improve the drug-loading and release of electroactive conducting polymer films we have developed a new conductive-magnetic nanocomposite. By loading a conductive-magnetic nanoparticle with drug, we are able to create a densely loaded electroactive drug reservoir. Using the magnetic separation properties of the synthesized nanocarrriers, we were able to electrodeposit an extensive conducting polymer network on an electrode encapsulating the loaded nanoparticles. We have demonstrated that the prepared nanocomposite is capable of electroactive drug-release and outperforms the traditional doped-conducting polymer in storage by several folds.

7.0 CONCLUSION

7.1 SUMMARY OF RESULTS

This dissertation describes the development of new materials for the improvement of the neural electrode-tissue interface. Using fundamental theory and techniques from chemistry, molecular biology, and physics a wide variety of new platforms were developed. A new immobilizable SODm (iSODm) was prepared and demonstrated effective improvement of neuron survivability and reduction of oxidative environment. As a means for detecting oxidative stress *in vivo*, a new superoxide sensor was developed by combining a metalloporphyrin sensing element with the electrical properties of PEDOT/GO films. With the goal of translating the L1CAM biomimetic coating technology that has demonstrated the ability to promote neuron survival as well as prevent inflammation, efforts were placed on creating translatable technological improvements. Finally, using magnetic and conductive nanomaterials, new drug delivery systems were developed with clinical applications.

The antioxidant SODm coating described in *Chapter 2* was prepared with the hope of reducing oxidative stress around neural implants and therby improving neuron survivability. Not only was a new complex synthesized with high SODm activity, but it was combined with SAM technology to create an antioxidant surface coating. Using the iSODm coating, we demonstrated an elimination of superoxide produced by a stimulated microglia cell line. We also observed

evidence of a decreased inflammatory response as indicated by a decrease in ROS related enzyme activity. Initial acute (1 week) *in vivo* studies demonstrated the effectiveness of the coating to improve neuron density around implanted neural electrode probes.

Whereas *Chapter 2* focused on the creation of a new method for preventing oxidative damage, the focus of *Chapter 3* was to produce a new diagnostic tool for *in vivo* oxidative stress. Building upon our laboratories previous success with PEDOT/GO based biosensors, we incorporated a superoxide sensing element into the film. With the prepared hemin-PEDOT/GO electrode we were able to effectively detect superoxide produced via the xanthine oxidase enzymatic system. In addition using this newly designed electrode, we were able to complete a mechanistic study of superoxide production.

Chapter 4 expanded upon our previous work developing biomimetic coatings for neural implants. We were able to apply our knowledge of protein-based coatings to create a new coating strategy for parylene C based devices. In addition, for the first time we demonstrated isolation of non-human primate L1CAM for use in *in vivo* studies. Furthermore, we developed new practical coating strategies for applying the L1CAM technology to FDA-approved devices. Finally, using our translatable technology, we effectively demonstrated improvements in neural recording quality in non-human primate neural prosthetic experiments.

To expand upon our ability for treatment of oxidative stress near neural implants *Chapter 5* details the development of new methods of non-invasively controlling drug release. Using a combination of silica and magnetic nanomaterials, we prepared nanoparticles that were responsive too externally applied magnetic fields. After demonstrating these materials could release loaded drug molecules following high-frequency magnetic field, we evaluated their performance *in vivo*. Using clinical grade instrumentation, we provided a ‘proof-of-concept’

study indicating that these materials could be used to drive drug release in the brain tissue of living organisms. Finally to provide a platform for combining this technology with neural electrodes, we were able to prepare a magnetic nanocomposite coating on silicon based substrates. Surprisingly we demonstrated not only improved biocompatibility but a remarkable effect on improving neurite outgrowth.

Finally, *Chapter 6* describes an additional method for drug delivery into the central nervous system from implanted electrode technology. Combining our previous efforts of electrochemically controlled drug-release, with our emerging research in magnetic nanoparticles, we effectively created a new conductive-magnetic nanocomposite. Using magnetic separation and electrodeposition we prepared a new electrode film marked by a dramatic increase in surface area, roughness, and fibrous network. This coating demonstrated a remarkable improvement in terms of drug loading and release capabilities compared to traditional conducting polymer based designs.

7.2 FUTURE DIRECTIONS AND PRELIMINARY DATA

7.2.1 Functional Study of iSODm Electrode

In this work we have described the beneficial effects of the iSODm coating resulted in antioxidant properties demonstrated *in vitro* as well an improved neuron density around neural electrodes implanted *in vivo* for 1 week. Due to these promising results, the technology is currently being tested with functional arrays. However, prior to use with functional neural probe packages, the practical design and chemical strategy had to be altered. For the purposes of

silanization of the neural probe in a moisture-free environment, a 3-neck flask was used that was equipped with a probe holder device (Figure 7-1). Furthermore, the traditional solvent used for organosilane chemistry, toluene, was incompatible with neural probe technology. We found that toluene vapors inevitably destroyed the epoxy coating covering the probe leads. We also evaluated a different method for the cleaning and activation of the silicon surface. For the safety of the probe, nitric acid cleaning was avoided. Instead, the probe was rinsed with acetone, followed by a 50% (v/v) MeOH/H_2O solution. To remove organic debris, the probe was rinsed with chloroform. Finally, the array was exposed to O_2 plasma for 1 min. To test the effectiveness of this coating strategy, we demonstrated that an L1CAM coating prepared in this manner effectively promoted neuron attachment (data not shown).

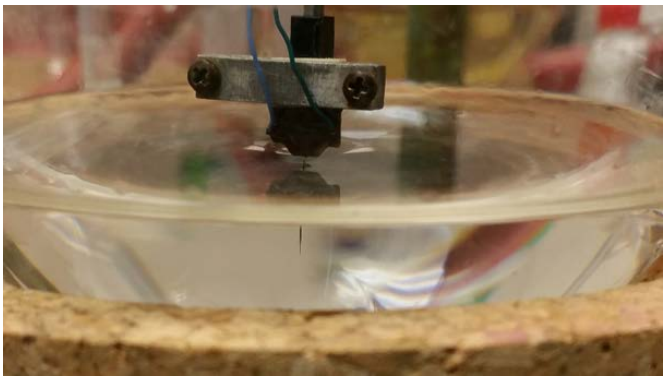

Figure 7-1 Design of Functional Array Coating Setup

To test the performance of chronically implanted neural probes, coated and unmodified probes were implanted into *S. dawley* rats for a functional recording study. Functional Michigan-style Neuronexus probes (A1-LP style, 16 channels, 3 mm long, 100 µm site spacing, 703 μm^2 area) were implanted into the M1 of rat brain (1.5 mm anterior to Bregma, 2 mm lateral to the midline). Neural recording was completed using a TDT RX5 system. Recordings were done on awake, freely moving animals. Data was collected in 5 min blocks and spike data analyzed using the commercially available OpenSorter package (Figure 7-2).

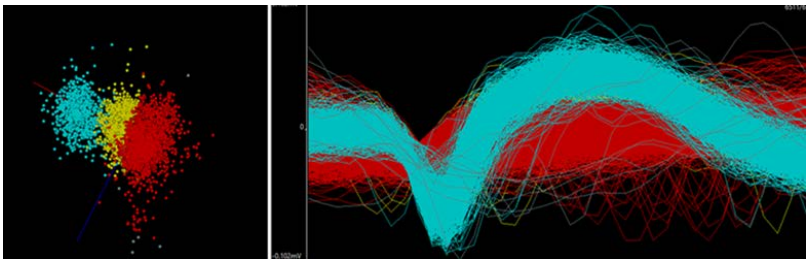

Figure 7-2 Representative In Vivo Neural Signal Quality

Following 1 week we found a high percentage of channels in the layer 3-4 region of the cortex producing high signal-to-noise ratio (SNR) recordable units (Figure 7-2). At this time, multiple animals have been implanted and continue to provide excellent recording quality. Upon completion, data will be analyzed on the basis of SNR, recordordable unit yield, and impedance across channels.

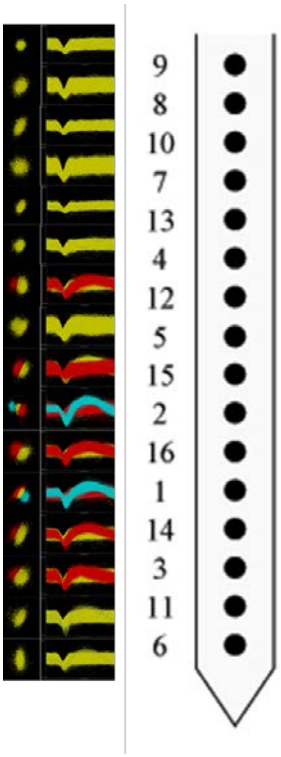

Figure 7-3 Electrode Array Recording Quality vs. Depth

7.2.2 In Vivo Imaging of Oxidative Species

Current analysis of oxidative stress and subsequent neurodegeneration around chronic neural electrodes is limited to histological end-point experiments. The short half-life and diffusion-limited reactions of reactive oxygen species make immunohistochemistry qualitative at best. With the use of dihydrorhodamine 123 (DHR 123), an indicator of ROS, the extent of oxidative stress in ex vivo human skin after exposure to UV light shows promise for directly visualizing ROS in tissue [23-24]. By combining *in vivo* imaging with the unique specificity of DHR 123 for peroxynitrite, it may be possible to visualize oxidative stress near a neural electrode in vivo and in real-time.

To test the ability to visualize an increase in oxidative species *in vivo*, we evaluated DHR fluorescence following stroke insult in the murine brain. In brief, following opening of a craniotomy location, the animal was injected with Rose Bengal (4,5,6,7-tetrachloro-2',4',5',7'-teatraiodofluorescein). Rose Bengal is used in animal models of ischemic stroke, through the creation of a thrombus in blood vessels following illumination by 561 nm light. Prior to excitation of the stroke-inducing rose bengal molecule, DHR was injected into the right hemisphere of the exposed brain tissue. As a control, rhodamine 123 (Rho123) was injected into the contralateral location. After the induction of stroke we observed an increase in the fluorescence of the tissue indicating oxidative production of Rho123 from the injected DHR (Figure 7-4). This tool could be an effective method for understanding the role that oxidative species play around implanted neural electrodes.

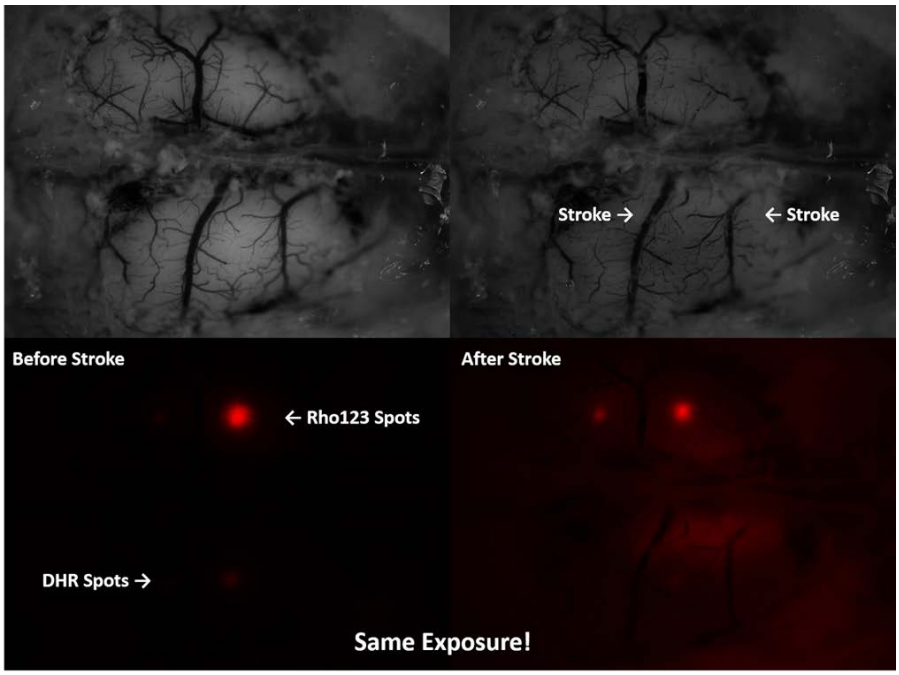

Figure 7-4 In Vivo Imaging of ROS Following Stroke

7.2.3 New Coating Strategy for Parylene C Materials

Using adsorption of L1CAM directly onto parylene C surfaces, we demonstrated an improvement in the neural tissue-electrode interface. Building upon that technology we have continued ways to improve the coating. Chemical modification of parylene C substrates by covalently attaching proteins through EDC/NHS chemistry has previously been described.[90] However, the use of Friedel-Crafts reaction makes the chemistry less effective when working with delicate neural probes. To that end we adapted oxygen plasma treatment for direct modification of payrlene C substrates. By relying upon the formation of O = C – O bonds formed following O_2 plasma treatment (described in *Chapter 4*), we directly modified surfaces with EDC/NHS linking chemistry. Following covalent attachment of L1CAM through the functionalized PC surface we demonstrated improved neuron attachment (Figure 7-5). Covalent strategies for L1CAM coatings will be effective at creating more long-term strategies for biomimetic coatings.

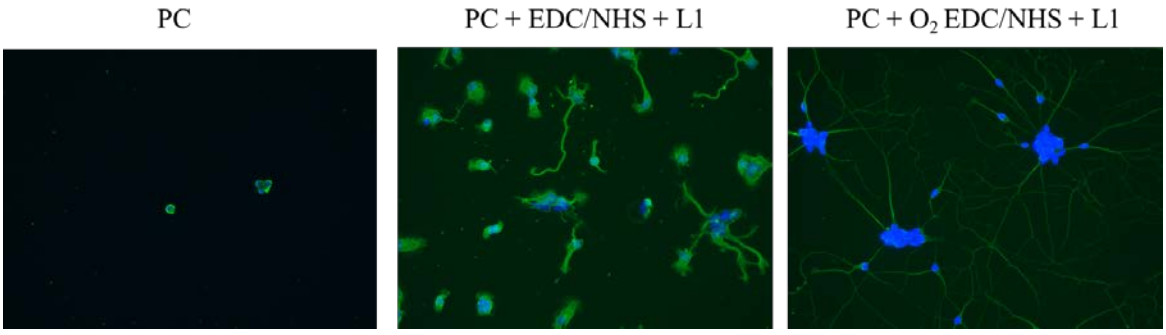

Figure 7-5 Plasma Initiated Covalent Protein Immobilization on PC

7.2.4 Dual Coating Strategy L1 and iSODm

The complex tissue response within the central nervous system (CNS) requires a multidisciplinary approach. Given our promising results with developing both a biomimetic coating as well as an antioxidant coating, we have combined the two technologies to improve the electrode interface. By adding the synthesized iSODm complex to the final step of silane-based coating technology (described in full detail in *Chapter 2* and *Chapter 4*), we were able combine these two coating strategies. Neuron cultures with the dual L1/iSODm coating displayed properties found in both coatings. Like in L1 cultures, the neurites were extensive and unfasiculated (Figure 7-6). However, unlike L1 cultures and more resembling iSODm cultures, the cell bodies readily attached and proliferated on the surface of the coating. By combining these two techniques we may greatly improve the tissue-electrode interface through the synergistic action of a cell adhesion-antioxidant coating.

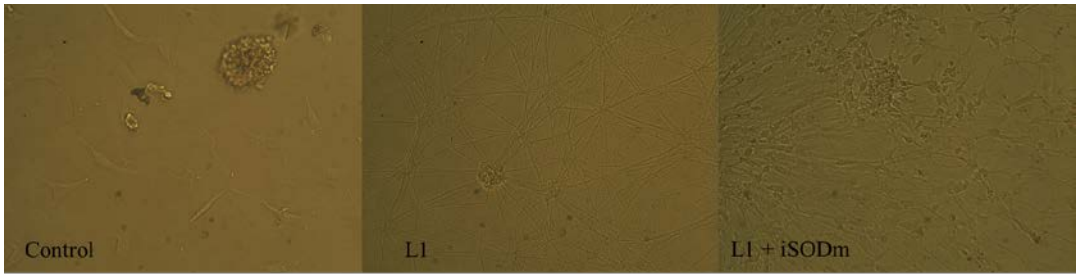

Figure 7-6 Neuron Growth on L1/iSODm Surface

BIBLIOGRAPHY

1. Polikov, V.S., Tresco, P.A. & Reichert, W.M. Response of brain tissue to chronically implanted neural electrodes. *Journal of Neuroscience Methods* **148**, 1-18 (2005).

2. Schwartz, A.B., Cui, X.T., Weber, Douglas J. & Moran, D.W. Brain-Controlled Interfaces: Movement Restoration with Neural Prosthetics. *Neuron* **52**, 205-220 (2006).

3. Brown, R.C., Lockwood, A.H. & Sonawane, B.R. Neurodegenerative Diseases: An Overview of Environmental Risk Factors. *Environmental Health Perspectives* **113**, 1250-1256 (2005).

4. Emerit, J., Edeas, M. & Bricaire, F. Neurodegenerative diseases and oxidative stress. *Biomedicine & Pharmacotherapy* **58**, 39-46 (2004).

5. Stieglitz, T. Neural prostheses in clinical practice: biomedical microsystems in neurological rehabilitation. *Acta neurochirurgica. Supplement* **97**, 411-418 (2007).

6. Navarro, X. et al. A critical review of interfaces with the peripheral nervous system for the control of neuroprostheses and hybrid bionic systems. *Journal of the peripheral nervous system : JPNS* **10**, 229-258 (2005).

7. O'Keefe, J. & Speakman, A. Single unit activity in the rat hippocampus during a spatial memory task. *Exp Brain Res* **68**, 1-27 (1987).

8. Xindong, L. et al. Stability of the interface between neural tissue and chronically implanted intracortical microelectrodes. *Rehabilitation Engineering, IEEE Transactions on* **7**, 315-326 (1999).

9. Williams, J.C., Rennaker, R.L. & Kipke, D.R. Long-term neural recording characteristics of wire microelectrode arrays implanted in cerebral cortex. *Brain research. Brain research protocols* **4**, 303-313 (1999).

10. Vetter, R.J., Williams, J.C., Hetke, J.F., Nunamaker, E.A. & Kipke, D.R. Chronic neural recording using silicon-substrate microelectrode arrays implanted in cerebral cortex. *IEEE transactions on bio-medical engineering* **51**, 896-904 (2004).

11. Biran, R., Martin, D.C. & Tresco, P.A. The brain tissue response to implanted silicon microelectrode arrays is increased when the device is tethered to the skull. *Journal of biomedical materials research. Part A* **82**, 169-178 (2007).

12. Williams, J.C., Hippensteel, J.A., Dilgen, J., Shain, W. & Kipke, D.R. Complex impedance spectroscopy for monitoring tissue responses to inserted neural implants. *Journal of neural engineering* **4**, 410-423 (2007).

13. McConnell, G.C. et al. Implanted neural electrodes cause chronic, local inflammation that is correlated with local neurodegeneration. *Journal of neural engineering* **6**, 056003 (2009).

14. Markesbery, W.R. Oxidative stress hypothesis in Alzheimer's disease. *Free radical biology & medicine* **23**, 134-147 (1997).

15. Jomova, K., Vondrakova, D., Lawson, M. & Valko, M. Metals, oxidative stress and neurodegenerative disorders. *Molecular and cellular biochemistry* **345**, 91-104 (2010).

16. Hensley, K. et al. A model for beta-amyloid aggregation and neurotoxicity based on free radical generation by the peptide: relevance to Alzheimer disease. *Proceedings of the National Academy of Sciences of the United States of America* **91**, 3270-3274 (1994).

17. Dexter, D. et al. Lipid peroxidation as cause of nigral cell death in Parkinson's disease. *Lancet (London, England)* **2**, 639-640 (1986).

18. Dexter, D.T. et al. Basal lipid peroxidation in substantia nigra is increased in Parkinson's disease. *Journal of neurochemistry* **52**, 381-389 (1989).

19. Gilgun-Sherki, Y., Melamed, E. & Offen, D. The role of oxidative stress in the pathogenesis of multiple sclerosis: the need for effective antioxidant therapy. *Journal of neurology* **251**, 261-268 (2004).

20. Gilgun-Sherki, Y., Melamed, E. & Offen, D. Antioxidant treatment in Alzheimer's disease: current state. *Journal of molecular neuroscience : MN* **21**, 1-11 (2003).

21. Piantadosi, C.A. & Zhang, J. Mitochondrial generation of reactive oxygen species after brain ischemia in the rat. *Stroke; a journal of cerebral circulation* **27**, 327-331; discussion 332 (1996).

22. Avantaggiato, A., Bertuzzi, G., Pascali, M., Candotto, V. & Carinci, F. THE THEORIES OF AGING: REACTIVE OXYGEN SPECIES AND WHAT ELSE? *Journal of biological regulators and homeostatic agents* **29**, 156-163 (2015).

23. Klaper, M. & Linker, T. Intramolecular Transfer of Singlet Oxygen. *Journal of the American Chemical Society* **137**, 13744-13747 (2015).

24. Colton, C.A., Snell, J., Chernyshev, O. & Gilbert, D.L. Induction of superoxide anion and nitric oxide production in cultured microglia. *Annals of the New York Academy of Sciences* **738**, 54-63 (1994).

25. Crow, J.P. Dichlorodihydrofluorescein and dihydrorhodamine 123 are sensitive indicators of peroxynitrite in vitro: implications for intracellular measurement of reactive nitrogen and oxygen species. *Nitric oxide : biology and chemistry / official journal of the Nitric Oxide Society* **1**, 145-157 (1997).

26. Zuo, L., Zhou, T., Pannell, B.K., Ziegler, A.C. & Best, T.M. Biological and physiological role of reactive oxygen species--the good, the bad and the ugly. *Acta physiologica (Oxford, England)* **214**, 329-348 (2015).

27. Valko, M., Rhodes, C.J., Moncol, J., Izakovic, M. & Mazur, M. Free radicals, metals and antioxidants in oxidative stress-induced cancer. *Chemico-biological interactions* **160**, 1-40 (2006).

28. Jomova, K. & Valko, M. Advances in metal-induced oxidative stress and human disease. *Toxicology* **283**, 65-87 (2011).

29. Wu, F., Tyml, K. & Wilson, J.X. iNOS expression requires NADPH oxidase-dependent redox signaling in microvascular endothelial cells. *Journal of cellular physiology* **217**, 207-214 (2008).

30. Batinić-Haberle, I. in Methods in Enzymology, Vol. Volume 349 223-233 (Academic Press, 2002).

31. Batinic-Haberle, I., Reboucas, J.S. & Spasojevic, I. Superoxide dismutase mimics: chemistry, pharmacology, and therapeutic potential. *Antioxidants & redox signaling* **13**, 877-918 (2010).

32. Batinic-Haberle, I. et al. Design of Mn porphyrins for treating oxidative stress injuries and their redox-based regulation of cellular transcriptional activities. *Amino acids* **42**, 95-113 (2012).

33. Bernard, A.S. et al. Evaluation of the anti-oxidant properties of a SOD-mimic Mn-complex in activated macrophages. *Dalton transactions (Cambridge, England : 2003)* **41**, 6399-6403 (2012).

34. Khan, M.A., Alam, K., Dixit, K. & Rizvi, M.M. Role of peroxynitrite induced structural changes on H2B histone by physicochemical method. *International journal of biological macromolecules* (2015).

35. Baker, K. et al. Synthetic combined superoxide dismutase/catalase mimetics are protective as a delayed treatment in a rat stroke model: a key role for reactive oxygen

species in ischemic brain injury. *The Journal of pharmacology and experimental therapeutics* **284**, 215-221 (1998).

36. Peng, J., Stevenson, F.F., Doctrow, S.R. & Andersen, J.K. Superoxide dismutase/catalase mimetics are neuroprotective against selective paraquat-mediated dopaminergic neuron death in the substantial nigra: implications for Parkinson disease. *The Journal of biological chemistry* **280**, 29194-29198 (2005).

37. Chertok, B. et al. Iron oxide nanoparticles as a drug delivery vehicle for MRI monitored magnetic targeting of brain tumors. *Biomaterials* **29**, 487-496 (2008).

38. Kong, S.D. et al. Magnetic targeting of nanoparticles across the intact blood-brain barrier. *Journal of controlled release : official journal of the Controlled Release Society* **164**, 49-57 (2012).

39. Sun, C., Lee, J.S. & Zhang, M. Magnetic nanoparticles in MR imaging and drug delivery. *Advanced drug delivery reviews* **60**, 1252-1265 (2008).

40. Pickard, M.R. & Chari, D.M. Robust Uptake of Magnetic Nanoparticles (MNPs) by Central Nervous System (CNS) Microglia: Implications for Particle Uptake in Mixed Neural Cell Populations. *International Journal of Molecular Sciences* **11**, 967-981 (2010).

41. Bal-Price, A. & Brown, G.C. Inflammatory neurodegeneration mediated by nitric oxide from activated glia-inhibiting neuronal respiration, causing glutamate release and excitotoxicity. *The Journal of neuroscience : the official journal of the Society for Neuroscience* **21**, 6480-6491 (2001).

42. Bal-Price, A., Matthias, A. & Brown, G.C. Stimulation of the NADPH oxidase in activated rat microglia removes nitric oxide but induces peroxynitrite production. *Journal of neurochemistry* **80**, 73-80 (2002).

43. Hu, S.-H., Liu, T.-Y., Huang, H.-Y., Liu, D.-M. & Chen, S.-Y. Magnetic-Sensitive Silica Nanospheres for Controlled Drug Release. *Langmuir* **24**, 239-244 (2008).

44. Nakada, T., Matsuzawa, H., Igarashi, H., Fujii, Y. & Kwee, I.L. In vivo visualization of senile-plaque-like pathology in Alzheimer's disease patients by MR microscopy on a 7T system. *Journal of neuroimaging : official journal of the American Society of Neuroimaging* **18**, 125-129 (2008).

45. Katscher, U., Bornert, P. & van den Brink, J.S. Theoretical and numerical aspects of transmit SENSE. *IEEE transactions on medical imaging* **23**, 520-525 (2004).

46. Azemi, E., Lagenaur, C.F. & Cui, X.T. The surface immobilization of the neural adhesion molecule L1 on neural probes and its effect on neuronal density and gliosis at the probe/tissue interface. *Biomaterials* **32**, 681-692 (2011).

47. Azemi, E., Stauffer, W.R., Gostock, M.S., Lagenaur, C.F. & Cui, X.T. Surface immobilization of neural adhesion molecule L1 for improving the biocompatibility of chronic neural probes: In vitro characterization. *Acta Biomaterialia* **4**, 1208-1217 (2008).

48. Lagenaur, C. & Lemmon, V. An L1-like molecule, the 8D9 antigen, is a potent substrate for neurite extension. *Proceedings of the National Academy of Sciences of the United States of America* **84**, 7753-7757 (1987).

49. Lemmon, V., Farr, K.L. & Lagenaur, C. L1-mediated axon outgrowth occurs via a homophilic binding mechanism. *Neuron* **2**, 1597-1603 (1989).

50. Haspel, J., Schurmann, G., Jacob, J., Erickson, H.P. & Grumet, M. Disulfide-mediated dimerization of L1 Ig domains. *Journal of neuroscience research* **66**, 347-355 (2001).

51. Li, Y. & Galileo, D.S. Soluble L1CAM promotes breast cancer cell adhesion and migration in vitro, but not invasion. *Cancer cell international* **10**, 34 (2010).

52. Naka, Y., Kitazawa, A., Akaishi, Y. & Shimizu, N. Neurite outgrowths of neurons using neurotrophin-coated nanoscale magnetic beads. *Journal of Bioscience and Bioengineering* **98**, 348-352 (2004).

53. Johnson, J.L., Ellis, B.A., Munafo, D.B., Brzezinska, A.A. & Catz, S.D. Gene transfer and expression in human neutrophils. The phox homology domain of p47phox translocates to the plasma membrane but not to the membrane of mature phagosomes. *BMC immunology* **7**, 28 (2006).

54. Beckman, J.S. & Koppenol, W.H. Nitric oxide, superoxide, and peroxynitrite: the good, the bad, and ugly. *The American journal of physiology* **271**, C1424-1437 (1996).

55. Deng, J. et al. Magnetic and conducting Fe3O4–polypyrrole nanoparticles with core-shell structure. *Polymer International* **52**, 1182-1187 (2003).

56. Chen, J., Wollenberger, U., Lisdat, F., Ge, B. & Scheller, F.W. Superoxide sensor based on hemin modified electrode. *Sensors and Actuators B: Chemical* **70**, 115-120 (2000).

57. Rahman, I.A. & Padavettan, V. Synthesis of silica nanoparticles by sol-gel: size-dependent properties, surface modification, and applications in silica-polymer nanocomposites — a review. *J. Nanomaterials* **2012**, 8-8 (2012).

58. Rahman, I.A., Vejayakumaran, P., Sipaut, C.S., Ismail, J. & Chee, C.K. Effect of the drying techniques on the morphology of silica nanoparticles synthesized via sol–gel process. *Ceramics International* **34**, 2059-2066 (2008).

59. Kandasamy, G. & Maity, D. RECENT ADVANCES IN SUPERPARAMAGNETIC IRON OXIDE NANOPARTICLES (SPIONs) FOR IN VITRO AND IN VIVO CANCER NANOTHERANOSTICS. *International journal of pharmaceutics* (2015).

60. Islam, M. et al. Liquid crystalline graphene oxide/PEDOT:PSS self-assembled 3D architecture for binder-free supercapacitor electrodes. *Frontiers in Energy Research* **2** (2014).

61. Luo, X., Matranga, C., Tan, S., Alba, N. & Cui, X.T. Carbon nanotube nanoreservior for controlled release of anti-inflammatory dexamethasone. *Biomaterials* **32**, 6316-6323 (2011).

62. Luo, X., Weaver, C.L., Tan, S. & Cui, X.T. Pure graphene oxide doped conducting polymer nanocomposite for bio-interfacing. *Journal of Materials Chemistry B* **1**, 1340-1348 (2013).

63. Weaver, C.L., Li, H., Luo, X. & Cui, X.T. A graphene oxide/conducting polymer nanocomposite for electrochemical dopamine detection: origin of improved sensitivity and specificity. *Journal of Materials Chemistry B* **2**, 5209-5219 (2014).

64. Brown, G.C. & Neher, J.J. Inflammatory neurodegeneration and mechanisms of microglial killing of neurons. *Molecular neurobiology* **41**, 242-247 (2010).

65. Floyd, R.A. Neuroinflammatory processes are important in neurodegenerative diseases: an hypothesis to explain the increased formation of reactive oxygen and nitrogen species as major factors involved in neurodegenerative disease development. *Free radical biology & medicine* **26**, 1346-1355 (1999).

66. Weldon, D.T. et al. Fibrillar beta-amyloid induces microglial phagocytosis, expression of inducible nitric oxide synthase, and loss of a select population of neurons in the rat CNS in vivo. *The Journal of neuroscience : the official journal of the Society for Neuroscience* **18**, 2161-2173 (1998).

67. Block, M.L. & Hong, J.S. Microglia and inflammation-mediated neurodegeneration: multiple triggers with a common mechanism. *Progress in neurobiology* **76**, 77-98 (2005).

68. Lull, M.E. & Block, M.L. Microglial activation and chronic neurodegeneration. *Neurotherapeutics : the journal of the American Society for Experimental NeuroTherapeutics* **7**, 354-365 (2010).

69. Potter-Baker, K.A. et al. Development of Superoxide Dismutase Mimetic Surfaces to Reduce Accumulation of Reactive Oxygen Species for Neural Interfacing Applications. *Journal of materials chemistry. B, Materials for biology and medicine* **2**, 2248-2258 (2014).

70. Reboucas, J.S., Spasojevic, I. & Batinic-Haberle, I. Pure manganese(III) 5,10,15,20-tetrakis(4-benzoic acid)porphyrin (MnTBAP) is not a superoxide dismutase mimic in aqueous systems: a case of structure-activity relationship as a watchdog mechanism in experimental therapeutics and biology. *Journal of biological inorganic chemistry : JBIC : a publication of the Society of Biological Inorganic Chemistry* **13**, 289-302 (2008).

71. Bhatia, S.K. et al. Use of thiol-terminal silanes and heterobifunctional crosslinkers for immobilization of antibodies on silica surfaces. *Analytical biochemistry* **178**, 408-413 (1989).

72. Zhang, F., Liu, J. & Shi, J.-S. Anti-inflammatory activities of resveratrol in the brain: Role of resveratrol in microglial activation. *European Journal of Pharmacology* **636**, 1-7 (2010).

73. Cheepsunthorn, P., Radov, L., Menzies, S., Reid, J. & Connor, J.R. Characterization of a novel brain-derived microglial cell line isolated from neonatal rat brain. *Glia* **35**, 53-62 (2001).

74. Li, Y. & Trush, M.A. Diphenyleneiodonium, an NAD(P)H Oxidase Inhibitor, also Potently Inhibits Mitochondrial Reactive Oxygen Species Production. *Biochemical and Biophysical Research Communications* **253**, 295-299 (1998).

75. Floyd, R.A. & Hensley, K. Oxidative stress in brain aging. Implications for therapeutics of neurodegenerative diseases. *Neurobiology of aging* **23**, 795-807 (2002).

76. Halliwell, B. in eLS (John Wiley & Sons, Ltd, 2001).

77. Keller, J.N. et al. Mitochondrial manganese superoxide dismutase prevents neural apoptosis and reduces ischemic brain injury: suppression of peroxynitrite production, lipid peroxidation, and mitochondrial dysfunction. *The Journal of neuroscience : the official journal of the Society for Neuroscience* **18**, 687-697 (1998).

78. Gomes, A., Fernandes, E. & Lima, J.L.F.C. Fluorescence probes used for detection of reactive oxygen species. *Journal of Biochemical and Biophysical Methods* **65**, 45-80 (2005).

79. Borgmann, S. Electrochemical quantification of reactive oxygen and nitrogen: challenges and opportunities. *Analytical and bioanalytical chemistry* **394**, 95-105 (2009).

80. Amatore, C. et al. Monitoring in real time with a microelectrode the release of reactive oxygen and nitrogen species by a single macrophage stimulated by its membrane mechanical depolarization. *Chembiochem : a European journal of chemical biology* **7**, 653-661 (2006).

81. Amatore, C., Arbault, S., Guille, M. & Lemaître, F. Electrochemical Monitoring of Single Cell Secretion: Vesicular Exocytosis and Oxidative Stress. *Chemical Reviews* **108**, 2585-2621 (2008).

82. Amatore, C. et al. Real-time amperometric analysis of reactive oxygen and nitrogen species released by single immunostimulated macrophages. *Chembiochem : a European journal of chemical biology* **9**, 1472-1480 (2008).

83. Peteu, S., Peiris, P., Gebremichael, E. & Bayachou, M. Nanostructured poly(3,4-ethylenedioxythiophene)-metalloporphyrin films: improved catalytic detection of peroxynitrite. *Biosensors & bioelectronics* **25**, 1914-1921 (2010).

84. Lei, W. et al. Microwave-assisted synthesis of hemin-graphene/poly(3,4-ethylenedioxythiophene) nanocomposite for a biomimetic hydrogen peroxide biosensor. *Journal of Materials Chemistry B* **2**, 4324-4330 (2014).

85. Xu, Y. et al. A Graphene Hybrid Material Covalently Functionalized with Porphyrin: Synthesis and Optical Limiting Property. *Advanced Materials* **21**, 1275-1279 (2009).

86. Roth, K.M. et al. Measurements of Electron-Transfer Rates of Charge-Storage Molecular Monolayers on Si(100). Toward Hybrid Molecular/Semiconductor Information Storage Devices. *Journal of the American Chemical Society* **125**, 505-517 (2003).

87. Kolarcik, C.L. et al. Elastomeric and soft conducting microwires for implantable neural interfaces. *Soft matter* **11**, 4847-4861 (2015).

88. Kolarcik, C.L. et al. In vivo effects of L1 coating on inflammation and neuronal health at the electrode-tissue interface in rat spinal cord and dorsal root ganglion. *Acta Biomater* **8**, 3561-3575 (2012).

89. Kenwrick, S. & Doherty, P. Neural cell adhesion molecule L1: relating disease to function. *BioEssays* **20**, 668-675 (1998).

90. Zhang, C., Thompson, M.E., Markland, F.S. & Swenson, S. Chemical surface modification of parylene C for enhanced protein immobilization and cell proliferation. *Acta Biomaterialia* **7**, 3746-3756 (2011).

91. Song, J.S., Lee, S., Jung, S.H., Cha, G.C. & Mun, M.S. Improved biocompatibility of parylene-C films prepared by chemical vapor deposition and the subsequent plasma treatment. *Journal of Applied Polymer Science* **112**, 3677-3685 (2009).

92. Trantidou, T., Tariq, M., Terracciano, C.M., Toumazou, C. & Prodromakis, T. Parylene C-based flexible electronics for pH monitoring applications. *Sensors (Basel, Switzerland)* **14**, 11629-11639 (2014).

93. Winslow, B.D., Christensen, M.B., Yang, W.K., Solzbacher, F. & Tresco, P.A. A comparison of the tissue response to chronically implanted Parylene-C-coated and uncoated planar silicon microelectrode arrays in rat cortex. *Biomaterials* **31**, 9163-9172 (2010).

94. Kahouli, A. et al. Effect of O 2 , Ar/H 2 and CF 4 plasma treatments on the structural and dielectric properties of parylene-C thin films. *Journal of Physics D: Applied Physics* **45**, 215306 (2012).

95. Pruden, K.G., Sinclair, K. & Beaudoin, S. Characterization of parylene-N and parylene-C photooxidation. *Journal of Polymer Science Part A: Polymer Chemistry* **41**, 1486-1496 (2003).

96. Golda, M., Brzychczy-Wloch, M., Faryna, M., Engvall, K. & Kotarba, A. Oxygen plasma functionalization of parylene C coating for implants surface: nanotopography and active sites for drug anchoring. *Materials science & engineering. C, Materials for biological applications* **33**, 4221-4227 (2013).

97. Fraser, G.W. & Schwartz, A.B. Recording from the same neurons chronically in motor cortex. *Journal of neurophysiology* **107**, 1970-1978 (2012).

98. Chang, T.Y. et al. Cell and Protein Compatibility of Parylene-C Surfaces. *Langmuir* **23**, 11718-11725 (2007).

99. Rabe, M., Verdes, D. & Seeger, S. Understanding protein adsorption phenomena at solid surfaces. *Advances in Colloid and Interface Science* **162**, 87-106 (2011).

100. Recek, N. et al. Protein Adsorption on Various Plasma-Treated Polyethylene Terephthalate Substrates. *Molecules* **18**, 12441 (2013).

101. Pardridge, W.M. Blood-brain barrier biology and methodology. *Journal of neurovirology* **5**, 556-569 (1999).

102. Sawyer, A.J. & Kyriakides, T.R. Nanoparticle-based evaluation of blood-brain barrier leakage during the foreign body response. *Journal of neural engineering* **10**, 016013 (2013).

103. Kumar, C.S.S.R. & Mohammad, F. Magnetic Nanomaterials for Hyperthermia-based Therapy and Controlled Drug Delivery. *Advanced drug delivery reviews* **63**, 789-808 (2011).

104. Qhobosheane, M., Santra, S., Zhang, P. & Tan, W. Biochemically functionalized silica nanoparticles. *The Analyst* **126**, 1274-1278 (2001).

105. Liu, X., Ma, Z., Xing, J. & Liu, H. Preparation and characterization of amino–silane modified superparamagnetic silica nanospheres. *Journal of Magnetism and Magnetic Materials* **270**, 1-6 (2004).

106. Ceballos, D. et al. Magnetically Aligned Collagen Gel Filling a Collagen Nerve Guide Improves Peripheral Nerve Regeneration. *Experimental Neurology* **158**, 290-300 (1999).

107. Nowacek, A. & Gendelman, H.E. NanoART, neuroAIDS and CNS drug delivery. *Nanomedicine* **4**, 557-574 (2009).

108. Pardridge, W.M. CNS Drug Design Based on Principles of Blood-Brain Barrier Transport. *Journal of neurochemistry* **70**, 1781-1792 (1998).

109. Grabrucker, A.M. et al. Development of Novel Zn²⁺ Loaded Nanoparticles Designed for Cell-Type Targeted Drug Release in CNS Neurons: In Vitro Evidences. *PLoS ONE* **6**, e17851 (2011).

110. Vergoni, A.V. et al. Nanoparticles as drug delivery agents specific for CNS: in vivo biodistribution. *Nanomedicine: Nanotechnology, Biology and Medicine* **5**, 369-377 (2009).

111. Luo, X. & Cui, X.T. Sponge-like nanostructured conducting polymers for electrically controlled drug release. *Electrochemistry communications* **11**, 1956 (2009).